ELECTRONIC CHARACTERIZATION OF SIZE-SELECTED PLATINUM CLUSTERS AND MODIFICATION THROUGH ATOMIC LAYER DEPOSITION

by

Yang Dai

A dissertation submitted to the faculty of
The University of Utah
in partial fulfillment of the requirements for the degree of

Doctor of Philosophy

Department of Chemistry

The University of Utah

May 2017

The University of Utah Graduate School

STATEMENT OF DISSERTATION APPROVAL

The dissertation of **Yang Dai**

has been approved by the following supervisory committee members:

Scott L. Anderson	, Chair	**9/14/2016** Date Approved
Peter B. Armentrout	, Member	**9/14/2016** Date Approved
Jennifer Shumaker-Parry	, Member	**9/14/2016** Date Approved
Ryan P. Steele	, Member	**9/14/2016** Date Approved
Anil Vasudeo Virkar	, Member	**9/14/2016** Date Approved

and by **Cynthia Burrows**, Chair/Dean of

the Department/College/School of **Chemistry**

and by David B. Kieda, Dean of The Graduate School.

ABSTRACT

The research presented in this dissertation will focus on the electronic structure of size-selected Pt_n ($n \leq 24$) clusters supported on oxidized Si, as well as their catalytic activity, surface morphology, and electronic structure when Pt clusters are overcoated/undercoated by Al_2O_3 via 1-3 cycles of atomic layer deposition (ALD). The experiments found within this dissertation required the modification, design, and construction of a complex instrument capable of spanning pressures down to ultra high vacuum (UHV) levels while allowing for relatively high pressure ALD chambers and quick sample exchange. This was accomplished by designing and building a cluster deposition beamline capable of depositing size-selected metal clusters as well as the necessary sample holders and sample stages to make and analyze samples. Though the main goal was to determine how ALD overcoating/undercoating affects SiO_2 supported Pt_n clusters, during the course of this research, it was discovered that the inherent size effects on the electronic structure of clusters can also be reflected by white line and absorption edge in X-ray absorption near edge structure (XANES) spectra. This result will give implications for the interpretation of XANES on nano/subnanometer size metal clusters.

In addition to the investigation of the size effects on the electronic structures of Pt_n clusters via X-ray photoelectron spectroscopy (XPS) and XANES, the surface morphology, and catalytic activity of Pt_n clusters with and without ALD modification were also probed by ion scattering spectroscopy (ISS), grazing-incidence small-angle scattering (GISAXS),

and CO temperature programed desorption (TPD). Trimethylaluminum, the precursor of Al_2O_3 ALD, preferentially binds to "on-top" sites of Pt_n clusters, and by depositing Al_2O_3 via 1 cycle of ALD, high-temperature CO binding sites are completely blocked and these sites are not recoverable.

Chapter 1 gives a brief introduction into heterogeneous catalysis, and more specifically, the importance of size-selected clusters and the advantage of ALD-modified catalysts. Chapter 2 presents the design of the cluster deposition beamline, sample holder, and sample stages, and the description of the whole instrument. Chapter 3 focuses on the size effects of Pt_n clusters on XANES spectra and its implication. Finally, Chapter 4 discusses the effects of deposited Al_2O_3 via ALD on the electronic structure, catalytic activity, and surface morphology of Pt_n clusters.

TABLE OF CONTENTS

ACKNOWLEDGEMENTS

This dissertation would not have been possible without the help of so many people. First, I would like to express my deepest gratitude to my graduate advisor, Dr. Scott L. Anderson, for his guidance, support, and encouragement throughout the research. Working with him really enables me to grow as a critical thinker and a scientist. Thanks to him, I had the opportunity to build, test, and utilize the cluster deposition beamline for the research.

I will always look back and appreciate the jokes from him when I was frustrated troubleshooting the instrument, it helped keep me sane in a frustrating time. He treated me not as a student, but as a colleague. Joining his group is the one choice I will never regret making.

I want to thank my comrade, Tim Gorey, without whom my graduate work would have taken at least another two years. We shared so many things in common—favorite band, Lonely Island, "Call Me Maybe," Indochine lunch special, and some wired words we developed that only we can understand. People passing through our lab could always hear our horrible singing. He made working in the lab so enjoyable. He also helped me become a "true" chemist, by teaching me how to brew beer. It is definitely a hobby I will enjoy in my life.

I also cherish the mentorship and friendship from my officemate, Will Kunkel and my previous colleague, Matt Kane, to whom I attribute most of my data analysis skills and

lab skills. I forgive you, Matt, for giving me the wrong target and wasting almost two months trying to find Pt from XPS until I realized that the target you gave me was Ir instead of Pt. And I apologize for constantly bugging you and discussing research with you even though you are now working in a pharmaceutical company. And Will, as my smoking partner for the past five years, we had countless conversations over various topics during our "smoke breaks." He is the guy who takes everything very seriously. He wrote his comments in extreme detail during my practice talks to help me improve, and for that, I am truly grateful.

I would like to thank my committee members: Professor Peter Armentrout, Professor Jennifer Shumaker-Parry, Professor Ryan Steele, and Professor Anil Virkar for important discussions about my research and guiding me through all these years. I also owe my thanks to Willow Toso and Dale Heisler from the electronic shop, without whom, I would not know how to troubleshoot an RF generator or power supplies. Two of the most important people in my first three years, Dennis Romney and Tom Gudmundson from the machine shop, taught me a great deal about instrument design and machining techniques. I will truly benefit greatly from the machine shop class they taught, not just for my graduate work, but for the rest of my life.

I want to give my special thanks to my wife, Chaoya Sun, who made great sacrifices in order to support me to finish my Ph.D. Along with her, I want to acknowledge my parents and parents-in-law for their support and encouragement. During the lab tour I gave to my father-in-law, he said that my lab was more like a garage than a lab because there were so many bolts and wrenches lying everywhere. Ever since then, I have kept everything in my lab very organized and clean. His advice was well noted.

Finally, I want to acknowledge my son, Samuel. I am sorry that I could not stay beside you since you were born. It was heartbreaking when I knew that you called dad to every man with short hair and a big face. I promise, that I will come back home to you very soon.

CHAPTER 1

INTRODUCTION

1.1 Size-Selected Clusters as Model Catalysts

Catalysis is undoubtedly one of the most important fields in the modern economy, contributing approximately 35% of the world's Gross Domestic Product (GDP) with annual sales of ~1.5 trillion dollars.[1] Of all the different approaches to catalytic research, heterogeneous catalysis involving supported nanoparticles on high-surface-area substrates has been drawing great attention from researchers. When the size of the catalytic particles reaches into the nanometer regime, not only do the active sites on the surface increase, but most importantly, the catalytic properties differ dramatically from their bulk counterparts. The most representative example is the Au nanoparticles (< 2nm) which demonstrate great catalytic activity on various oxidation reactions,[2-4] whereas Au bulk is well-known for its inertness.

Model catalysts are commonly used in fundamental research in an attempt to understand the origin of the catalytic properties of nanoparticles. The advantage of model catalyst studies is that the systems (nanoparticles and support) are greatly simplified as compared to real-world catalysts by conducting the experiments in well-controlled environments, such as ultra-high vacuum (UHV) in order to eliminate all the contaminants, and depositing nanoparticles on a well-defined substrate. Furthermore, the size of the clusters deposited can also be precisely controlled by using a size-selected cluster deposition source. By varying the size of metal clusters, it has become possible to probe the surface morphology and electronic structure of small nano/subnanoclusters, correlate them with the catalytic properties, and ultimately lead to the rational design of new efficient catalysts.

Size-selected cluster deposition gives great flexibility in terms of cluster size and

coverage, yet is not limited by the cluster-support combination. In contrast, commonly used vapor deposition techniques do not provide precise control over cluster sizes due to the fact that cluster growth depends on the nucleation sites (usually the defect sites) on the substrates. [5-7]Colloidal synthesis methods can also be used to make clusters with a relatively narrow size distribution, however, the synthesized clusters are covered by capping ligands or molecules which can lead to the poisoning of catalysts by blocking the active sites. Therefore, model catalyst prepared by size-selected cluster deposition is the most suitable to the investigation of the origin of catalytic properties for nanoclusters.

1.2 Electronic Structure of Metal Clusters

The electronic structure of nanoclusters evolves rapidly as the size decreases below 2 nm. More specifically, the electronic structure of nanoclusters is different from that of the bulk due to the disappearance of conduction band, the formation of a band gap and the discretization of the electron orbitals. By using Scanning Tunneling Spectroscopy (STS), Lai et al.[8] oberserved that Au nanoparticles (NPs) (> 4 nm in diameter) have a well-developed bulk-like electronic structure , and a band gap only starts to form when the size of Au NPs becomes smaller, indicating the transition from metal to nonmetal, and a similar trend was also observed for Pd NPs, suggesting that this is a fundamental size property as opposed to a unique phenomenon seen only in gold.

It has been shown that the deviation of electronic structure of the metal nanoclusters from the bulk is closely related to the catalytic activity and selectivity.[9-11] Tuning the electronic structure by precise control over cluster size can lead to improved performance of catalysts. Therefore, full rational design and development of new

catalysts requires fundamental research on the understanding of the relationship between NPs properties, such as electronic structure and morphology, and catalytic performance. Commonly used surface analysis techniques for probing electronic structures of nanoclusters are X-ray photoelectron spectroscopy (XPS), and ultra-violet photoelectron spectroscopy. These are great tools in monitoring the change of the core level electrons and valence level electrons; however, they can mostly only be used in UHV. Thanks to the advancement and availability of synchrotron light sources, X-ray absorption fine structure has been gaining increasing popularity in the field of heterogeneous catalysis due to its ability to probe the electronic structure both in situ and in operando conditions.[12] In XANES, an X-ray absorption spectrum is measured when core electrons are ejected by absorbing X-ray photons with sufficient energy. Two useful features, absorption edge energy, and white line intensity, are typically of greatest interest. Edge energy is determined by the energy required to excite a core electron to the lowest unoccupied orbital (LUMO). White line intensity is the measurement of the density of unoccupied density of states, and thus also sensitive to the transition probabilities. Conventionally in heterogeneous catalysis, the white line intensity and its absorption edge energy are used as indicators to determine the oxidation states of the catalysts. As the oxidation states increases, the edge energy and the white line intensity increases accordingly. However, as the particle size of the catalysts reach to nano/subnanoscale regime, the electronic structure will deviate from their bulk counterpart. Therefore, a question is raised: is the conventional method of XANES spectra interpretation still valid? Part of the work in this dissertation presents that the particle size plays an important role in XANES, and the size effect must be taken into account when

interpreting XANES for nanoclusters less than a few nanometer size range.

1.3 Atomic Layer Deposition Modified Catalysts

Catalytic activity, selectivity, and stability are the three main factors that affect the catalysts' performance. It is difficult to simultaneously control all of them. The recent development of atomic layer deposition (ALD) overcoating on nanoparticles has shown great promise to accomplish this goal. ALD applies self-limiting reactions and provides precise control over the film growth on the atomic scale. There are two different methods of ALD overcoating, depending on whether the supported NPs are completely covered by an ALD film.[13] When the NPs are completely overcoated (typically over 20 cycles of ALD) initially, the thick film will eliminate the catalytic activities of the NPs and substrate due to the inaccessibility of the reactants to the surface active sites. However, through heat treatment, nano-pores are formed and reexpose the NPs surface to the reactants.[14,15] The thick ALD layer acts as a physical barrier to prevent sintering or agglomeration, while the selectivity of the catalysts is improved because the low-coordination sites are blocked by the overcoats, leaving mostly the terrace sites exposed. There is no better example of improved catalytic selectivity and stability than the ALD-overcoated Pd NPs for oxidative dehydrogenation of ethane.[15] With 45 cycles of Al_2O_3 ALD (~7.7 nm thick) on Pd NPs (~2.8 nm) surface, the catalysts give a 23% yield of desired ethylene product in contrast to 1.9% for the uncoated Pd NPs. Meanwhile, the overcoated Pd NPs demonstrate stable activity for ~1700 min and negligible change of particle size whereas the uncoated Pd NPs completely lose catalytic activity due to coke formation and particle sintering.

Another method of ALD overcoating is done by partially coating the supported NPs and the substrate with less than 10 cycles of ALD, leading to a discontinuous film on the surface.[13] The overcoat preferentially nucleates at the low-coordinated sites (edges and corners) of the NPs, analyzed by HR-TEM and DRIFT.[16-18] These low-coordination surface sites are responsible for sintering,[19] and some unwanted side reactions. The advantage of this method is that more NPs surface can be exposed with less cycles of ALD, and thus will have a high catalytic activity as a comparison to the former overcoating method discussed.

Although ALD overcoating has shown significant improvement in catalytic performance, it is mainly used to modify the surface of NPs with the size range above ~2.5 nm. In Chapter 4 of this dissertation, we present a study of Al_2O_3 ALD on size-selected Pt_{24} clusters with XPS, XANES, TPD, GISAXS, and ISS. The combination of the exceptional thickness control of the Al_2O_3 ALD performed in High Vacuum (HV) with precise control over the cluster size is demonstrated as a great way to fine tune the morphology, electronic structure, and ultimately, the catalytic performance.

1.4 References

(1) Ma, Z.; Zaera, F. In *Encyclopedia of Inorganic Chemistry*; John Wiley & Sons, Ltd: Hoboken, NJ, 2006.

(2) Gao, F.; Goodman, D. W. *Annu. Rev. Phys. Chem.* **2012**, *63*, 265.

(3) Haruta, M.; Date, M. *Appl. Catal. A: General* **2001**, *222*, 427.

(4) Fu, Q.; Saltsburg, H.; Flytzani-Stephanopoulos, M. *Science* **2003**, *301*, 935.

(5) Henry, C. R. *Cryst. Res. Technol.* **1998**, *33*, 1119.

(6) Campbell, C. T. *Surf. Sci. Rep.* **1997**, *27*, 1.

(7) Freund, H. J.; Pacchioni, G. *Chem Soc Rev* **2008**, *37*, 2224.

(8) Lai, X.; St. Clair, T. P.; Valden, M.; Goodman, D. W. *Prog. Surf. Sci.* **1998**, *59*, 25.

(9) Roberts, F. S.; Kane, M. D.; Baxter, E. T.; Anderson, S. L. *Phys. Chem. Chem. Phys.* **2014**, *16*, 26443

(10) Kaden, W. E.; Wu, T.; Kunkel, W. A.; Anderson, S. L. *Science* **2009**, *326*, 826.

(11) Abbet, S.; Sanchez, A.; Heiz, U.; Schneider, W.-D. *J. Catal.* **2001**, *198*, 122.

(12) Ramaker, D. E.; Koningsberger, D. C. *Phys. Chem. Chem. Phys.* **2010**, *12*, 5514.

(13) O'Neill, B. J.; Jackson, D. H. K.; Lee, J.; Canlas, C.; Stair, P. C.; Marshall, C. L.; Elam, J. W.; Kuech, T. F.; Dumesic, J. A.; Huber, G. W. *ACS Catal.* **2015**, *5*, 1804.

(14) Ma, Z.; Brown, S.; Howe, J. Y.; Overbury, S. H.; Dai, S. *J. Phys. Chem. C* **2008**, *112*, 9448.

(15) Lu, J. L.; Fu, B. S.; Kung, M. C.; Xiao, G. M.; Elam, J. W.; Kung, H. H.; Stair, P. C. *Science* **2012**, *335*, 1205.

(16) Wang, C.; Wang, H.; Yao, Q.; Yan, H.; Li, J.; Lu, J. *J. Phys. Chem. C* **2016**, *120*, 478.

(17) Feng, H.; Lu, J.; Stair, P. C.; Elam, J. W. *Catal. Lett.* **2011**, *141*, 512.

(18) Lu, J.; Liu, B.; Greeley, J. P.; Feng, Z.; Libera, J. A.; Lei, Y.; Bedzyk, M. J.; Stair, P. C.; Elam, J. W. *Chem. Mater.* **2012**, *24*, 2047.

(19) Greeley, J. *Electrochimica Acta* **2010**, *55*, 5545.

CHAPTER 2

CLUSTER DEPOSITION BEAMLINE EQUIPPED WITH IN SITU SURFACE PREPARATION AND CHARACTERIZATION TECHNIQUES

2.1 Introduction

The experiments in this dissertation utilized a newly designed and constructed surface science instrument capable of depositing size-selected metal clusters on well characterized substrates in ultra-high vacuum (UHV), thin film deposition (ALD), as well as in situ analysis of the as-deposited samples via X-ray photoelectron spectroscopy (XPS), ion scattering spectroscopy (ISS), and temperature programmed desorption/reaction (TPD/TPR). The design of the newly built cluster deposition beamline is based on that of the original beamline in our lab with improvements over target motion control system, nominal mass range (up to ~16,000 Da), and differential pumping stages. More importantly, by attaching the cluster deposition beamline to the existing VG Scientific ESCALAB MKII surface analysis apparatus, we can take advantage of its sample transferring system and sample preparation chamber, allowing faster sample production for the ex situ analysis and sample surface modification via atomic layer deposition (ALD) under high vacuum. It took ~3 years to bring the whole instrument fully into practice since the initial design began.

The assembly of the new cluster deposition instrument is shown in Figure 2.1. The instrument consists of three distinct regions, including a cluster deposition beamline, a load lock for sample exchange, and an ultra-high vacuum (UHV) system that can be further divided into three separately pumped sections. More specifically, there is a “prep” chamber (base pressure 8×10^{-10} Torr), a “main” section (2.5×10^{-10} Torr) that is further broken down into a main chamber and a spherical chamber, and a chamber with a mass spectrometer (UTI 100 quadrupole powered via Extrel electronics) that samples gas from the main section through a 3 mm aperture via a skimmer cone. Each section has both

turbomolecular and titanium sublimation pumps. The details of each section and sample transfer are discussed below.

2.2 Instrument Design

2.2.1 Sample Transfer

A sample can be introduced into the prep chamber through the load lock, which is attached to the prep chamber with the base pressure at $< 10^{-7}$ Torr, as measured by a cold cathode vacuum gauge. There is a heating stage in the load lock allowing sample heating up to ~1200 K. Through the load lock, the sample is transferred by a wobble stick and positioned onto a magnetic transporter, which can then be transferred to either a fixed ALD stage in the prep chamber, or passed into the spherical chamber in the main UHV section, where it can be either transferred to a rotary sample carousel that can store up to six samples, or onto a precision XYZ manipulator. The manipulator is used to position the sample in one of three positions. The first position is located in the spherical chamber, where the sample is at the focus of a hemispherical energy analyzer, a windowless vacuum UV lamp,[1] dual anode and monochromatic X-ray sources, and an electron impact ion gun, allowing sample cleaning by sputtering and annealing, and spectroscopic analysis by UPS, XPS, and ISS. In the second position, which is located in the main chamber, the sample is held 1 mm behind the exposure mask of the cluster deposition beamline allowing a well-defined 2 mm diameter spot of size-selected clusters to be deposited. In the third position shown in Figure 2.2, the sample is held in front of the differential pumping aperture for the mass spectrometer (UTI 100 quadrupole with Extrel electronic) allowing analysis of the species desorbing from the sample. In the mass

spectrometry position, the sample is also at the focus of 6 dosing tubes that can be used to deliver either continuous or pulsed gas doses for reactivity studies. Positioning repeatability is estimated to be better than 50 μm.

2.2.2 Cluster Deposition Beamline

The design of the cluster deposition beamline is based on that of an existing beamline in our lab.[2-4] As shown in Figure 2.3, it consists of seven chambers, and can be divided into six sections comprised of a laser vaporization source, first quadrupole (quad), second quad, quadrupole mass spectrometer (QMS), isolation valve, and final quad. Each chamber is pumped by an independent pumping station with the exception of the final two chambers together being pumping by a single pumping station. During deposition, the pressure in the main section increases by ~2×10^{-10} Torr of helium.

2.2.2.1 Vaporization Source

The clusters are produced in a laser vaporization source located in the square chamber by irradiating a metal target with a 532 nm Nd: YAG laser at a rate of 20 Hz. The schematic representation of the vaporization source is shown in Figure 2.4. In the square chamber, the metal target is glued onto an aluminum block using J-B weld. The edge of the metal surface is covered by a thin Teflon sheet in order to make smooth contact with the polished stainless steel surface during laser vaporization process. The metal target is pushed against the wall by the springs to create a seal for the helium flow. The target is attached to a motor system controlled by a program written by LabVIEW software so the whole surface has equal amount of laser exposure. During deposition,

metal plasma is generated by laser vaporization of a rastering metal target. The plasma is cooled in the waiting chamber and carried by a pulsed inert carrier gas flow (helium) through a cylindrical nozzle orifice (0.08 in. in diameter). The helium gas line is cooled by a liquid N_2 reservoir to have a better cooling effect on the plasma, and eliminate any potential contaminants from flowing into the main chamber, that is, water. Helium gas is injected into the source through an inlet controlled by a piezoelectric valve with an O-ring seal. The frequency of the helium pulse is synchronized with the laser repetition rate and its timing relative to the laser pulse can be adjusted through a pulse generator (Quantum 9514+). In addition to the helium gas propulsion, an initial kinetic energy is mostly gained for metal cations by the positive float voltage on the source.

During deposition, the pressure in the source cannot be directly measured, instead, the foreline pressure is measured and used as a parameter to adjust for different sizes of clusters. Inside the source, the pressure is approximately in the order of a few Torr. In addition to the helium pressure, each size of metal cluster is also sensitive to the timing and duration of the helium pulse, with the possible explanation being that more helium is needed to cool the plasma in order to form larger clusters.

2.2.2.2 First and Second Quadrupole Ion Guide

A quadrupole ion guide is an electric quadrupole consisting of four cylindrical rods alternating positive and negative potentials. The rods are made by stainless steel with a diameter of 0.374 in. Each quadrupole ion guide in the beamline operates in the radio frequency (RF) of ~2.1 MHz, allowing high transmission of ions without mass filtering capability. DC potential is also applied to the quadrupole rods and can be

adjusted to obtain optimal ion transmission.

After expanding into vacuum through the cylindrical nozzle, cluster cations are collected and guided by the first quadrupole (quad) ion guide. The negatively charged particles produced are attracted by the source since the source is positively biased relative to the ground. The ports of the first quad chamber that connects the square chamber and the second quad chamber has a 20˚ bending angle (Figure 2.3), which prevents neutral clusters from getting through the beamline and being deposited on the sample surface. At the end of the first quad, the trajectory of positively charged metal clusters are bent by the bending lens into the second quad. The main purposes of the second quad are to reduce the helium pressure through three differentially pumping stages and to stabilize the trajectory of the clusters. The pressure after the second quad drops down to ~3×10^{-6} Torr during the deposition.

2.2.2.3 Quadrupole Mass Spectrometer

After the second quad, cluster cations are mass selected by a home-made quadrupole mass filter (Figure 2.5) controlled by 440 kHz electronics (Extrel 150-QC) that give a nominal mass range up to 16,000 Da. In between the second quad and QMS, there is an Einzel lens stack to improve the transmission of the beam. The QMS section consists of pre- and postfilters,[5] allowing better focus of the cluster beam in and out of the mass filter, and four high precision cylindrical electrodes (stainless steel, 6.8 in. in length, 0.374 in. in diameter). The distance between the facing edges of two opposite poles is 0.326 in., nominally 1/1.148 times the rod diameter, which allows the geometric center of the quadrupole to be approximately an ideal hyperbolic field.

For QMS, there are four parameters that need to be controlled in order to allow the transmission of size-selected cluster beam, including RF voltage, DC pole bias, ΔM and ΔRes. More specifically, RF and DC voltages are directly related to the mass of the clusters. In extrel electronics, the mass resolution increases linearly as mass increases, and ΔRes corresponds to the slope of the scan line, which mainly affects the sensitivity and resolution for high masses. ΔM, on the other hand, graphically represents the intercept of the scan line in a plot where RF voltage is the x-axis, and DC voltage is the y-axis. ΔM controls the sensitivity and mass resolution in the lower mass range.

2.2.2.4 Isolation Valve and Final Quadrupole Ion Guide

With the cluster size being selected be the QMS, the cluster beam is then passed through a home-made isolation valve (Figure 2.6) separating the beamline and the UHV system. The isolation valve consists of a lens stack allowing better beam transmission to the final quad, and a pusher that connects to a solenoid valve. When the pusher is in the closed position as shown in Figure 2.6, the beamline is isolated from the UHV system by an O-ring seal, and short two lenses. In the open position, the two lenses become isolated and the cluster beam can be guided through. The valve is only open during the deposition process.

Finally, the size-selected clusters are guided by the final quad and deposited onto the sample surface through a 2 mm diameter exposure mask which the sample is positioned behind in the main UHV section so that consistent deposition spot diameters are achieved.

2.2.2.5 Deposition Energy and Current Measurement

Through the whole deposition process, the clusters gain their initial kinetic energy through helium propulsion and source voltage. The kinetic energy of the clusters depositing on the substrate is controlled by electrically floating the beamline with respect to the sample, which is grounded through an electrometer. Because the source imparts some kinetic energy to the clusters beam, deposition energy is calibrated via a retarding potential analysis of the cluster beam on the sample. The amount of clusters deposited on the sample is monitored continuously via the cluster cation neutralization current, and then converted to the unit of monolayer corresponding to the close-packed bulk metal.

2.2.2.6 Testing and Operating Conditions

Typical operating conditions for depositing 1 eV Pt_{24} clusters are given in Table 2.1. It is important to know that beamline operating condition varies depending on the size of the clusters and the metal chosen. Ten electrostatic lenses as well as source pressure, laser power, helium pulse timing, and quadrupole AC and DC voltages need to be controlled for each specific size of metal clusters. When there is noticeable current measured by the picoammeter, the cluster beam transmission can be tuned by adjusting all the parameters. However, it is usually the case that there is no beam transmission at all when a new metal target is used. In order to establish a correct set of parameters for a new metal target, the picoammeter is firstly hooked to bending lenses as we try to maximize the beam transmission from the source through the first quad by tuning just the first quad voltage, source voltage, helium timing, and laser power. After the current reaches its maximum, we then hook the picoammeter to a lens in the second quad, and so

forth. By doing so, we can minimize the parameters we need to control and gradually guide the beam all the way to the sample.

Cluster beam currents are typically between 30 pA and 1500 nA for Pt with the beamline float voltage on, leading to a deposition time that ranges from 5 to 60 min for a 0.1 ML equivalent surface coverage. Since the operating condition of the beamline is not fully optimized, there is still room for deposition rate improvement.

2.2.3 Sample Holder and Stage

Because part of the UHV system still utilizes the VG sample transport hardware (VG ESCALAB II) including its wobble stick forks, magnetic transporter, and loadlock sample transfer system, it is necessary to adapt our design of the home-made sample holders and sample stages to the requirements of VG transport hardware so that they will be compatible with the existing VG sample transport hardware.

There are three sample stages designed for different purposes. The first one is the manipulator sample stage in the main UHV section with heating and cooling capability, used for cluster deposition, TPD, and spectroscopic studies including XPS, UPS, and ISS. Though this stage can also be used for sample cleaning through sputtering and annealing, such usage is usually avoided as an attempt to prevent the introduction of contamination into the UHV system. The second one is sample preparation stage located in the prep chamber with heating capability. It is used for sample surface cleaning, annealing, and thin film deposition from evaporative source. In addition, this stage is specially designed to perform atomic layer deposition in high vacuum. The third stage is located in the load lock with heating capability. Though this capability was not used in the experiments

described in the dissertation, it is mainly designed to be a sample stage in a high-pressure cell for sample preparation and some experiments where large dose of reactant gas is needed. The details of the sample holder, manipulator stage, and preparation stage are discussed below.

2.2.3.1 Sample Holder

Samples are mounted on homemade transferrable sample holders, improved from an earlier design.[6] The sample holder is shown in Figure 2.7. The manipulation stub allows the use of both conventional wobble stick forks and coaxial pincer grip wobble sticks to transfer the sample holder. The pin is used to mate to cylindrical sockets in order to mount the sample holder in the ESCALAB's magnetic transporter and sample holder "parking" carousel. Tantalum wires are spot-welded onto the opposite sides of the sample and mounted on the sample holders by screws. In addition to the mounting purpose, the tantalum wires are also used for resistive heating. Ceramic block and washers are used to prevent short circuit and allow electric current only flow through the tantalum wires during resistive heating. For temperature measurement, the junction of thin thermocouple wires (C-type, 0.005 in. in diameter) are directly spot-welded onto the sample. The other end of the wires is fed through a pinhole and spot-welded on the side of thermocouple posts (0.056 in. in diameter) which are held down by pins in a groove on the ceramic block. When the sample holder is fully inserted into a sample stage, the thermocouple post from the sample holder will make contact with the thermocouple electrode, and create a closed circuit for temperature measurement on the sample. The body of the sample holder is designed to be V-shaped for the convenience of insertion.

Substrates such as SiO_2 that cannot be directly spot-welded, are then clipped to a tantalum backing plate. Both the tantalum heating wires and C-type thermocouples are spot-welded onto the back of the backing plate. The surface of the backing plate is carefully made flat in order to maximize the contact area between the backing plate and the substrate for better heat transfer.

We have collaborated with Oak Ridge National Lab (ORNL) for in situ transmission electron microscopy (TEM) studies on size-selected Pt_n clusters, which allows us to directly observe deposited Pt_n clusters under various conditions. To achieve this, size-selected Pt_n clusters need to be directly deposited onto the TEM liquid cell (Poseidon E-chips, 6 mm × 4.5 mm × 0.28 mm) in UHV. To achieve this, a custom designed sample holder was made to mount the E-chip in UHV for cluster deposition. The schematics in Figure 2.8 shows the design of the holder. An E-chip can be inserted into the socket of the holder in the middle. Because the sample needs to be positioned vertically during deposition, in order to prevent the E-chip from falling off the holder, two separate lids were attached to both ends by 0-80 screws. The hole in the middle of the holder is for the purpose of alignment so that the clusters can be deposited onto the correct spot on the E-chip. The E-chip holder is mounted on the sample holder via tantalum heating wires, as shown in the bottom picture in Figure 2.8. The holder can be heated to 450 K in UHV to desorb organic solvent used for E-chip cleaning.

2.2.3.2 Manipulator Sample Stage

The manipulator sample stage is shown in Figure 2.9. The stage is attached to the end of the rod inside the manipulator bellow. When the sample holder is inserted into the

stage, the thermocouple posts on the sample holder will make firm contact with the thermocouple electrodes partly sitting in the groove of the ceramic block. The ceramic block is also used for the prevention of the short circuit for resistive heating. UHV Kapton insulated copper wires that draw power for resistive heating from the power supply are connected to an adaptor (not shown in Figure 2.9) clamped to the electrical feedthrough. For both heat transfer and electrical connection between the feedthrough and the copper receptacle, three braided silver plated wires are stacked together and soldered to both ends. During cooling, the whole sample stage is cold and contracted. We found that the sample receptacle would be pulled back as far as 0.2 in. by the feedthrough when copper connectors were used. However, by using braided wires over copper connectors, there is more flexibility for the feedthrough to contract during cooling without pulling the sample receptacle back. As a result, the sample remains its position during cooling without the sacrifice of cooling capability.

A clamp mechanism was incorporated in the sample stage to lock the sample holder down when it is engaged. It can force the sample holder into good contact with the sample receptacle in order to improve cooling. An additional benefit of this mechanism is that it can reestablish connection between the thermocouple posts and thermocouple electrodes that is lost due to the contraction during cooling. An electron gun used for e-beam heating is also attached to the clamp mechanism and carefully positioned so that the electron gun is directly facing the backside of the sample when the clamp mechanism is engaged.

The manipulator sample stage is a transferable stage that positions the sample in of the following stages: deposition stage, TPD stage, and spectroscopy stage. It is

important to very precisely align the sample with each stage. It would be convenient if there is a fixed universal coordinate on the manipulator for each stage; however, it is not possible because the position of sample mounted on the sample holder is different. If the coordinate for deposition stage is fixed, for example, the position may work for the samples mounted more or less in the middle, but may not work for the samples mounted slightly towards the side. To solve this problem, we use relative coordinate system. The deposition position is unfixed and varies depending on the position of the sample on the sample holder to make sure the deposition spot is more or less in the middle of the sample surface. The coordinates for TPD and spectroscopy stages are relative to that of deposition position. To find the TPD relative position, a flat silver plate with a 2mm diameter hole in the middle was mounted on the sample holder. A high precision cathetometer was used to align the hole with the exposure mask and the coordinate for this position was recorded. The position where the hole and the orifice of the TPD cone is aligned was also found by the telescope. Therefore, the TPD position relative to the deposition position can be calculated for all the samples regardless of their positions on the sample holders. To find the relative position between the deposition position and the spectroscopy position, the 2mm circular hole on the silver plate sample was filled by gold plate. The position of the gold spot was then found by XPS and recorded. The relative coordinate between spectroscopy and deposition positions was then calculated.

2.2.3.3 Preparation Sample Stage

The design of the sample receptacle is similar to that of the manipulator sample stage. As shown in Figure 2.10, this fixed stage is built on one of five mini ports from a

6-in. Conflat flange. The rest of the ports are used for gas inlets and electrical feedthrough. This sample stage is equipped with a discharge Ar^+ sputter gun, an oven for evaporative film deposition, gas inlets for atomic layer deposition, and a residual gas analyzer, and a quartz-crystal microbalance (QCM). The sample is positioned more or less in the focal point of the ports connecting to the sputter gun and evaporation source. Since the deposition spot and the sputtering area are bigger than the size of the sample, the precise position of the focal point is not needed. Two gas tubes for ALD precursors are positioned directly facing the sample surface, yet they are not blocking the ion beam and particles from the sputter gun and evaporative source. This stage is mainly used for sample cleaning, annealing, and thin film deposition, and it can also be used for TPD experiments for the samples with relatively high vapor pressure.

2.3 References

(1) Roberts, F. S.; Anderson, S. L. *Rev. Sci. Instrum.* **2013**, *84*, 126101.

(2) Kaden, W. E.; Kunkel, W. A.; Roberts, F. S.; Kane, M.; Anderson, S. L. *J. Chem. Phys.* **2012**, *136*, 204705.

(3) Kane, M. D.; Roberts, F. S.; Anderson, S. L. *Int. J. Mass Spectrom.* **2014**, *370*, 1.

(4) Wu, T.; Kaden, W. E.; Kunkel, W. A.; Anderson, S. L. *Surf. Sci.* **2009**, *603*, 2764.

(5) Hiroki, S.; Sakata, K.; Sugiyama, N.; Muramoto, S.; Abe, T.; Murakami, Y. *Vacuum* **1995**, *46*, 681.

(6) Lapicki, A.; Boyd, K. J.; Anderson, S. L. *J. Vac. Sci. Technol. A* **2000**, *18*, 2603.

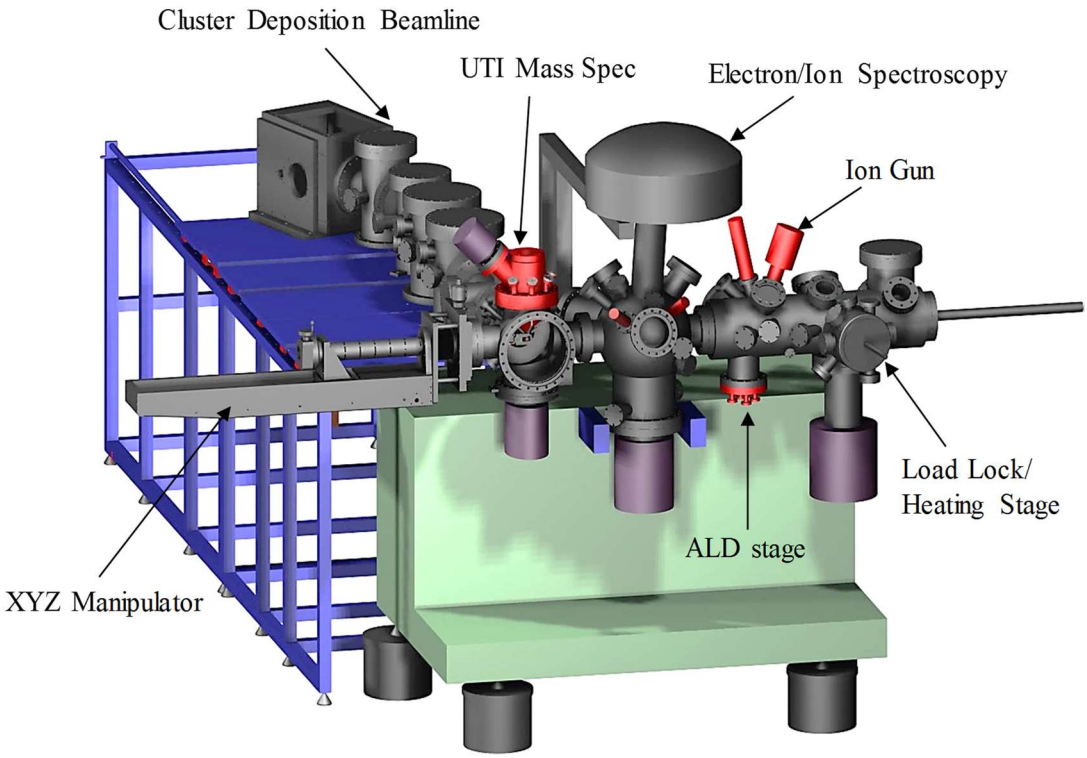

Figure 2.1 3D rendered image of the home-built instrument highlighting the key components.

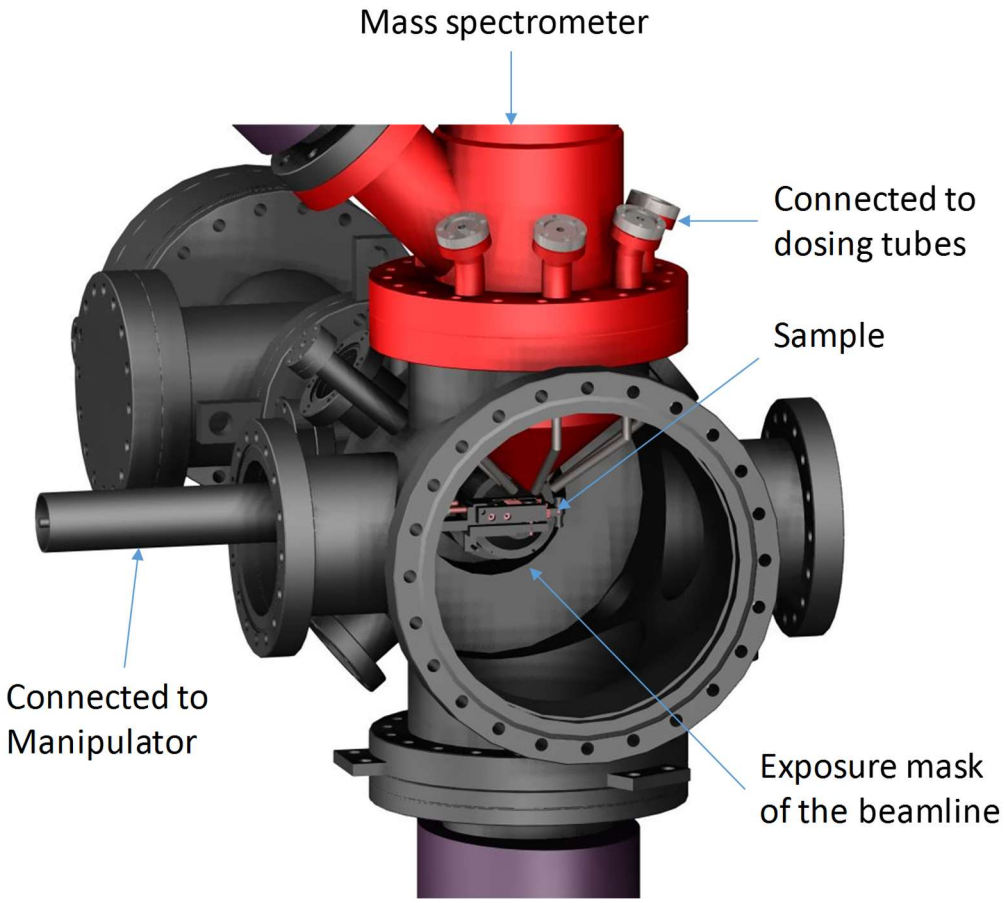

Figure 2.2 Representation of sample position for the differentially pumped mass spectrometer. Note that the sample needs to be rotated 90° counterclockwise to be positioned in front of the exposure mask of the beamline for deposition.

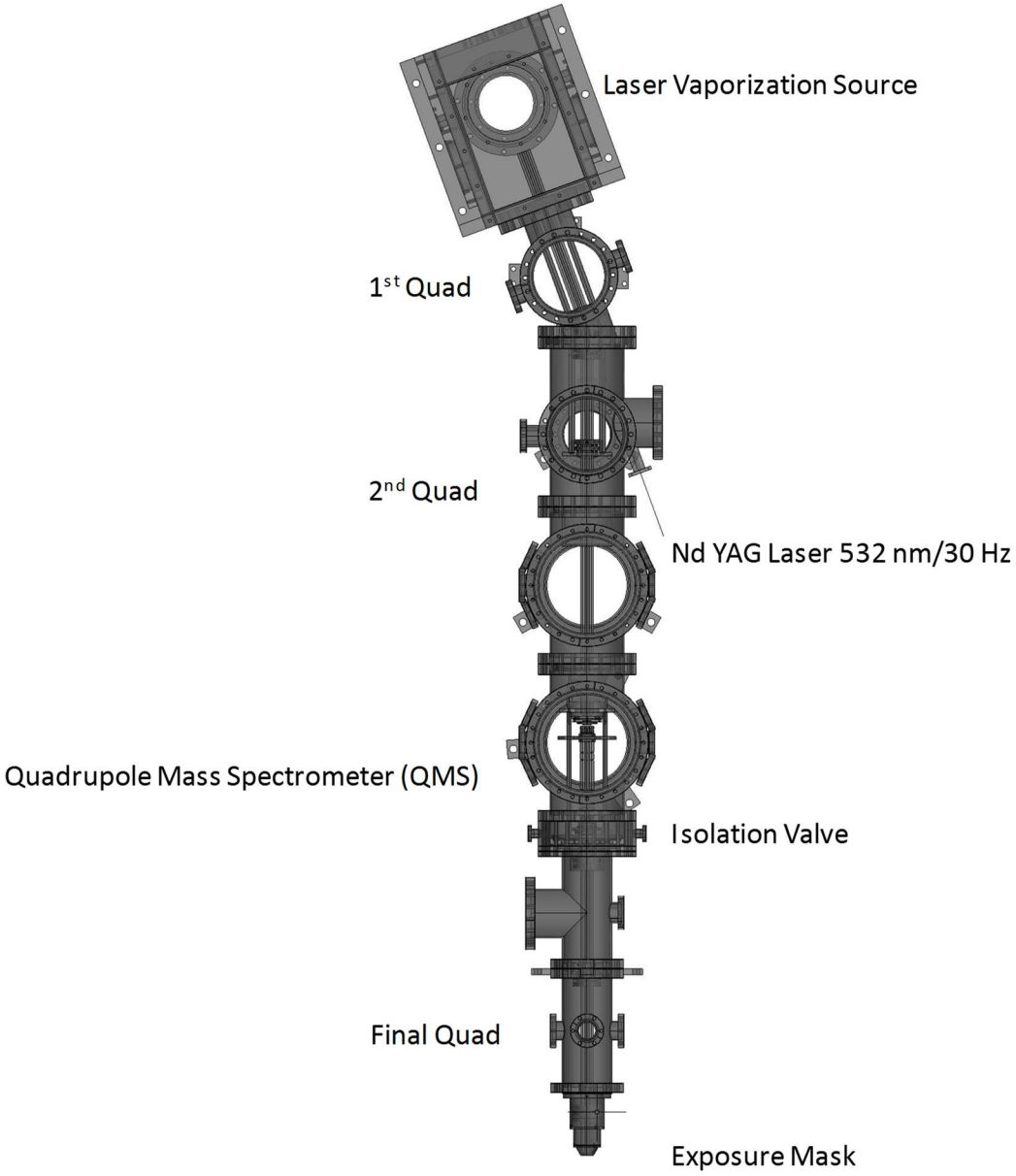

Figure 2.3 Top view of the cluster deposition beamline.

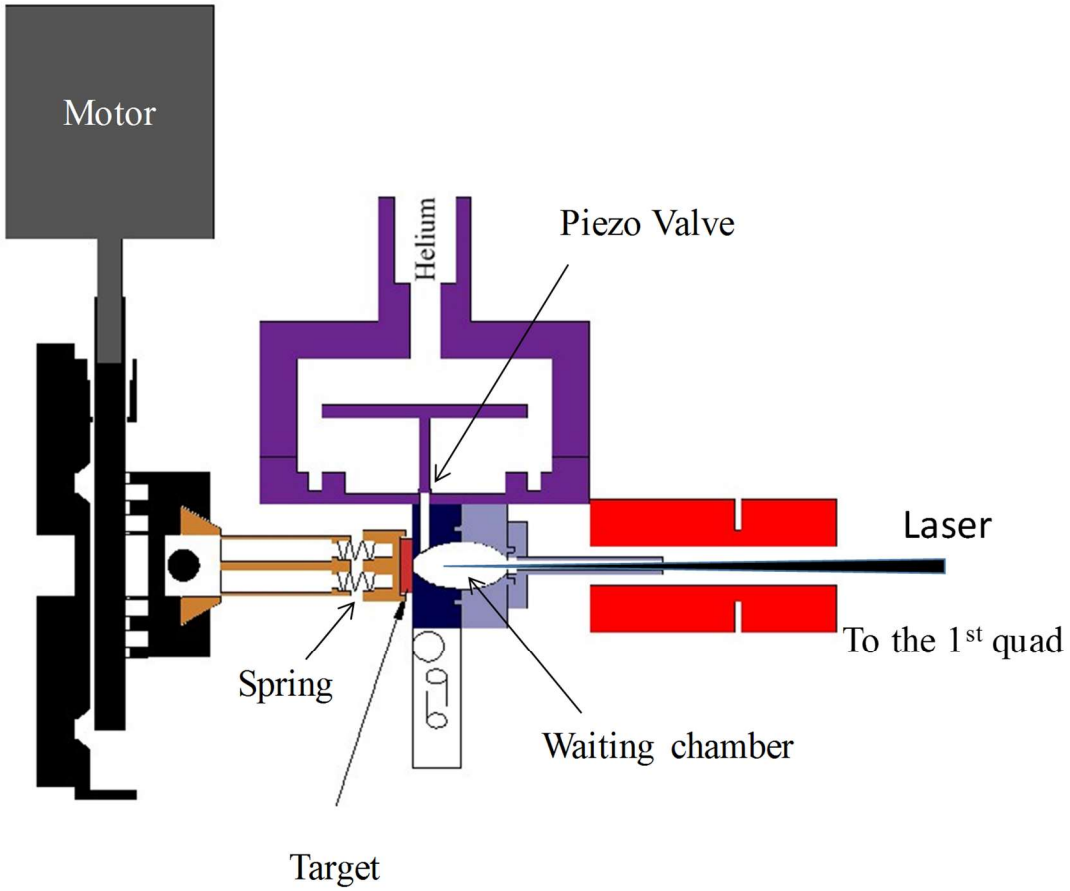

Figure 2.4 Schematic representation of the vaporization source highlighting the major components of the assembly.

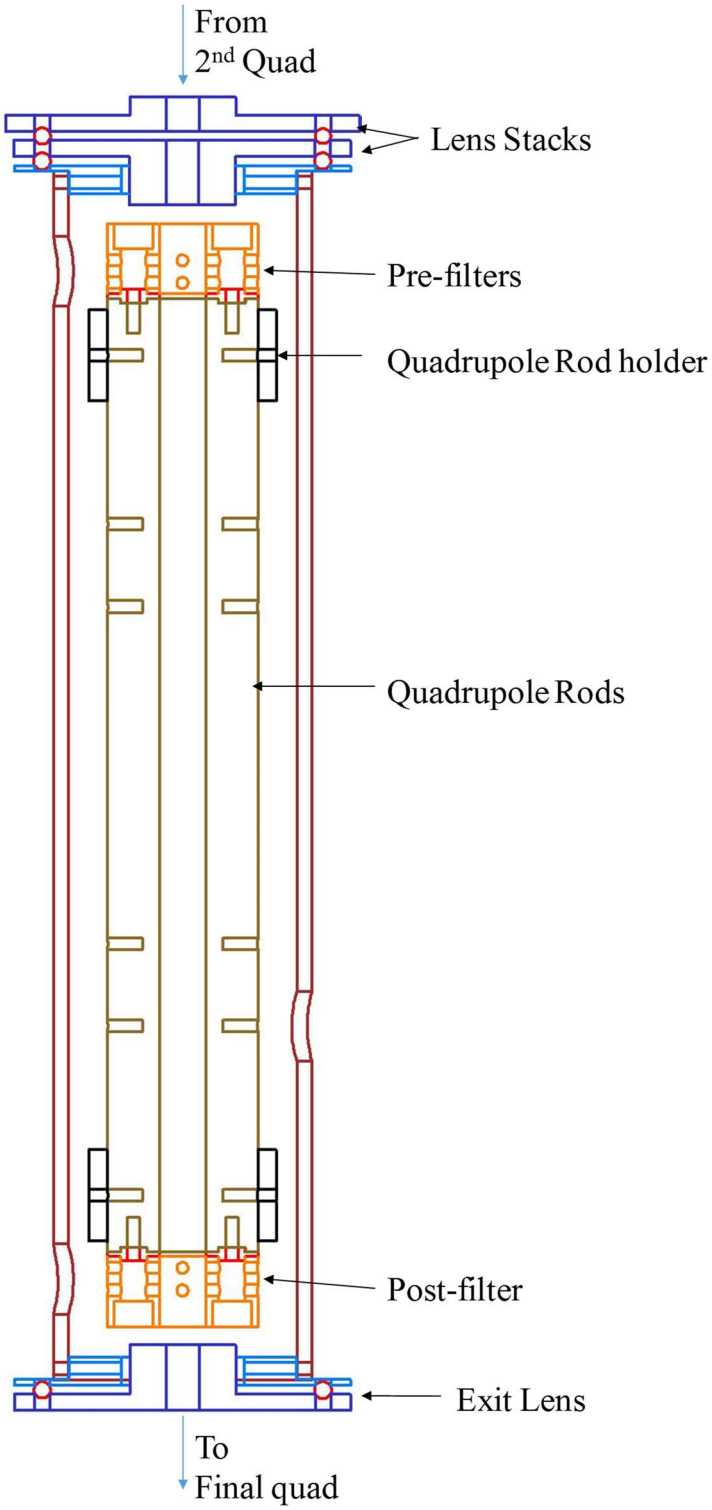

Figure 2.5 Cross-sectional detail of the home-made quadrupole mass filter.

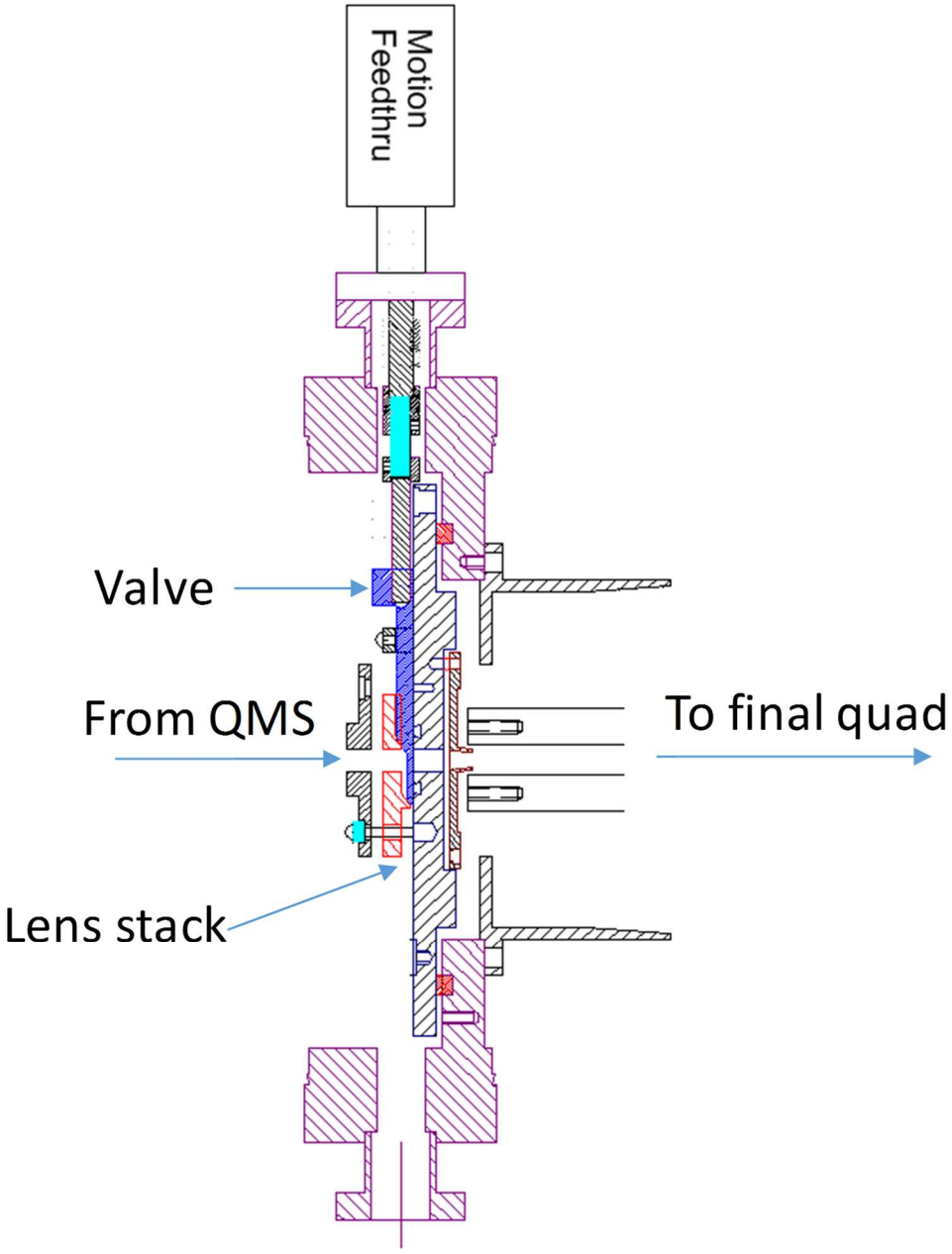

Figure 2.6 Cross-sectional detail of the homemade isolation valve assembly.

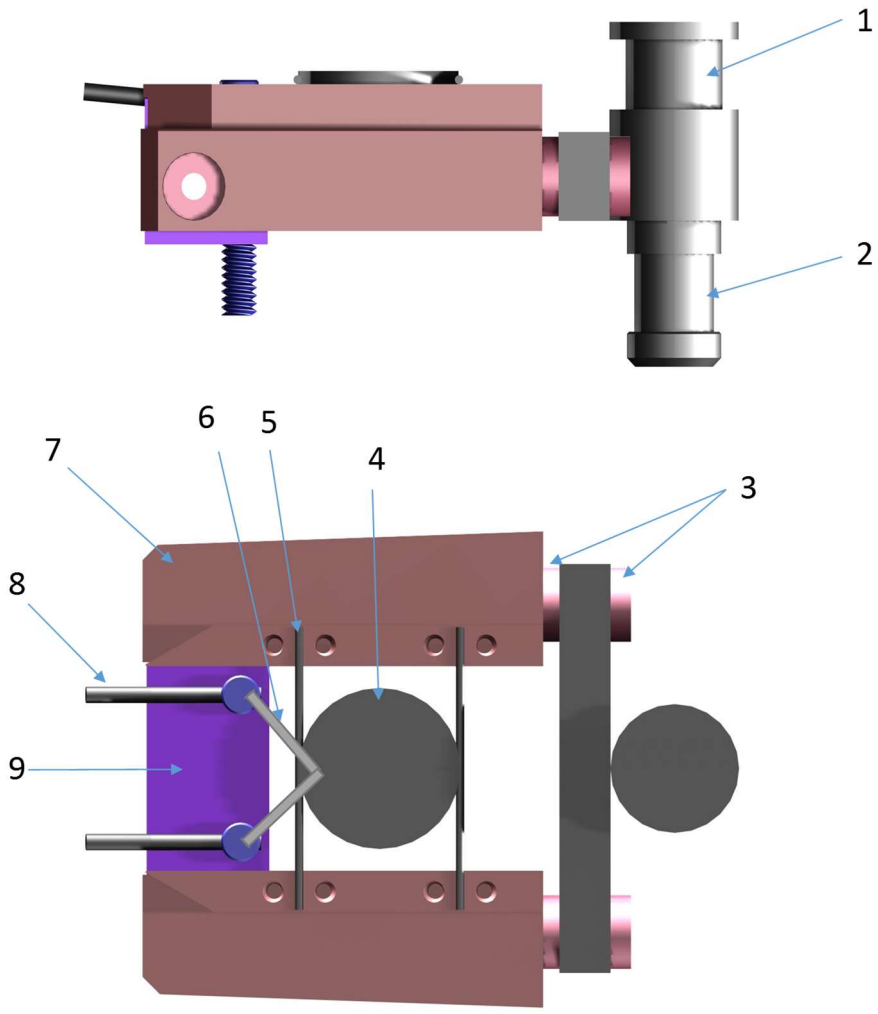

Figure 2.7 Top and side schematic representation of the sample holder: (1) stub for wobble sticks manipulation; (2) pin for sample holder “parking”; (3) ceramic washers for electrical isolation; (4) sample; (5) Ta wires for sample mounting and heating; (6) C-type thermocouple wires; (7) V-shaped sample holder copper body; (8) thermocouple posts for connections with the sample stage; (9) ceramic block for electrical isolation.

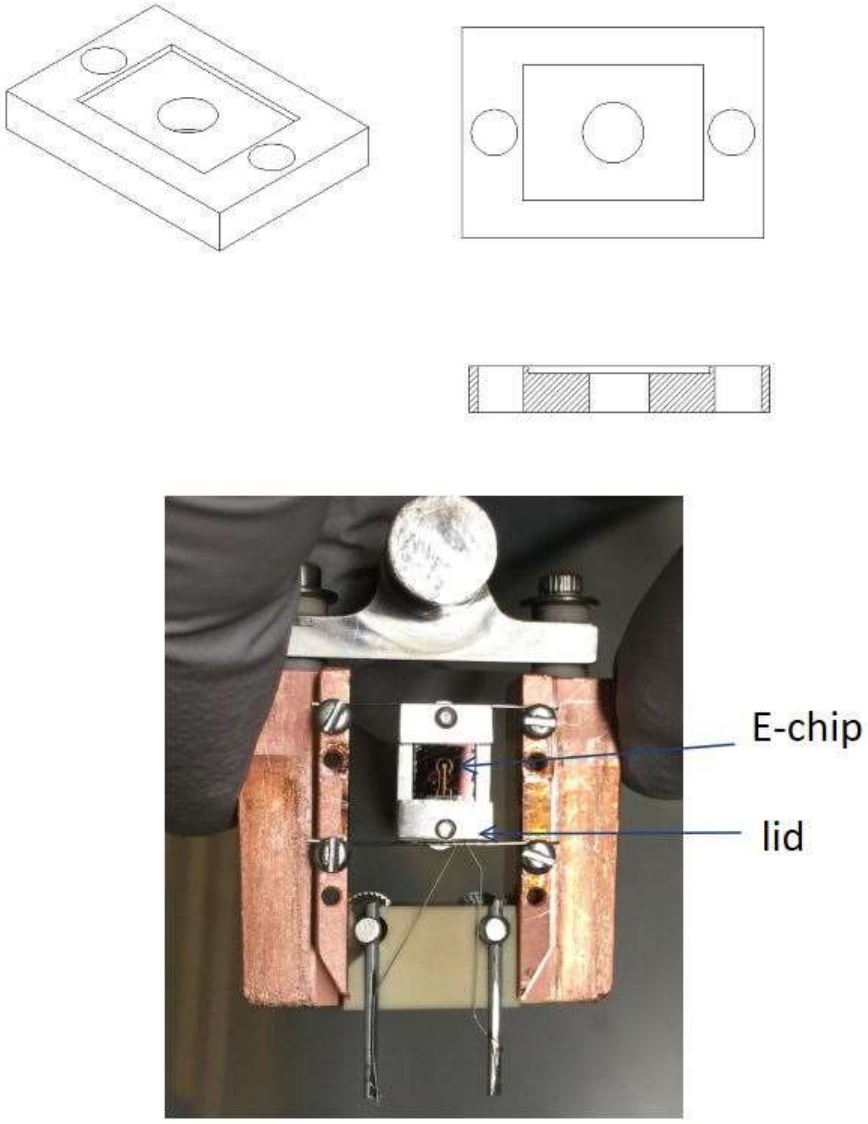

Figure 2.8 Schematic representation of the E-chip holder (top), and the picture of holder with E-chip mounted on the sample holder (bottom).

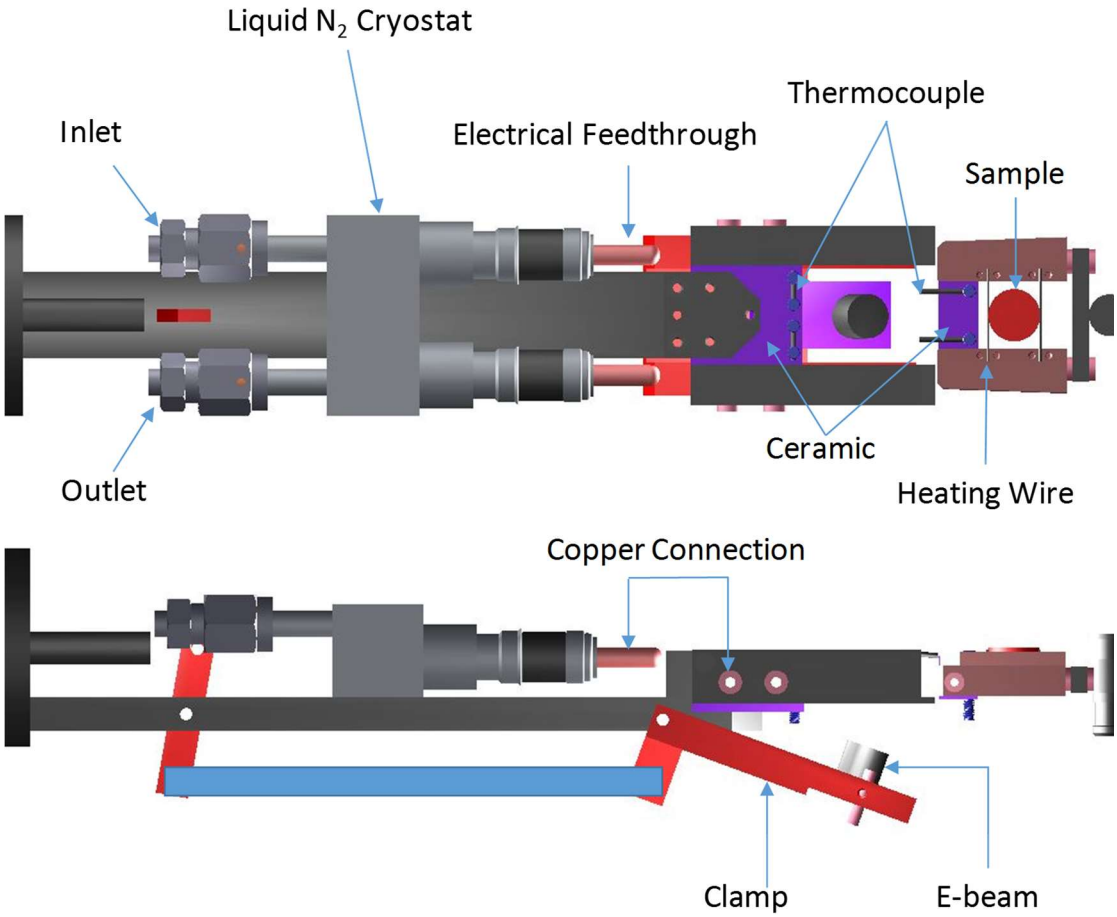

Figure 2.9 Top and side schematic representation of the sample holder and stage on the manipulator.

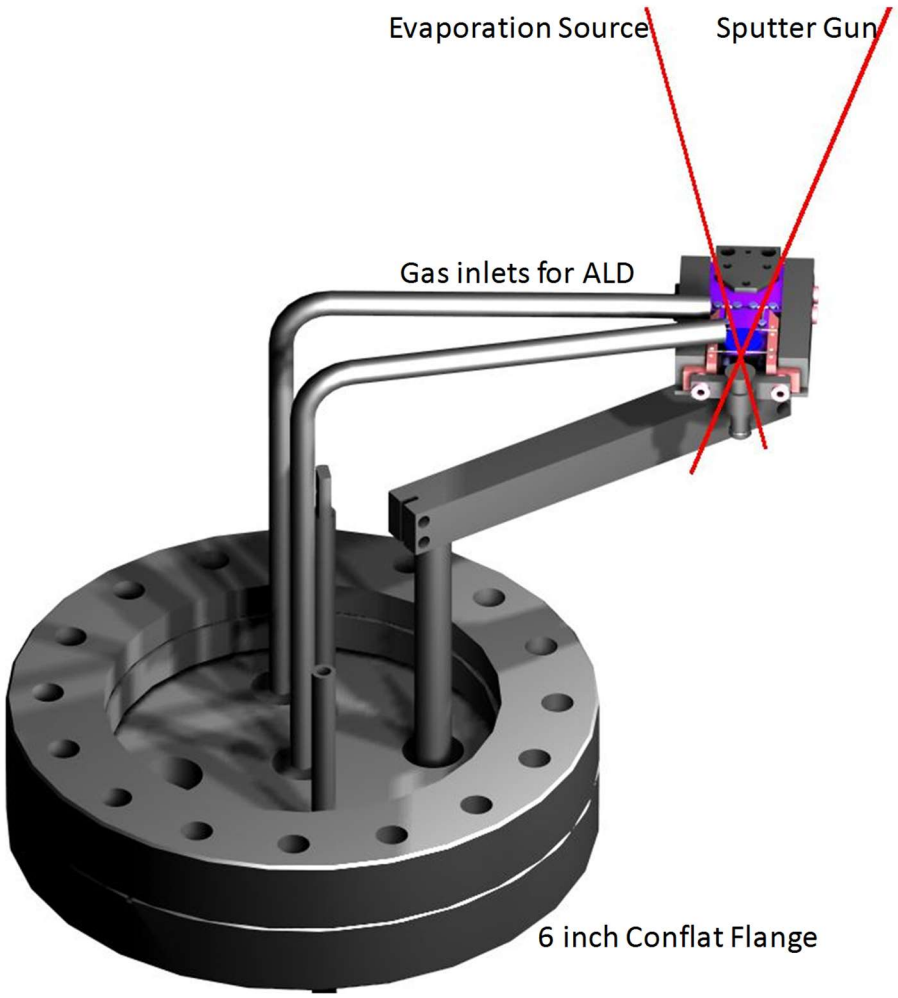

Figure 2.10 Front view of the preparation sample stage and the key components are highlighted.

Table 2.1 Typical operating conditions of beamline elements for depositing Pt_{24} clusters on the sample.

Element	Typical operating conditions
Float Voltage	-65 V
Source foreline pressure	231 mTorr
Focus lens	-62 V
He pulse Delay	0.0328 s
Laser power pulse timing	290 μs
Source float voltage	3 V
Bending lens (left)	-49.09 V
Bending lens (right)	-14.69 V
1st Quad RF	376 V, 2.0 MHz
1st Quad DC	25.32 V
2nd Quad RF	387 V, 2.2 MHz
2nd Quad DC	-11.36 V
Mass dial	5.4
QMS pole bias	10
Δ M	3
Pre filer	0.4 V
Post filter	-14 V
1st entrance lens	-83.3 V
2nd entrance lens	-264.8 V
Baseplate	-314 V
Holder	8.8 V
Skimmer	-24 V
Exit lens	-314 V
Can	-49 V
Exposure mask	-275 V

CHAPTER 3

INHERENT SIZE EFFECTS ON XANES OF NANOMETER METAL CLUSTERS: SIZE-SELECTED PLATINUM CLUSTERS ON SILICA

Yang Dai, Timothy J. Gorey, Scott L. Anderson, Sungsik Lee, Sungwon Lee, Soenke Seifert, and Randall E. Winans. Inherent size effect on XANES of nanometer metal clusters: size-selected platinum clusters on silica. Reprinted with permission from *J. Phys. Chem. C,* **2017,** *121* (1), pp 361-374.

THE JOURNAL OF PHYSICAL CHEMISTRY C

Article

pubs.acs.org/JPCC

Inherent Size Effects on XANES of Nanometer Metal Clusters: Size-Selected Platinum Clusters on Silica

Yang Dai,[†] Timothy J. Gorey,[†] Scott L. Anderson,*[,§,†] Sungsik Lee,[§,‡] Sungwon Lee,[‡] Soenke Seifert,[‡] and Randall E. Winans[‡]

[†]Chemistry Department, University of Utah, Salt Lake City, Utah 84112, United States

[‡]X-ray Science Division, Argonne National Laboratory, 9700 South Cass Avenue, Argonne, Illinois 60439, United States

Supporting Information

ABSTRACT: X-ray absorption near-edge structure (XANES) is commonly used to probe the oxidation state of metal-containing nanomaterials; however, as the particle size in the material drops below a few nanometers, it becomes important to consider inherent size effects on the electronic structure of the materials. In this paper, we analyze a series of size-selected Pt_n/SiO_2 samples, using X-ray photoelectron spectroscopy (XPS), low energy ion scattering, grazing-incidence small-angle X-ray scattering, and XANES. The oxidation state and morphology are characterized both as-deposited in UHV, and after air/O_2 exposure and annealing in H_2. The clusters are found to be stable during deposition and upon air exposure, but sinter if heated above ~150 °C. XANES shows shifts in the Pt L_3 edge, relative to bulk Pt, that increase with decreasing cluster size, and the cluster samples show high white line intensity. Reference to bulk standards would suggest that the clusters are oxidized; however, XPS shows that they are not. Instead, the XANES effects are attributable to development of a band gap and localization of empty state wave functions in small clusters.

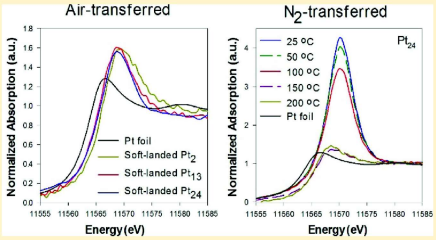

INTRODUCTION

X-ray absorption near-edge spectroscopy (XANES) is a powerful method for *in situ* probing of materials such as catalysts under operating conditions. XANES involves excitation of an electron from a core orbital to empty states above the Fermi level (E_F) for the sample. Because the core level energies are element-specific, XANES can probe the electronic environment of atoms of different elements present in the sample. Two features in XANES are typically of greatest interest. The energy of the absorption onset, or edge, is determined by the energy required to promote an electron from the core level into the lowest unoccupied orbital or state (LUMO). In addition, the intensity of the so-called white line—an absorption maximum that often appears just above the edge—is sensitive to the density of unoccupied states and the transition probabilities to them from the initial core level.[1−3]

Detailed interpretation of XANES requires knowledge of the core orbital energy, the density and energies of unoccupied orbitals, and how these change with sample oxidation state, support, particle size, etc. In addition, however, the transition energies are strongly affected by relaxation in the absorption final state, which may also depend on oxidation state and particle size. There are several theoretical studies, primarily of isolated (i.e., unsupported) clusters, which are discussed below. For most experiments, the required information is not available, and calculating it *ab initio* is infeasible for many samples. Therefore, XANES is often interpreted by comparing spectra for samples of interest, to spectra for bulk reference materials, such as the bulk metal, metal oxides, or other metal compounds.

For example, changes in edge energies and white line intensities can be used to infer changes in the oxidation state of catalyst particles induced by operating conditions. In many cases, the edge energy increases with increasing metal oxidation state, because the electron-poor environment on the metal atoms stabilizes the initial core level.[4,5] White line intensity also frequently increases with metal oxidation state, because oxidation depopulates orbitals near E_F and can change orbital hybridization.[1,6,7]

For metal particles smaller than a few nanometers, particle size can strongly affect the metal electronic structure, and therefore can also affect XANES. For example, the binding energy of core orbitals can be strongly size dependent due to size effects on screening and relaxation in the XANES core-hole final state. This effect is well-known in X-ray photoelectron spectroscopy (XPS), giving rise to size-dependent binding energy (BE) shifts of 1.5 eV or more, relative to the BE for bulk metal.[8−10] For small Pt clusters on Al_2O_3[11] or SiO_2,[12] UV photoelectron spectroscopy (UPS) reveals band gaps that increase with decreasing size, and such band gaps affect both

Received: October 7, 2016
Revised: December 9, 2016
Published: December 12, 2016

DOI: 10.1021/acs.jpcc.6b10167
J. Phys. Chem. C 2017, 121, 361−374

the energy and density of the unoccupied states that are populated in XANES. Rehybridization of valence orbitals for oxide-supported metal clusters[13] and atoms[14] also affects the density of states and can significantly affect core level binding energies as well. These, and other considerations discussed below, suggest that there should be inherent effects of particle size on XANES, which could be large for samples containing metal centers in the few nanometer or smaller size range.

There is great current interest in "single atom catalysts", i.e., catalysts where the support is designed to stabilize isolated atoms and small clusters of a catalytically active metal.[15−20] XANES has been used to probe such materials,[21] and one obvious question is whether or not interpretation by reference to bulk standards is reasonable for such small metal centers.

In this paper, we present a study of size-selected Pt_n/silica samples, prepared by both soft- and hard-landing of mass-selected Pt_n (n = 2, 13, 24) on oxidized silicon supports (SiO_2/Si) in ultrahigh vacuum. *In situ* XPS and low energy ion scattering spectroscopy (ISS) were used to probe the morphology and electronic properties of the samples, both as-prepared, and after exposure to CO, O_2, or air, and after annealing either in UHV or in an H_2 flow. Samples were also characterized by grazing incidence small-angle X-ray scattering (GISAXS) to measure the particle size, both at room temperature and after annealing at different temperatures. Grazing-incidence X-ray absorption spectroscopy (GIXAS)[22] was used to measure XANES under different conditions. The conclusion from the study is that, not surprisingly, there are substantial size effects on XANES, which must be taken into account when interpreting XANES for particles in the few nanometer or subnanometer size range.

EXPERIMENTAL METHODOLOGY

Preparation of Supported Size-Selected Pt Clusters. Pt_n/SiO_2 samples were prepared by depositing Pt_n^+ on 10 × 14 mm sections of an oxidized Si wafer. Deposition and *in situ* sample analysis were carried out using a new cluster deposition instrument, shown in Figure S1. The instrument includes a cluster deposition beamline (shown in Figure S2), a load lock chamber for sample exchange (base pressure <10^{-7} Torr), and an ultrahigh vacuum (UHV) system divided into three separately pumped sections. These are a "prep" chamber (8 × 10^{-10} Torr), a "main" section (2.5 × 10^{-10} Torr), and a chamber housing a mass spectrometer that samples gas from the main section through a 3 mm aperture. Each section has both turbomolecular and titanium sublimation pumps.

Samples are mounted on homemade transferrable sample holders, improved from an earlier design,[23] to allow both resistive and e-beam heating. The sample holders can be inserted into copper/ceramic receptacles for cooling, and to make connections for heating and temperature monitoring. Positioning repeatability is estimated to be better than 50 μm. Samples are introduced into the system through the load-lock chamber, which also houses a receptacle stage allowing samples to be heated to ∼1200 K. In the prep chamber, the sample is manipulated using a magnetic transporter, and can also be transferred to a fixed stage for heating to ∼1200 K. This stage is also equipped with a discharge sputter gun, an oven for evaporative film deposition, gas inlets for atomic layer deposition, a residual gas analyzer, and a quartz crystal microbalance. After opening an isolation valve, the sample can be passed into the main UHV section, where it is either transferred to a rotary "parking" stage that can store six samples, or into a receptacle attached to a precision *XYZ*/rotation manipulator. While on the manipulator, the sample temperature can be controlled between ∼130 and >2200 K, using a combination of liquid N_2 cooling and resistive and e-beam heating.

The manipulator is used to move samples between three positions. In one, the sample is at the focus of a hemispherical energy analyzer, a windowless vacuum UV lamp,[24] dual anode and monochromatic X-ray sources, and an electron impact ion gun, allowing sample cleaning by sputtering/annealing, and analysis by UPS, XPS, and ISS. In the second position, the sample is <1 mm from the deposition mask of our cluster deposition beamline, allowing a well-defined 2 mm diameter spot of size-selected clusters to be deposited. In the third position, the sample is just in front of the differential pumping aperture for a mass spectrometer (UTI 100 quadrupole with Extrel electronics) allowing analysis of species desorbing from the sample. In the mass spectrometry position, the sample is also at the focus of 6 tubes that deliver either continuous or pulsed gas doses.

SiO_2/Si substrates were prepared by dicing an oxidized Si wafer into 10 × 14 mm pieces, using n-doped Si to give sufficient conductivity to minimize charging during deposition and analysis. The Si substrates were clipped to a tantalum backing plate that was spot-welded to tantalum heating wires, which were attached to the copper sample holder. The sample temperature is monitored by a type C thermocouple spot-welded to the Ta backing plate. For these experiments, the substrates were cleaned by heating in UHV to 800 K for 20 min prior to cluster deposition. The absence of significant contaminants was verified by XPS and ISS (on different samples, to avoid beam damage).

The cluster deposition beamline is similar to one we have described previously.[25−27] A beam of Pt_n^+ clusters is generated by laser vaporization of a rastering Pt target, with the Pt plasma entrained in a pulsed helium flow. After expanding into vacuum, cluster cations are collected and guided by a series of radio frequency (RF) quadrupoles through a total of 6 stages of differential pumping, before entering the main UHV section for deposition. During deposition, the main section pressure increases by 2 × 10^{-10} Torr of helium. At the midpoint of the beamline, clusters are mass selected by a homemade quadrupole filter controlled by 440 kHz electronics (Extrel 150-QC) giving a nominal mass range to 16 000 Da. The impact energy of the Pt clusters on the sample is controlled by electrically floating the beamline with respect to the sample, which is grounded through an electrometer. The deposition energy is calibrated by retarding potential analysis of the beam on the sample. Most of the experiments discussed below were done with samples prepared by deposition at ∼1 eV/atom energy, which we will refer to as "soft landing". For comparison, a few samples were prepared by "hard-landing" clusters at ∼3.75 eV/atom. Deposition is monitored continuously via the Pt_n^+ neutralization current, and was stopped at a coverage corresponding to 1.50 × 10^{14} Pt atoms *per* cm^2 (∼10% of a close-packed Pt monolayer), deposited in the form of different size Pt_n. Samples for GISAXS and XANES studies were made by depositing four cluster spots to form a stripe along the long axis of the substrate, for better overlap with the grazing incidence X-ray footprint.

An issue that potentially could affect interpretation of the grazing-incidence X-ray experiments is the extent to which Pt penetrates the SiO_2/Si surface—a process that requires

DOI: 10.1021/acs.jpcc.6b10167
J. Phys. Chem. C 2017, 121, 361−374

displacement of one or more Si or O atoms from their initial lattice positions. Cowen et al. recently calculated displacement probabilities for Si and O atoms in silica for a wide range of initial atomic kinetic energies and angles, validating their results against previous theory and experimental displacement data.[28] The energies required to give 1% displacement probability for O and Si atoms are ~11 and ~25 eV, respectively, and for 33% displacement probability the energies are ~25 and ~50 eV, for O and Si, respectively. The worst case scenario would be for the cluster's deposition energy to be transferred to a single Si or O atom in the substrate. Under soft-landing conditions (1 eV/atom) the total energy for Pt_2 is just 2 eV—far too low to drive Si or O displacement. For Pt_{13}, the displacement probability in this scenario would be ~1% for O and negligible for Si, and for Pt_{24}, the total energy (24 eV) would be sufficient to drive O atom displacement with reasonable (~30%) probability, but Si displacement would still be at the 1% level.

Note, however, that the assumption that the cluster's kinetic energy is all transferred to a single substrate atom is unrealistic for all but the smallest clusters. For example, Pt_{24}, if spherical with the bulk density, would have a diameter of 0.88 nm, compared to the ~0.15 nm atomic spacings in silica. If we estimate the impact "footprint" as half the cluster cross sectional area, roughly nine substrate atoms would be impacted, making it unlikely that any one atom would receive enough energy transfer to exceed the displacement threshold. In addition, clusters can deform on impact, consuming some of the impact energy in the process, and also increasing the footprint area and number of substrate atoms over which the deposition kinetic energy is distributed. We conclude that for our soft-landing conditions, clusters in the size range studied should remain entirely on top of the SiO_2/Si surface. For hard-landing of Pt_{24}, the total cluster kinetic energy (90 eV) should be large enough to drive some substrate atom displacement and mixing of Pt atoms into the surface layer, but still far too low to drive deep penetration into the substrate.

After cluster deposition, samples were analyzed by a variety of methods. Samples destined for XANES and GISAXS studies were characterized by XPS, then transferred out of the UHV system, and placed in a custom-made shipping container and shipped to Argonne. Most samples were transferred and shipped in air, however, one set of Pt_{24}/SiO_2/Si samples was transferred under N_2. For this transfer, the load lock chamber was enclosed in an N_2-purged glovebag, and samples were transferred into the shipping container, which was then sealed inside a metal-sealed housing, all under N_2. On the receiving end, the samples were transferred from the housing to the sealed GISAXS/XANES cell under N_2. Such precautions should have reduced the O_2 exposure by roughly 5 orders of magnitude, compared to the air-transferred samples.

***In Situ* X-ray Photoelectron Spectroscopy.** To verify the cluster coverage and to study effects of different sample manipulations on the electronic properties of the Pt_n clusters, XPS was done *in situ* in the main UHV section, using Al Kα radiation incident at an angle of 54.7°, with electrons detected along the surface normal. Pt 4f spectra were taken for as-prepared samples, and for samples that were heated in either UHV or H_2, or exposed to O_2 or to air. To minimize effects of X-ray damage or adventitious adsorbates, each of these experiments was done on a separately prepared sample.

Low Energy Ion Scattering Spectroscopy (ISS). The 1 keV He^+ scattering was used to examine sample morphology, focusing on how various sample manipulations change the fraction of Pt atoms exposed in the top layer of the sample.[29−31] A He^+ beam current of 0.1 μA was incident on the sample at 45°, and He^+ scattered along the surface normal was analyzed with the hemispherical energy analyzer. A series of ISS measurements was done for each sample. Experiments were done for hard and soft-landed Pt_{24}, for soft-landed Pt_{24} after exposures to CO or O_2, and after annealing in either UHV or in H_2. To minimize complications from He implantation and sputter damage, each experiment was done on a separately prepared sample.

Grazing-Incidence Small-Angle X-ray Scattering. *In situ* X-ray experiments were performed using a unique setup developed at the Sector 12-ID-C at the Advanced Photon Source of the Argonne National Laboratory.[22] The experiments were performed in a home-built reaction cell sealed with Kapton windows and mounted on a computer-controlled goniometer. The cluster sample was placed on the top of a ceramic heater centered in the cell. The heater power was regulated by temperature controller with K-type thermocouple attached to the heater surface. The X-ray beam was scattered off the surface of the sample at grazing incidence angle of 0.15°, which is at the critical angle of the substrate. A 1024 × 1024 pixel two-dimensional CCD detector designed and built at the APS was used for recording the GISAXS images from the sample. Initial measurements on as-deposited samples were made at incident energy of 18 keV with a scattering vector (q) range of 0.008−0.5 $Å^{-1}$ and annealing measurements were done at 11.75 keV with a q range of 0.008−0.33 $Å^{-1}$. The scattering vector was calibrated using silver behenate. The size distributions of the scatterers present on the sample surfaces were determined by fitting the GISAXS data using the Modeling II tool in the Irena package.[32] Note that these samples were prepared by random deposition of gas-phase clusters, and the coverage is such that the average intercluster separation for Pt_{24} was ~5 nm. Given the nature of the oxidized Si substrate, there is no reason to expect substrate-driven ordering of the clusters.

X-ray Absorption Near Edge Structure. Grazing incidence X-ray absorption spectra (incidence angle =0.15°) were collected at the Sector 12-BM-B and 12-ID-C stations at the Advanced Photon Source of the Argonne National Laboratory using fluorescence detectors (13 element Ge detector and Vortex 4 element SDD) mounted perpendicular to the X-ray beam and parallel to the sample surface.[22,33,34] The incident X-ray energy was calibrated using Pt foil (EXAFS Materials) by setting the inflection point in the first differential XANES to 11564 eV. The edge energy was defined as the position of the inflection point, and determined by using the IFEFFIT interactive software package (with ATHENA and ARTEMIS graphical interfaces).[35] The effects of parameters such as normalization energy range and background were tested, and confirmed to be minimal. The energy of Pt L_3 edge was calibrated based on Pt foil with <0.1 eV accuracy, and was checked for every sample scan.

■ RESULTS

Particle Size Characterization by GISAXS. From the perspective of understanding what the XANES results reveal about the samples, the first question is whether the clusters remain intact during deposition and transfer to Argonne for analysis. GISAXS experiments were performed for Pt_2/SiO_2/Si, Pt_{13}/SiO_2/Si, and Pt_{24}/SiO_2/Si samples as well as for a control SiO_2/Si sample, all at room temperature. For soft-landed Pt_{24},

DOI: 10.1021/acs.jpcc.6b10167
J. Phys. Chem. C 2017, 121, 361−374

both air- and N_2-transferred samples were studied. Figure 1a shows typical raw scattering data, in this case for a soft-landed

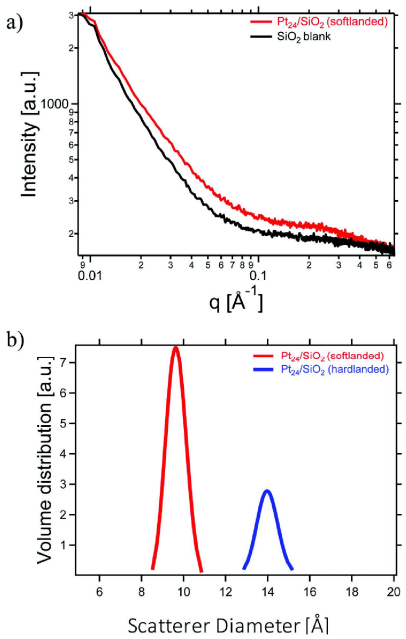

Figure 1. (a) Raw GISAXS for soft-landed $Pt_{24}/SiO_2/Si$ and for a blank SiO2/Si sample. (b) Size distributions extracted by fitting data as in part a for soft- and hard-landed $Pt_{24}/SiO_2/Si$.

$Pt_{24}/SiO_2/Si$ sample transferred in air, and for a clean SiO_2/Si blank. The presence of the Pt_{24} leads to significant additional scattering in the q range between 0.02 and 0.4 $Å^{-1}$. GISAXS showed no evidence of any anisotropy in the particle shape, but this is not surprising. Pt_{24} may simply be too small to show well developed shape. Furthermore, small metal clusters, including Pt, often show a range of thermally accessible low-lying isomers,[36,37] both in the gas phase and on surfaces. Therefore, given the random nature of the deposition process, it is almost certain that our results average over a range of cluster structures.

Figure 1b shows the scatterer size distributions extracted by fitting the data for both soft- and hard-landed samples. Fitting was attempted assuming particle shapes that were spherical, hemispherical, and flattened spherical with different aspect ratios. The data were best fit with the hemispherical or flattened spherical models, suggesting that the Pt clusters tend to flatten on the silica surface. For soft-landed Pt_{24}, the fitted scatterer size distribution is quite narrow, peaking at 0.96 nm diameter in the hemisphere model. A hemisphere of this size with bulk density would contain only ~16 atoms, however, given the low Pt−Pt coordination in such small particles, some contraction of Pt−Pt bonds would not be surprising, i.e., hemispheres or flattened spheres of this size could contain additional atoms. We conclude that the GASAXS results are consistent with the deposited Pt_{24} remaining mostly intact at room temperature, even with several days of air exposure during sample transfer. This conclusion is in line with scanning transmission electron microscopy results for small Pt_n clusters deposited under similar conditions on carbon, which showed no evidence for ripening or sintering even after months of air exposure.[38]

The scatterer size for hard-landed Pt_{24} was significantly larger, with fitted diameter of ~1.48 nm, which would correspond to a spherical Pt cluster of bulk density containing ~112 atoms. It seems unlikely, however, that impact at higher energies would enhance diffusion and sintering. Indeed, there are a number of reports demonstrating that depositing clusters at increased energies results in support defect formation that tends to anchor the clusters, stabilizing them against sintering.[39−46] While our hard-landing energy (3.75 eV/atom) is relatively low, for Pt_{24} the 90 eV total energy is certainly high enough to cause significant damage to the clusters and/or substrate. GISAXS measures scattering from disordered volumes in the near-surface region of the Si samples, and by measuring with photon energy of 11.75 keV, just above the Pt edge, we are particularly sensitive to disorder involving Pt atoms. We previously used ISS and XPS to probe the effects of impact energy on deposition of Ir_n^+ (n = 1−15) on TiO_2, and found that embedding of clusters into the TiO_2 substrate became significant at total energies in the 80−100 eV range.[30] Because Pt and Ir have similar atomic mass and cohesiveness, it is reasonable to expect partial embedding of hard-landed Pt_{24} into the SiO_2/Si support, creating a larger disordered Pt volume. Because the hard-landed Pt_{24} has complex morphology, we focus the discussion on the simpler, soft-landed samples.

For $Pt_2/SiO_2/Si$ and $Pt_{13}/SiO_2/Si$, the GISAXS showed no significant difference in scattering in the q range of interest, between the samples with clusters and the SiO_2/Si blank. This absence of scattering is despite the Pt coverage being the same as in the Pt_{24} samples. Apparently these clusters are simply too small to give rise to significant SAXS signal. While it is unfortunate that we could not directly measure the size distributions for the Pt_2 and Pt_{13} samples, the absence of SAXS signal does show that agglomeration and ripening processes do not produce clusters in the detectable size range. XPS, below, provides further evidence supporting this conclusion.

The thermal stability of the deposited clusters was probed by monitoring GISAXS for a soft-landed $Pt_{24}/SiO_2/Si$ sample as it was annealed to different temperatures in a flow of 4% H_2 in helium and 800 Torr total pressure. As shown in Figure 2a, no significant changes in the scattering were observed for annealing temperatures of 50 or 100 °C, however, at 150 and 200 °C there was substantial signal growth in the q range around 0.1 $Å^{-1}$. Note that previous work has shown that annealing of SiO_2/Si substrates of this type up to 200 °C, does not lead to any change of scattering.[33,47] The temperature dependent line cut (horizontal) data were fit to obtain the particle size distributions shown in Figure 2b. For temperatures up to 100 °C, the scattering is fit by a size distribution peaking at ~1 nm, as in Figure 1b. At 150 °C, the peak of the corresponding size distribution was still close to 1 nm, but with a tail extending to ~5 nm, indicating significant cluster agglomeration and/or ripening. By 200 °C, the subnanometer clusters had essentially disappeared, and the peak of the distribution shifted to 2.1 nm, with a tail extending to ~5 nm. It may seem odd that the distribution narrows at 200 °C,

DOI: 10.1021/acs.jpcc.6b10167
J. Phys. Chem. C 2017, 121, 361−374

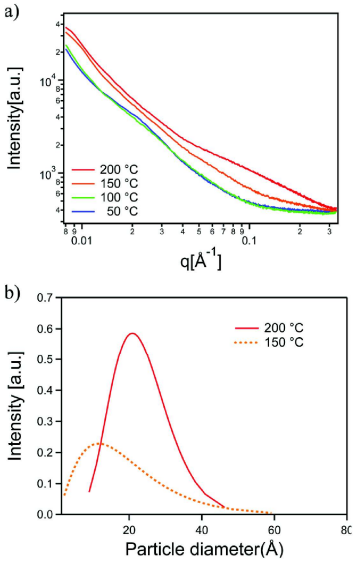

Figure 2. (a) GISAXS intensity (horizontal cut) change of soft-landed $Pt_{24}/SiO_2/Si$ sample during the heating cycle, as temperature was increased from 50 to 200 °C in H_2. (b) Fitted particle size distributions obtained at 150 °C (dashed) and 200 °C (solid).

however, consider the number of atoms in the particles. For spherical Pt particles with bulk density, 2 nm corresponds to ~280 atoms, and 5 nm would be ~4300 atoms. Given our low initial coverage of Pt_{24}, it is not unreasonable that the size should reach a high temperature limit, because a given area on the SiO_2 has only a limited number of Pt atoms.

Morphology and Adsorbate Binding Analysis by ISS. He^+ ion scattering provides additional information regarding the effects of hard landing, adsorbate exposure, and annealing in H_2 on sample morphology. Figure 3a shows a typical ISS spectrum for $Pt_{24}/SiO_2/Si$. Peaks in the spectrum result primarily from events where He^+ scatters from a single atom in the topmost layer of the sample, while multiple-scattering events contribute the broad background at low energy. The energy retained by He^+ in a single-scattering event gives the target atom mass, as indicated by the labels.[48] The Si and O peaks are much larger than that for Pt because the Pt coverage is low, and because ions were collected from an area larger than the 2 mm cluster spot. We are primarily interested in how the Pt peak intensity, i.e., the fraction of Pt in the surface layer, changes when samples are heated or exposed to adsorbates. To account for any day-to-day variation in He^+ beam intensity, the Pt ISS intensity has been normalized to the sum of the Si and O intensities. It should be noted that the temperatures examined are well below the 1600 °C melting temperature of silica, and that none of the adsorbates studied here adsorb on silica in the temperature range of the experiments. As a result, there are no changes to the Si or O ISS intensities from adsorbate exposures. Prolonged exposure to the He^+ beam does result in changes to

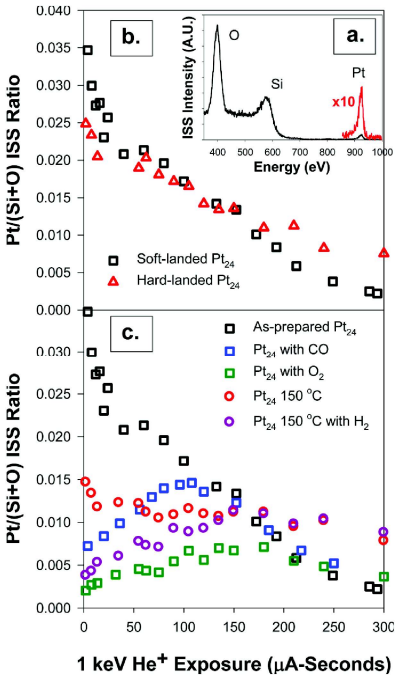

Figure 3. (a) Typical ISS spectrum for $Pt_{24}/SiO_2/Si$. (b) Pt ISS intensity, normalized to the sum of Si and O signals, as a function of 1 keV He^+ ion exposure for soft- and hard-landed $Pt_{24}/SiO_2/Si$. (c) Normalized Pt ISS intensity for as-deposited Pt_{24}, and samples exposed to CO or O_2, annealed in vacuum or in H_2.

the Si-to-O ratio, however, the sum of Si and O intensities is essentially exposure-independent.

Figure 3b shows how the Pt ISS intensity changes with He^+ exposure, for as-prepared samples made by soft- and hard-landing Pt_{24} clusters on SiO_2/Si. The He^+ beam is left on throughout the experiment, with ISS scans run periodically. Note that the Pt signal for both samples peaks at zero He^+ exposure, decaying slowly as Pt is lost from the surface layer by He^+ sputtering. For the low He^+ beam current used here, monotonic decay is characteristic of samples where the clusters have little or no adsorbate coverage that would attenuate scattering signal from the underlying Pt.

Note that the initial signal is lower for the hard-landed Pt_{24} sample, showing that it initially exposes a smaller fraction of the Pt atoms in the surface layer, compared to the soft-landed sample. The decay rate is slower for the hard-landed sample, however, such that the signal remaining at long times is much higher. This pattern is consistent with the soft-landed Pt_{24} clusters remaining on the surface of the SiO_2 support, as might be expected, with morphology that exposes a substantial fraction of the Pt atoms in the surface layer. This morphology results in high initial Pt signal, but also means that the Pt sputter loss rate is high. The lower initial intensity and slower

DOI: 10.1021/acs.jpcc.6b10167
J. Phys. Chem. C 2017, 121, 361−374

decay for hard-landed Pt_{24} is consistent with the cluster being partially embedded in the top layers of the SiO_2/Si substrate. A smaller fraction of Pt is exposed initially, but as top layer Pt, Si, and O atoms are lost by sputtering, additional Pt is exposed, resulting in a slower signal decay rate. Similar effects of cluster embedding on ISS were observed for Ir_n hard landed on both TiO_2[30] and SiO_2.[49]

Figure 3c compares the Pt ISS signal for separate samples of soft-landed Pt_{24}, measured as-deposited, or after exposure to either CO (10 L) or O_2 (~1000 L) at room temperature, or after annealing to 150 °C for 1 h in either UHV or in 10^{-4} Torr of H_2. It can be seen that for the samples exposed to either CO or O_2, the initial Pt signal is strongly attenuated compared to the as-deposited sample, but that the signal increases with He^+ exposure until it matches that for the as-deposited sample. There are three mechanisms by which adsorbates attenuate He^+ scattering from underlying Pt atoms. For an adsorbate (e.g., CO) binding in any site on top of a Pt cluster, there will tend to be some Pt atoms that are inaccessible to He^+ due to "shadowing" by C or O atoms (He^+ is incident at 45°).[48,50] For binding in atop sites, there is an additional "blocking" mechanism, wherein He^+ that scatters from the underlying Pt atom is blocked from reaching the detector (along the surface normal) because the adsorbate is in the way. Finally, more than 99% of He^+ neutralizes during scattering from surfaces,[51−54] and the presence of adsorbates on the clusters tends to reduce the ion survival probability (ISP) for He^+ scattering from the cluster atoms. On the other hand, adsorbates binding to the support or to the cluster periphery tend to have little effect on He^+ scattering from the clusters.[27]

CO binding was studied to give a point of comparison for the other adsorbates, because it is known to bind efficiently to Pt at room temperature, including to small Pt_n on alumina.[11] An exposure of 10 L corresponds to ~2.5 CO molecules impinging *per* surface atom, thus we expect binding sites stable at room temperature to be largely saturated. The ~80% initial attenuation of Pt ISS intensity indicates that the cluster binds enough CO to strongly attenuate scattering from the underlying Pt. For comparison, note that from temperature-programmed desorption of CO from Pt_n/alumina,[11] we estimate that the saturation coverage at room temperature is roughly 0.7 to 0.8 CO *per* Pt atom in the surface layer.

During the initial ~100 μA·s of He^+ exposure, the Pt ISS signal increases slowly, as He^+ sputters CO from the cluster surfaces, exposing underlying Pt.[11,27,30,49,55] CO sputters faster than Pt because CO-Pt bonds are weaker than the bonds that must be broken to remove a Pt atom from a cluster. Finally, at long exposures, the Pt signal decays due to Pt sputtering, with absolute Pt intensity and decay rate that are essentially identical to those for the Pt_{24} sample that was not exposed to CO. This similarity indicates that CO adsorption did not drive any major structural changes in the sample, such as sintering to larger particles.

For the sample exposed to O_2 (3×10^{-7} Torr for 1 h ≈1000 L), the initial attenuation of Pt ISS was even larger than that for CO, and the recovery of Pt intensity with He^+ exposure was substantially slower. The higher attenuation, compared to that from CO saturation, could result from a higher coverage of oxygen, but it could also result from oxygen binding geometries that more efficiently attenuate He^+ scattering from Pt. Pt signal also recovers more slowly after O_2 exposure than in the CO experiment, which suggests stronger Pt−O binding, compared to Pt−CO. In any case, it is clear that for O_2 exposures much smaller than those occurring during transfer in air for GISAXS or XANES, the Pt clusters are covered with adsorbed oxygen in some form.

Another Pt_{24} sample was heated in UHV at 150 °C, to examine thermal effects in absence of adsorbates. This sample showed a ~50% decrease in the initial Pt ISS intensity, and the signal simply decayed during further exposure to the He^+ beam, but more slowly than for the unheated Pt_{24} sample. The lower initial Pt intensity indicates that ~50% fewer Pt atoms were in the surface layer, compared to unheated Pt_{24}, and the monotonic decay rules out adsorbates as the cause (as expected for heating in UHV). Heating, therefore, is shown to transform the Pt_{24} into *thicker* structures, in which only half as much of the Pt is in the surface layer detected by ISS. Thicker Pt structures also account for the slower decay of ISS intensity, because loss of Pt from the top layer simply exposes underlying Pt. From ISS alone, it is not possible to distinguish scenarios where Pt_{24} sinters into larger particles vs simply restructuring into more compact, 3-dimensional shapes without any size increase. GISAXS, where particle growth was observed at 150 °C (in H_2), suggests that sintering is probably a factor.

For comparison, we also did ISS on a sample that was heated during H_2 exposure. This experiment was done by transferring a Pt_{24} sample to the prep chamber, partially closing the gate valve on its pump, and then flowing H_2 through the chamber at 10^{-4} Torr while the sample was heated to 150 °C for 1 h ($\approx 3.6 \times 10^5$ L exposure). After cooling, the chamber was evacuated, and the sample was transferred back to the main UHV section for ISS. The Pt ISS intensity after heating in H_2 was ~4 times lower than that for the sample that was heated in vacuum, i.e., about 8 times lower than for as-deposited Pt_{24}/SiO_2/Si. The fact that the Pt intensity initially increased with He^+ exposure shows that hydrogen adsorbed on the surface must contribute to the initial attenuation. The observation that the Pt intensities and decay rates at large He^+ exposures are essentially identical for the samples annealed in H_2 and in UHV, suggests that the degree of sintering was similar, at least for the relatively low H_2 pressure used.

Such strong attenuation from adsorbed hydrogen is surprising, because the cross section for 1 keV He^+ scattering scales like the atomic number of the target atom.[48] Therefore, the scattering shadows cast by adsorbed H atoms are much smaller than those cast by C or O atoms. Furthermore, because H has low electron density and relatively high ionization energy, we might also expect a smaller effect from adsorbed H on the ion survival probability. One mechanism by which adsorbed H would cause substantial attenuation of Pt ISS signal is blocking, but only for H atoms bound in atop sites on Pt atoms. The large attenuation from annealing in H_2 thus suggests substantial population of such sites.

XANES. Pt L_3-edge XANES collected at grazing incidence for soft-landed Pt_n/SiO_2/Si (n = 2, 13, 24) are compared to the spectrum for Pt foil in Figure 4. These samples were prepared as above, transported in air, and held under 800 Torr of helium during spectral acquisition. There are two obvious differences between the XANES for Pt_n/SiO_2/Si and Pt foil. The absorption onset or edge, is clearly shifted to higher energy for the Pt cluster samples, and the shift increases with decreasing cluster size. If we estimate the edge energy as the inflection point of the rising edge of the absorption signal, the shifts relative to the energy for Pt foil are ~2 eV for Pt_{24} and Pt_{13}, and ~2.6 eV for Pt_2. In addition, the "white line" peak is both more intense, and shifted to higher energy, than that for

DOI: 10.1021/acs.jpcc.6b10167
J. Phys. Chem. C 2017, 121, 361−374

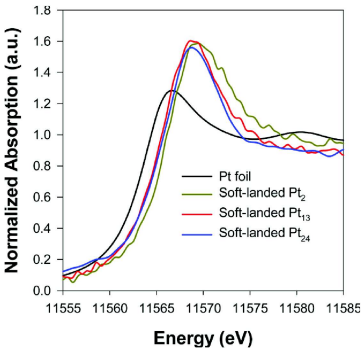

Figure 4. XANES, normalized to the intensity above the edge, for $Pt_n/SiO_2/Si$ samples (n = 2, 13, 24) and Pt foil.

Pt foil, and the shift, but not the intensity, is noticeably larger for Pt_2 than for the larger Pt_n. As noted in the introduction, and discussed below, if these changes were interpreted by reference to XANES for bulk samples, the conclusion would be that the Pt_n are oxidized, presumably during transfer in air to Argonne for XANES analysis. From the ISS measurements above, it is clear that there is oxygen binding to the surface of the clusters. Unfortunately, the beamline used in this experiment is not capable of measuring the full EXAFS energy range, otherwise, EXAFS could potentially give more insights into the nature of the binding.

Figure 5 compares the Pt L_3-edge XANES for soft- and hard-landed $Pt_{24}/SiO_2/Si$ samples, both of which were exposed to air

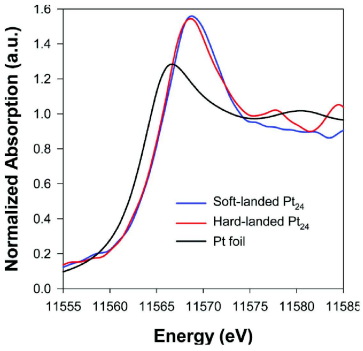

Figure 5. XANES, normalized to the intensity above the edge, for $Pt_n/SiO_2/Si$ samples, prepared by soft and hard landing.

during transportation. XANES was measured under 800 Torr of helium. The differences in the white line intensity and edge energy are negligible, but there is additional structure for the hard-landed sample at higher energies. Unfortunately, the beamline used for this experiment was not optimized for wide-range scans, so we were unable to measure the full EXAFS energy range. Given the GISAXS and ISS results suggesting that the hard-landed clusters are probably embedded into the SiO_2/Si support, we speculate that the additional structure may result from formation of Pt−Si or Pt−O bonds.

A final XANES experiment was done to address two questions: (1) Are the high white line intensities and edge shifts observed for the cluster samples due to oxidation during transport in air? (2) What is the effect of annealing on the XANES structure? A sample was prepared by Pt_{24} soft landing in UHV, as above, then after *in situ* XPS characterization, it was transported and transferred to the XANES cell under N_2. During XANES, the sample was held in a flow of 4% H_2 in helium at a total pressure of 800 Torr. We do not claim that this sample had no air exposure, however, the oxidizer exposure should have been ~10^5 times smaller than for air-transferred samples. Therefore, if silica-supported Pt_{24} does oxidize during air exposure, the extent of oxidation for the N_2-transferred sample *should be less than or equal to* the extent of oxidation for the air-transferred samples. Certainly we would not expect the N_2-transferred sample to be more oxidized. Note that N_2 is unlikely to bind to the clusters in either air or N_2 transfer. Kimmel et al.[56] showed that N_2 desorbs from Pt(111) below 45 K, and Tripa et al.[57] showed that even for stepped and kinked Pt surfaces which present low coordination Pt sites, similar to what might be expected for Pt clusters, N_2 adsorbed weakly, desorbing below 160 K.

Figure 6 shows the XANES for the N_2-transferred sample, both as received at 25 °C, and for various annealing

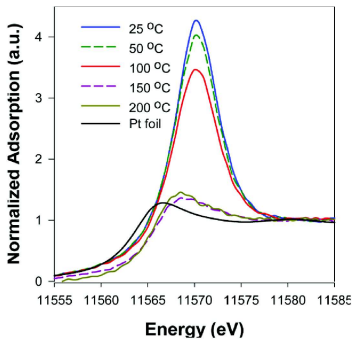

Figure 6. XANES, normalized to the intensity above the edge, for a soft-landed $Pt_{24}/SiO_2/Si$ sample, as a function of annealing temperature in 4% H_2 in He.

temperaures in the H_2/He flow. First consider the room temperature (25 °C) XANES, which should be directly comparable to that for soft-landed Pt_{24} in Figure 4. The white line intensity for this N_2-transferred sample is substantially higher than that for the air-transferred $Pt_{24}/SiO_2/Si$ sample in Figure 4, and its absorption edge energy is shifted 4.4 eV above the edge for Pt foil, compared to a shift of ~2 eV for air-exposed $Pt_{24}/SiO_2/Si$. If we interpreted the edge energy and white line intensity by reference to bulk standards, we would conclude that the N_2-transferred sample is far more oxidized than the sample transferred in air, contrary to intuition.

When the sample in Figure 6 was heated in H_2, there was little change at 50 or 100 °C; however, at 150 °C the white line intensity dropped close to the intensity for Pt foil, although the

DOI: 10.1021/acs.jpcc.6b10167
J. Phys. Chem. C 2017, 121, 361−374

edge and peak energies were still shifted ~2 eV to higher energy, compared to the values for Pt foil. Heating to 200 °C had hardly any further effect on the XANES. Again, if we interpreted these changes by reference to bulk standards, the decrease in white line intensity to the bulk value would suggest that the initially oxidized sample was reduced to the metallic state by heating in H_2 above 100 °C, however, this would not explain why the spectrum remains substantially shifted relative to the bulk Pt spectrum. Note, however, that these XANES changes occurred over the same temperature range where GISAXS showed the clusters sintering into nanoparticles, suggesting that these may be effects of size, rather than oxidation state.

The other difference between the air- and N_2-transferred samples is that the former were studied in He, and the latter in an H_2/He mixture. It has been reported that the white line intensity decreases and the edge broadens and shifts to higher energy as hydrogen is adsorbed on Pt clusters.[58−60] While the edge energy is higher for the N_2-transferred sample studied in H_2, the white line intensity is also higher, and the edge is sharper, compared to the air-transferred sample studied in He. Therefore, we conclude that H_2 cannot explain the differences between the air- and N_2-transferred samples at room temperature. Chemisorbed hydrogen is found to desorb from Pt particles at ~140 °C,[58] which is around the temperature where the white line decrease is observed. It is conceivable that hydrogen may play some role in the decrease, however, the GISAXS results show substantial sintering in this temperature range, and that seems likely to be the dominant effect.

Electronic Structure of Supported Pt_{24} Clusters Probed by XPS. To probe the oxidation state of Pt in these samples, we measured the Pt 4f binding energies (BEs) for Pt_n/SiO_2/Si samples, both as-prepared, and after different treatments. We focus on Pt_2 and Pt_{24}, representing the largest and smallest clusters studied. For Pt_{24}, GISAXS showed that the clusters remained unsintered at temperatures below 150 °C, and for Pt_2, the absence of measurable signal showed that sintering, if it occurred at all at room temperature, did not produce clusters in the GISAXS-detectable size range.

The XPS results are summarized in Figure 7, showing the Pt $4f_{7/2}$ and $4f_{5/2}$ fine structure peaks and fits used to estimate the BEs. All BE values reported and discussed below refer to the $4f_{7/2}$ component.

Spectrum A is for an as-prepared Pt_{24} sample, measured immediately after deposition in UHV. The Pt $4f_{7/2}$ BE is 71.0 eV, at the low end of the 70.9 to 71.3 eV range reported for bulk Pt.[61] The range of reported bulk values is indicated in Figure 7 by a horizontal blue bar at the top of the figure, and the average is indicated by a vertical blue dashed line. The Pt $4f_{7/2}$ BEs reported for PtO are in the 72.4 to 74.6 eV range (average ~74.0 eV), and for PtO_2 the reported BEs are in the 74.1 to 75.6 eV range (average ~74.9 eV). Horizontal bars indicate the reported ranges, and the averages are shown by vertical dashed lines. The 71.0 eV BE for Pt_{24}/SiO_2/Si makes it clear that the Pt is in the zero oxidation state (Pt^0), as might be expected for a sample that was only exposed to UHV.

Spectrum B is for a sample exposed to 1000 L of O_2 after deposition, resulting in a $4f_{7/2}$ BE shifted 0.2 eV to higher energy, to ~71.2 eV. We know from the ISS measurements in Figure 3, that exposure to 1000 L O_2 results in adsorption of oxygen on the Pt cluster surface, and as might be expected, this oxygen ad-layer attenuates the Pt XPS intensity relative to that for the as-prepared sample. It is clear, however, that after O_2 exposure in UHV, the Pt BE remains in the range reported for Pt metal, and far from the ranges reported for PtO or PtO_2.

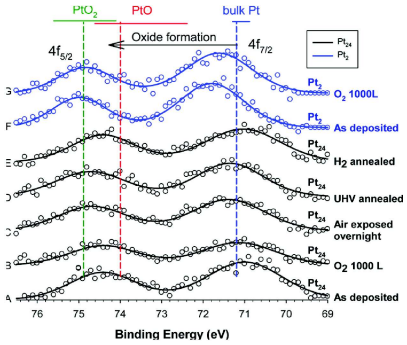

Figure 7. (A−E) Pt 4f XPS for Pt_{24}/SiO_2/Si: (A) as-prepared in UHV; (B) with 1000 L RT O_2 exposure; (C) after overnight air exposure; (D) after annealing to 150 °C in UHV; (E) after annealing at 150 °C in 10^{-4} Torr of H_2; (F and G) Pt 4f XPS for Pt_2/SiO_2/Si, as deposited and after O_2 exposure. Horizontal bars show the range of 4 $f_{7/2}$ BEs reported for bulk Pt and oxides. Vertical lines show mean BE values.

Spectrum C is for a sample that was transferred into the load lock, exposed to ambient laboratory air overnight, and then reintroduced to UHV for postexposure XPS analysis, i.e., for a sample with air exposure comparable to that for the air-transported samples in Figures 1−5. It can be seen that air exposure, which includes O_2, water, and unknown adventitious species, results in a 0.4 eV shift to higher BE and a slight intensity attenuation, compared to the as-prepared sample. Again, however, the BE remains far below the ranges reported for oxides like PtO or PtO_2. It should be noted that the air exposure for this sample was comparable to the exposure for the air-transferred sample set probed in Figures 1,2,4, and 5, and ~10^5 times larger than the estimated exposure for the N_2-transferred sample probed in Figure 6.

Spectrum D is for a sample that was annealed for an hour at 150 °C in UHV, and spectrum E is for a sample that was annealed for an hour in 10^{-4} Torr of H_2. Annealing in UHV results in a ~ 0.4 eV peak shift to higher BE relative to the as-prepared sample, and the Pt XPS intensity is attenuated by 22%. Annealing in H_2 results in a 19% attenuation in Pt XPS intensity, but with no detectable BE shift relative to as-deposited Pt_{24}.

For Pt_2, spectrum F shows that the BE for the as-deposited sample was 71.8 eV—significantly higher than those for any of the Pt_{24} samples. This is outside the BE range reported for bulk Pt^0, but still far from the range expected for Pt oxides. Because this spectrum was measured *in situ*, without significant oxidizer exposure, the shift is attributed to an inherent size effect, as discussed below.

Finally, the Pt_2 sample exposed to 1000 L of O_2 gives rise to spectrum G. O_2 exposure resulted in a small (10%) attenuation of the Pt 4f signal and a shift to *lower* binding energy, by 0.2 eV. Note that the direction of the shift is opposite to what would be expected if the platinum were oxidized by the O_2 exposure.

DOI: 10.1021/acs.jpcc.6b10167
J. Phys. Chem. C 2017, 121, 361−374

DISCUSSION

The key question we wish to address is whether the features seen in XANES of the $Pt_n/SiO_2/Si$ samples are due to Pt oxidation and reduction, as reference to bulk standards would suggest, or if they are due to some size-dependent electronic structure effects, or to some combination of size and oxidation effects. Therefore, we first need to understand how the cluster size and oxidation state vary during the experiments.

GISAXS shows that Pt_{24} is stable after deposition and transport at room temperature for heating up to ~100 °C, but sinters to form particles in the 2−3 nm range during heating to 150 °C or above in H_2. ISS also shows evidence of Pt_{24} sintering during heating to 150 °C in either UHV or H_2, the main difference being that H_2 exposure also results in formation of an adsorbed hydrogen layer.

Pt_2 and Pt_{13} were not detected by GISAXS, which tells us that sintering to clusters in the ≥24 atom range does not occur at room temperature. As discussed below, the substantial shift in XPS BEs between Pt_2 and Pt_{24} is evidence that the clusters present on the $Pt_2/SiO_2/Si$ sample are quite small.

The key question in XANES interpretation is whether or not supported Pt_n clusters oxidize during air exposure. ISS shows that exposure to both O_2 and CO results in binding of an adsorbate layer, but the main information about oxidation state comes from XPS.

XPS BEs are the energy difference between the photoemission initial state (a neutral Pt atom) and final state (Pt missing a core electron), both of which are affected by the atomic environment. For an isolated Pt atom, loss of the core electron results in relaxation of all the other electrons, stabilizing the final state, and reducing the BE relative to what it would be in absence of relaxation. In bulk metal, there is additional final state stabilization by the conduction electrons, which screen/delocalize the charge, further lowering the BE. In a bulk oxide like PtO or PtO_2, the Pt atoms are positively charged, and reduced e^-−e^- repulsion stabilizes the initial state. In addition, the absence of conduction electrons will reduce final state screening and charge delocalization, compared to Pt metal. The combination of more stable initial state, and less stable final state results in Pt 4f BEs that are substantially greater than that for Pt metal: ΔBE = +3 to 3.5 eV for PtO and ΔBE = +4 to 4.5 eV for PtO_2.

For small metal particles on insulating supports, it is common that XPS BEs are higher than those in the bulk metal, even when the particles are clearly in the zero oxidation state.[8,9,13,14,62−74] For example, Au 4f BEs for small unoxidized Au nanoparticles grown on titania or silica increase sharply at low Au coverages (small average particle size), by up to ~1.5 eV for Au/SiO_2.[8] Similarly, XPS BEs for size-selected noble metal clusters deposited on oxide supports are typically 0.5 to 2 eV above the BEs for the bulk metals, generally increasing with decreasing cluster size, but with significant fluctuations with size in some cases.[10,13,38,55,73−77]

For a cluster on an insulating support, the extent of final state charge delocalization clearly shrinks as the cluster does, and band gaps may develop with decreasing size (see below), further reducing the ability to screen and delocalize the charge. Such final state effects tend to increase BEs with decreasing cluster size. Cluster-support interactions can affect the initial state electronic properties in ways that reinforce or counteract this trend. For example, support-to-cluster electron transfer would tend to destabilize the initial state (more e^-−e^- repulsion) and stabilize the final state (better core hole screening), thus lowering the BE, while cluster-to-support electron transfer tends to increase BEs. In addition, recent theoretical studies of Pd atoms on ultrathin SiO_2,[14] and of small Pd_n clusters on TiO_2,[13] have identified rehybridization of metal orbitals as a major factor in BE shifts. Size-specific electronic structure effects, such as electronic shell closings, also affect both the initial and final state energies, causing BE fluctuations with size.

From the above considerations, we might expect that the Pt 4f BE for as-deposited $Pt_2/SiO_2/Si$ should be significantly higher than that for $Pt_{24}/SiO_2/Si$, and that both should be well above the bulk value. In fact, the BE for as-deposited Pt_{24} is slightly (~0.2 eV) *below* the bulk BE, while the Pt_2 BE is 0.6 eV above the bulk value. The fact that the Pt_{24} BE is not shifted to higher energy suggests that there must be some effect that compensates for the expected effect of final state charge localization. We suggest that this effect is support-to-cluster electron transfer, which is not unexpected, given Pt's high work function (6.1 eV for Pt(111)).[78] For example, DFT calculations for Pt_{13} clusters on γ-alumina, by Hu et al.[79] found a net charge on the clusters of up to ~1 e^- depending on binding geometry.

Our XPS results can be compared to experiments by Eberhardt et al.[12] in which Pt_n (n = 1 to 6) were deposited on oxidized silicon wafers and on amorphous carbon films and then studied by XPS. In their experiment, the samples were transferred to the XPS instrument in a portable vacuum system at ~10^{-8} Torr (~150 L exposure to background gases). For $Pt_2/SiO_2/Si$, their Pt 4f BE was 72.65 eV − about 0.8 eV higher than our measurement for as-deposited Pt_2, where the background exposure was ~100 times smaller. It is not clear what is responsible for shift in absolute BE scale, however, their results agree with ours in showing a BE decrease with increasing size. They found a ~0.2 eV decrease from Pt_2 to Pt_6, while we see a 0.8 eV decrease from Pt_2 to Pt_{24}.

When $Pt_{24}/SiO_2/Si$ is annealed to 150 °C or above, GISAXS and ISS show that the clusters sinter into 2−3 nm particles. Since larger particles should allow more screening and charge delocalization in the final state, we might expect the Pt 4f BE to shift lower, closer to the bulk value. As shown in Figure 7, however, the BE for as-deposited Pt_{24} is already below the bulk value, and annealing in H_2 or UHV causes either no shift, or a slight shift to higher BE, respectively. We rationalized the low BE for as-deposited Pt_{24} as resulting from net substrate-to-cluster electron transfer. The amount of electron density that any given area of the SiO_2/Si substrate can transfer to a supported particle is limited. Thus, as clusters sinter into larger particles, the excess electron density *per* Pt atom must decrease, and apparently, this effect slightly overcompensates the shift to lower BE that would be expected from final state charge delocalization. For $Pt_{24}/SiO_2/Si$ annealed in H_2, there was no shift in Pt 4f BE, however, ISS showed the presence of significant hydrogen adsorption on the Pt, which undoubtedly would affect the Pt electronic structure. For example, if there is partial electron transfer from H to Pt, this would tend to offset the reduced substrate-to-Pt electron transfer for larger particles.

From the XANES perspective, the more important point is that when the $Pt_{24}/SiO_2/Si$ sample was exposed to O_2 or to air, the Pt 4f BEs shifted higher by 0.2 and 0.4 eV, respectively. For Pt_2, O_2 exposure actually resulted in a small (~0.18 eV) decrease in the Pt 4f BE. The final BEs remain well outside the range that would be expected for formation of oxides such as PtO or PtO_2.

DOI: 10.1021/acs.jpcc.6b10167
J. Phys. Chem. C 2017, 121, 361−374

Since ISS clearly shows formation of an adsorbed oxygen layer after O_2 exposure, the question is how this oxygen is bound to the clusters. O_2 interaction with Pt(111) has been extensively studied.[80−83] At low temperatures (<120 K), molecular O_2 chemisorbs, but at room temperature, chemisorption is dissociative, with O atoms bound in 3-fold hollow sites at a saturation coverage of 0.25.[82] Each Pt surface atom is coordinated to nine Pt atoms, but at most one O atom, and as a result, there is little effect on the Pt 4f BE. In contrast, in oxides like PtO or PtO_2, each Pt atom is bonded to multiple O atoms, with no Pt nearest neighbors.

For small Pt clusters, the nature of the oxygen adsorption is unclear, because both the Pt electronic properties and available binding sites are quite different from a bulk surface. The small BE shift we observed for Pt_{24} upon oxygen adsorption suggests that, as in bulk Pt, an adsorbed oxygen layer forms, but does not disrupt the network of Pt−Pt bonds in the cluster. This conclusion is consistent with an EXAFS study that showed no oxide formation for small Pt particles in the pores of a zeolite after long air exposure.[84]

The observation that the Pt BE for Pt_2 shifts to *lower* binding energy after O_2 exposure shows that oxygen does bind in some fashion to such small clusters, but with effects that are qualitatively different from those on bulk Pt. This is unsurprising - Pt_2 obviously has no 3-fold sites, and may not support O_2 dissociative adsorption at all. The shift to lower BE may indicate net O_2-to-Pt_2 electron transfer, or may result from increased final state screening from additional electrons brought to the Pt_2-surface complex by oxygen. In summary, it is clear that O_2 exposure to $Pt_n/SiO_2/Si$ leads to oxygen binding, but that nothing resembling a true oxide forms. The small BE shift from air exposure rules out oxide formation in those experiments, as well.

Our conclusion, thus, is that the $Pt_n/SiO_2/Si$ XANES results, including the effects of Pt_n size, annealing, and air vs N_2 transfer, must be interpreted primarily in terms of size-dependent changes in cluster electronic properties, rather than Pt oxidation and reduction. The electronic transitions at the L_3 edge are from the Pt 2p core level to empty states between the Fermi level (E_F) and vacuum level of the sample. The edge energy, therefore, depends on the energy of the lowest unoccupied orbital (LUMO), and the white line intensity depends on both the density of the unoccupied states, as well as the transition probabilities to them from the 2p orbital. For Pt metal, E_F is in the conduction band, thus there are empty states just above E_F, resulting in a low L_3 edge energy. On the other hand, those empty states are mostly in high dispersion s and p bands,[85,86] with low density of states, resulting in a low white line intensity. For oxides such as PtO_2, there is a ∼1.5 eV band gap,[86,87] so that the lowest energy empty states are shifted up in energy with respect to E_F, and the 2p level is stabilized relative to neutral Pt, increasing the edge energy. In addition, there is a peak in the density of states at the bottom of the conduction band, which enhances the white line intensity.

As discusses above, there are also cluster size effects on electronic structure, one of which is development of band gaps between the highest occupied molecular orbital (HOMO) and lowest unoccupied molecular orbital (LUMO), as the cluster size decreases. The HOMO energy has been measured as a function of Pt_n size by two groups, using UPS. Eberhardt et al.[88] measured UP spectra for Pt_n deposited on silica, and Figure 8 shows their measurement of the HOMO energy for $Pt_n/SiO_2/$

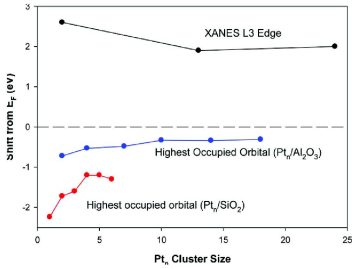

Figure 8. Shifts in the highest occupied orbital energy and the L_3 edge energy, relative to the analogous values for bulk Pt.

Si (n = 1−6), relative to E_F for the sample. More recently, Roberts et al.[11] measured UP spectra for a somewhat wider size range of Pt_n deposited on alumina, and those results for the HOMO energy are also plotted. The difference between the two sets of results may simply reflect the difference in support, however, the Eberhardt experiment was done with samples transferred in a vacuum suitcase at 10^{-8} Torr, whereas the Roberts experiment was done *in situ* in UHV; i.e., there would have been less adventitious exposure to the clusters in the Roberts experiments. Regardless, it can be seen that for small Pt_n, the HOMO is at least ∼0.7 eV below E_F, and even for the largest clusters studied, the HOMO energy is still ∼0.3 eV below E_F, converging slowly with increasing size.

Figure 8 also plots the XANES L_3 edge energies, taken as the inflection points in the absorption onsets in Figure 4. As for the UPS results, the edge energies have been plotted as shifts from the edge energy measured for Pt foil (11564.0 eV). Because the LUMO is at E_F for Pt foil, the edge shifts provide insight into how the LUMO energies vary with size in the Pt_n/SiO_2 samples. Note, however, that because relaxation in the XANES final state may be size-dependent, the edge shift is not equal to the LUMO energy. Nonetheless, it is striking that the increase in L_3 edge energy with decreasing cluster size closely mirrors the drop in the HOMO energies, suggesting that a major cause of the edge shift is simply development of a cluster size-dependent band gap. Although the systems are different, it is interesting to compare Figure 8 with scanning tunneling spectroscopy measurements of the band gaps for small Pd and Au particles on TiO_2, by Lai et al.[89] They observed that as the particle size dropped below ∼2.5 nm, measurable band gaps developed, reaching ∼1.6 eV for Au particles and ∼1.2 eV for Pd particles in the size range of Pt_{24}.

Size effects on the white line intensity are harder to predict, because this depends on both the density of empty states above the band gap, and the transition probability from the Pt 2p orbital into those states. One point is simply that for bulk metal, the empty states are conduction band states with wave functions that are delocalized over the volume of the metal. For small clusters, the extent of wave function delocalization is limited to the dimension of the cluster, thus the overlap between the localized Pt 2p orbital and the empty states should be higher for clusters, increasing with decreasing cluster size. There may also be effects of orbital hybridization that increase the density of empty states. For example, DFT calculations by Reber and Khanna for Pd_n/TiO_2 showed that the 4d−5s hybridization is a function of both cluster size, and the support

DOI: 10.1021/acs.jpcc.6b10167
J. Phys. Chem. C 2017, 121, 361−374

site where the cluster is bound.[13] In addition, Ankudinov et al.[90] reported that the white line intensity is strongly correlated with the geometry of clusters, for free, unsupported Pt clusters. Flatter geometries exhibited higher white line intensity compared to more three-dimensional shapes. They also computed XANES for Pt_6 in a model zeolite, and found, in agreement with experiment, a modest enhancement of the white line intensity. We have no information about our clusters' geometry, however, there is evidence from ion scattering and STM that for Pt_n on both TiO_2[91] and alumina,[11] there is a transition from planar to multilayer geometries at Pt_8.

The effect of cluster−support interactions on XPS are discussed above, i.e., there appears to be initial state SiO_2-to-Pt_n electron transfer that causes the Pt BEs to be shifted lower than would be expected from final state screening and charge localization effects. It is reasonable to expect that initial state electron transfer to Pt_n will also have effects on Pt XANES, although these are harder to predict. For example, support-to-cluster electron transfer will tend to fill otherwise unoccupied states of the clusters, and if all else remained unchanged, this would raise the edge energy, and might lower the density of empty 4d states, hence the white line intensity. Note, however, that it is likely that partial negative charging of the clusters also affects the energies of both the core and valence electrons, making it difficult to predict the effects on XANES. Certainly, the clusters still have band gaps, despite the extra electrons. Detailed calculations on the band structure of the Pt_n/SiO_2 system would be helpful in understanding these effects.

To our knowledge, the above results are the only ones available where XANES has been measured for size-selected clusters, with size confirmed by SAXS and oxidation state probed by XPS both as prepared, and after air and O_2 exposures. There are several other XANES studies of interest for comparison. Wei et al.[21] recently reported an interesting study of single atom and pseudosingle atom Pt catalysts on an iron oxide support, where they varied the Pt loading, thereby varying the average Pt particle size. For particles approaching 2 nm diameter, the XANES was bulk like, but as the cluster size decreased, both the edge energy and white line intensity increased. They attributed this behavior to increasing electron transfer from Pt to the FeO_x support, i.e., to oxidation of the small Pt clusters. As discussed above, however, the work function for Pt (6.1 eV for Pt(111))[78] is so high that significant Pt-to-FeO_x electron transfer seems unlikely. Indeed, our XPS results (Figure 7) for Pt_n/SiO_2 and DFT for Pt_n/alumina[79] both find electron transfer to the clusters. We, therefore, feel that it is likely that Wei et al. also were seeing inherent effects of Pt particle size on XANES.

Bayindir et al.[92] prepared ligand-capped Pt nanoparticles (1−2 nm) and probed their electronic structure with both XPS and XANES. From XPS, the Pt $4f_{7/2}$ BEs for Pt particles with three different capping ligands varied from 0.25 to 0.63 eV above the bulk Pt BE. Pt-ligand binding presumably has some effect on the initial state electronic properties of the Pt, but we also would expect some shift to higher BE from the final state screening/delocalization effect discussed above. In the Pt L_3 edge XANES, they observed an enhanced white line and ∼0.5 eV edge shift, relative to Pt foil, for primary-amine-capped particles. They reported calculations for Pt_{55} model clusters, which showed modest change in the s−p−d hybridization, relative to that in bulk Pt. They also discussed oxidation of the surface of their particles, although the bulk was clearly not oxidized. It is not clear how directly comparable this experiment is to ours, because their particles are ligand capped, whereas ours are bound to SiO_2/Si. Both metal−ligand and metal−support interactions will affect both the initial and final states of XPS and XANES.

CONCLUSIONS

We have shown that for $Pt_n/SiO_2/Si$ (n = 2, 13, 24) samples, XANES shows edge shifts and high white line intensities that would tend to suggest that the Pt is in oxide form, if the spectra were interpreted by reference to bulk standards. ISS and XPS show, however, that although O_2 exposure does result in formation of adsorbed oxygen layer, the Pt remains in the zero oxidation state, i.e., the Pt 4f BEs are far from the range expected for platinum oxides. Thus, we interpret the XANES effects as being primarily due to the inherent effects of cluster size on metal electronic structure. Similarly, the substantial diminution of the white line intensity and edge shift when $Pt_{24}/SiO_2/Si$ is annealed above 100 °C is attributed not to platinum reduction, but rather to sintering of the initial clusters into small nanoparticles, with more bulk-like electronic properties.

These results suggest that when XANES is used to probe samples containing metal particles with sizes below a few nanometers, it is important to consider the effects of particle size on the electronic levels involved in the XANES transition. Simply interpreting the results by reference to spectra for bulk materials can be quite misleading. The ambiguity of assigning XANES features to size vs oxidation effects shows the importance of combining XANES with independent methods that can provide insight into the particle size and oxidation state.

ASSOCIATED CONTENT

Supporting Information

The Supporting Information is available free of charge on the ACS Publications website at DOI: 10.1021/acs.jpcc.6b10167.

XPS, ISS, and XANES data, as well as the drawing of the cluster deposition beamline and surface analysis instrument (PDF)

AUTHOR INFORMATION

Corresponding Author

*(S.L.A.) E-mail: anderson@chem.utah.edu.

ORCID

Scott L. Anderson: 0000-0001-9985-8178

Randall E. Winans: 0000-0002-7080-7673

Notes

The authors declare no competing financial interest.

§Senior Authors

ACKNOWLEDGMENTS

This work supported by the Air Force Office of Scientific Research under a Basic Research Initiative grant (AFOSR FA9550-12-1-0481) and Grant FA9550-16-1-0141. This research used resources of the Advanced Photon Source, a U.S. Department of Energy (DOE) Office of Science User Facility operated for the DOE Office of Science by Argonne National Laboratory under Contract No. DE-AC02-06CH11357.

DOI: 10.1021/acs.jpcc.6b10167
J. Phys. Chem. C 2017, 121, 361−374

REFERENCES

(1) Yoshida, H.; Nonoyama, S.; Yazawa, Y.; Hattori, T. Quantitative Determination of Platinum Oxidation State by XANES Analysis. *Phys. Scr.* **2005**, *2005*, 813.

(2) Rehr, J. J.; Albers, R. C. Theoretical Approaches To X-Ray Absorption Fine Structure. *Rev. Mod. Phys.* **2000**, *72*, 621−654.

(3) Baumgartel, H. EXAFS, SEXAFS, XANES: X-Ray Absorption - Principles, Applications, Techniques of EXAFS, SEXAFS and XANES. *Nachr. Chem., Tech. Lab.* **1988**, *36*, 650−650.

(4) Yano, J.; Yachandra, V. K. X-ray Absorption Spectroscopy. *Photosynth. Res.* **2009**, *102*, 241−254.

(5) Wong, J.; Lytle, F. W.; Messmer, R. P.; Maylotte, D. H. K-edge Absorption Spectra of Selected Vanadium Compounds. *Phys. Rev. B: Condens. Matter Mater. Phys.* **1984**, *30*, 5596−5610.

(6) Shimizu, K.-i.; Kamiya, Y.; Osaki, K.; Yoshida, H.; Satsuma, A. The Average Pd Oxidation State In Pd/SiO_2 Quantified By L3-Edge XANES Analysis And Its Effects on Catalytic Activity for CO Oxidation. *Catal. Sci. Technol.* **2012**, *2*, 767−772.

(7) Bunker, G. *Introduction to XAFS: A Practical Guide to X-Ray Absorption Fine Structure Spectroscopy*; Cambridge University Press: Cambridge, U.K., 2010.

(8) Chusuei, C. C.; Lai, X.; Luo, K.; Goodman, D. W. Modeling Heterogeneous Catalysts: Metal Clusters on Planar Oxide Supports. *Top. Catal.* **2000**, *14*, 71−83.

(9) Bagus, P. S. Chemical Information from XPS Binding Energy Shifts: A Unified View. *Abstracts of Papers, 225th ACS National Meeting, New Orleans, LA, United States, March 23−27, 2003*; 2003, COLL-446.

(10) Kaden, W. E.; Wu, T.; Kunkel, W. A.; Anderson, S. L. Electronic Structure Controls Reactivity of Size-Selected Pd Clusters Adsorbed on TiO_2 Surfaces. *Science* **2009**, *326*, 826−9.

(11) Roberts, F. S.; Kane, M. D.; Baxter, E. T.; Anderson, S. L. Oxygen Activation and CO Oxidation Over Size-Selected Ptn/Alumina/Re(0001) Model Catalysts: Correlations with Valence Electronic Structure, Physical Structure, and Binding Sites. *Phys. Chem. Chem. Phys.* **2014**, *16*, 26443−26457.

(12) Eberhardt, W.; Fayet, P.; Cox, D. M.; Fu, Z.; Kaldor, A.; Sherwood, R.; Sondericker, D. Photoemission from Mass-Selected Monodispersed Platinum Clusters. *Phys. Rev. Lett.* **1990**, *64*, 780−3.

(13) Roberts, F. S.; Anderson, S. L.; Reber, A. C.; Khanna, S. N. Initial and Final State Effects in the Ultraviolet and X-ray Photoelectron Spectroscopy (UPS and XPS) of Size-Selected Pdn Clusters Supported on TiO2(110). *J. Phys. Chem. C* **2015**, *119*, 6033−6046.

(14) Kaden, W. E.; Büchner, C.; Lichtenstein, L.; Stuckenholz, S.; Ringleb, F.; Heyde, M.; Sterrer, M.; Freund, H.-J.; Giordano, L.; Pacchioni, G.; et al. Understanding Surface Core-Level Shifts Using the Auger Parameter; a Study of Pd Atoms Adsorbed on Sio2 Ultra-Thin Films. *Phys. Rev. B: Condens. Matter Mater. Phys.* **2014**, *89*, 115436.

(15) Yang, X.-F.; Wang, A.; Qiao, B.; Li, J.; Liu, J.; Zhang, T. Single-Atom Catalysts: A New Frontier in Heterogeneous Catalysis. *Acc. Chem. Res.* **2013**, *46*, 1740−1748.

(16) Flytzani-Stephanopoulos, M. Gold Atoms Stabilized on Various Supports Catalyze the Water-Gas Shift Reaction. *Acc. Chem. Res.* **2014**, *47*, 783−792.

(17) O'Mullane, A. P. From Single Crystal Surfaces to Single Atoms: Investigating Active Sites in Electrocatalysis. *Nanoscale* **2014**, *6*, 4012−4026.

(18) Thomas, J. M. Catalysis: Tens of Thousands of Atoms Replaced by One. *Nature* **2015**, *525*, 325−326.

(19) Choi, C. H.; Kim, M.; Kwon, H. C.; Cho, S. J.; Yun, S.; Kim, H.-T.; Mayrhofer, K. J. J.; Kim, H.; Choi, M. Tuning Selectivity of Electrochemical Reactions by Atomically Dispersed Platinum Catalyst. *Nat. Commun.* **2016**, *7*, 10922.

(20) Yang, S.; Kim, J.; Tak, Y. J.; Soon, A.; Lee, H. Single-Atom Catalyst of Platinum Supported on Titanium Nitride for Selective Electrochemical Reactions. *Angew. Chem., Int. Ed.* **2016**, *55*, 2058−2062.

(21) Wei, H.; Liu, X.; Wang, A.; Zhang, L.; Qiao, B.; Yang, X.; Huang, Y.; Miao, S.; Liu, J.; Zhang, T. FeOx-Supported Platinum Single-Atom and Pseudo-Single-Atom Catalysts For Chemoselective Hydrogenation of Functionalized Nitroarenes. *Nat. Commun.* **2014**, *5*, 5634.

(22) Lee, S.; Lee, B.; Seifert, S.; Vajda, S.; Winans, R. E. Simultaneous Measurement of X-Ray Small Angle Scattering, Absorption and Reactivity: A Continuous Flow Catalysis Reactor. *Nucl. Instrum. Methods Phys. Res., Sect. A* **2011**, *649*, 200−203.

(23) Lapicki, A.; Boyd, K. J.; Anderson, S. L. Kinematic Sample Mounting System for Accurate Positioning of Transferrable Samples. *J. Vac. Sci. Technol., A* **2000**, *18*, 2603−2605.

(24) Roberts, F. S.; Anderson, S. L. Hollow Cathode Lamp with Integral, High Optical Efficiency Isolation Valve: A Modular Vacuum Ultraviolet Source. *Rev. Sci. Instrum.* **2013**, *84*, 126101.

(25) Kaden, W. E.; Kunkel, W. A.; Roberts, F. S.; Kane, M.; Anderson, S. L. Thermal and Adsorbate Effects on the Activity And Morphology of Size-Selected Pdn/Tio2Model Catalysts. *Surf. Sci.* **2014**, *621*, 40−50.

(26) Wu, T.; Kaden, W. E.; Kunkel, W. A.; Anderson, S. L. Size-Dependent Oxidation of Pd_n ($N \leq 13$) on Alumina/Nial(110): Correlation with Pd Core Level Binding Energies. *Surf. Sci.* **2009**, *603*, 2764−2770.

(27) Kaden, W. E.; Kunkel, W. A.; Roberts, F. S.; Kane, M.; Anderson, S. L. CO Adsorption and Desorption on Size-Selected Pdn/TiO2(110) Model Catalysts: Size Dependence of Binding Sites and Energies, and Support-Mediated Adsorption. *J. Chem. Phys.* **2012**, *136*, 204705.

(28) Cowen, B. J.; El-Genk, M. S. Probability-Based Threshold Displacement Energies for Oxygen and Silicon Atoms in α-Quartz Silica. *Comput. Mater. Sci.* **2016**, *117*, 164−171.

(29) Kane, M. D.; Roberts, F. S.; Anderson, S. L. Alumina Support and Pd_n Cluster Size Effects on Activity Of Pd_n for Catalytic Oxidation of CO. *Faraday Discuss.* **2013**, *162*, 323−340.

(30) Aizawa, M.; Lee, S.; Anderson, S. L. Deposition Dynamics and Chemical Properties of Size-Selected Ir Clusters on TiO2. *Surf. Sci.* **2003**, *542*, 253−275.

(31) Aizawa, M.; Lee, S.; Anderson, S. L. Sintering, Oxidation, and Chemical Properties of Size-Selected Nickel Clusters on TiO2 (110). *J. Chem. Phys.* **2002**, *117*, 5001−5011.

(32) Ilavsky, J.; Jemian, P. R. Irena: Tool Suite for Modeling and Analysis of Small-Angle Scattering. *J. Appl. Crystallogr.* **2009**, *42*, 347−353.

(33) Winans, R. E.; Vajda, S.; Ballentine, G. E.; Elam, J. W.; Lee, B.; Pellin, M. J.; Seifert, S.; Tikhonov, G. Y.; Tomczyk, N. A. Reactivity of Supported Platinum Nanoclusters Studied By In Situ GISAXS: Clusters Stability Under Hydrogen. *Top. Catal.* **2006**, *39*, 145−149.

(34) Winans, R. E.; Vajda, S.; Lee, B.; Riley, S. J.; Seifert, S.; Tikhonov, G. Y.; Tomczyk, N. A. Thermal Stability of Supported Platinum Clusters Studied by in Situ GISAXS. *J. Phys. Chem. B* **2004**, *108*, 18105−18107.

(35) Ravel, B.; Newville, M. ATHENA, ARTEMIS, HEPHAESTUS: Data Analysis For X-Ray Absorption Spectroscopy Using IFEFFIT. *J. Synchrotron Radiat.* **2005**, *12*, 537−541.

(36) Zhai, H.; Alexandrova, A. N. Ensemble-Average Representation of Pt Clusters in Conditions of Catalysis Accessed Through GPU Accelerated Deep Neural Network Fitting Global Optimization. *J. Chem. Theory Comput.* **2016**, *12*, 6213.

(37) Dadras, J.; Shen, L.; Alexandrova, A. Pt−Zn Clusters on Stoichiometric MgO(100) and TiO2(110): Dramatically Different Sintering Behavior. *J. Phys. Chem. C* **2015**, *119*, 6047−6055.

(38) von Weber, A.; Baxter, E. T.; Proch, S.; Kane, M. D.; Rosenfelder, M.; White, H. S.; Anderson, S. L Size-Dependent Electronic Structure Controls Activity for Ethanol Electro-Oxidation at Pt_n/Indium Tin Oxide (n = 1 to 14). *Phys. Chem. Chem. Phys.* **2015**, *17*, 17601−17610.

(39) Yin, F.; Lee, S.; Abdela, A.; Vajda, S.; Palmer, R. E. Communication: Suppression of Sintering of Size-Selected Pd Clusters

DOI: 10.1021/acs.jpcc.6b10167
J. Phys. Chem. C 2017, 121, 361−374

Under Realistic Reaction Conditions For Catalysis. *J. Chem. Phys.* **2011**, *134*, 141101.
(40) Hayakawa, T.; Yasumatsu, H.; Kondow, T. Deposition of Size-Selected Metal Clusters on Inert Graphite Surface with Atomic Anchors. *Eur. Phys. J. D* **2009**, *52*, 95−98.
(41) Smith, R.; Nock, C.; Kenny, S. D.; Belbruno, J. J.; Di Vece, M.; Palomba, S.; Palmer, R. E. Modeling the Pinning of Au and Ni Clusters on Graphite. *Phys. Rev. B: Condens. Matter Mater. Phys.* **2006**, *73*, 125429.
(42) Gibilisco, S.; Di Vece, M.; Palomba, S.; Faraci, G.; Palmer, R. E. Pinning of Size-Selected Pd Nanoclusters on Graphite. *J. Chem. Phys.* **2006**, *125*, 084704.
(43) Tong, X.; Benz, L.; Chretien, S.; Kemper, P.; Kolmakov, A.; Metiu, H.; Bowers, M. T.; Buratto, S. K. Pinning Mass-Selected Agn Clusters on the TiO2(110)-1 × 1 Surface Via Deposition at High Kinetic Energy. *J. Chem. Phys.* **2005**, *123*, 204701−6.
(44) Di Vece, M.; Palomba, S.; Palmer, R. E. Pinning of Size-Selected Gold and Nickel Nanoclusters on Graphite. *Phys. Rev. B: Condens. Matter Mater. Phys.* **2005**, *72*, 073407.
(45) Jodicke, H.; Schaub, R.; Monot, R.; Buttet, J.; Harbich, W. Energetic Cluster Deposition on a Dislocation Network. Ag7 On 2 ML Ag/Pt(1 1 1). *Surf. Sci.* **2001**, *475*, 109−117.
(46) Bromann, K.; Brune, H.; Felix, C.; Harbich, W.; Monot, R.; Buttet, J.; Kern, K. Hard and Soft Landing of Mass Selected Ag Clusters On Pt(111). *Surf. Sci.* **1997**, *377*−*379*, 1051−1055.
(47) Vajda, S.; Winans, R. E.; Elam, J. W.; Lee, B.; Pellin, M. J.; Seifert, S.; Tikhonov, G. Y.; Tomczyk, N. A. Supported Gold Clusters and Cluster-Based Nanomaterials: Characterization, Stability and Growth Studies By In Situ GISAXS Under Vacuum Conditions and in the Presence of Hydrogen. *Top. Catal.* **2006**, *39*, 161−166.
(48) Rabalais, J. W. *Principles and Applications of Ion Scattering Spectrometry: Surface Chemical and Structural Analysis*; Wiley: New York, 2003; p 336.
(49) Kaden, W. E.; Kunkel, W. A.; Anderson, S. L. Cluster Size Effects on Sintering, CO Adsorption, and Implantation in Ir/SiO_2. *J. Chem. Phys.* **2009**, *131*, 114701.
(50) Bertrand, P. G.; Rabalais, J. W. Ion Scattering and Recoiling for Elemental Analysis And Structure Determination. In *Low Energy Ion-Surface Interactions*, Rabalais, J. W., Ed. Wiley: Chichester, U.K., 1994; pp 55−116.
(51) Kumar, R.; Mintz, M. H.; Schultz, J. A.; Rabalais, J. W. Ion Survival Probabilities for 3 Kev Helium(+), Neon(+), and Argon(+) Scattering from Lanthanum and Adsorbate Covered Lanthanum Surfaces. *Surf. Sci.* **1983**, *130*, L311−L316.
(52) Akazawa, H.; Murata, Y. Neutralization of Noble-Gas Ions at Very Low Energies. *Phys. Rev. B: Condens. Matter Mater. Phys.* **1989**, *39*, 3449−52.
(53) Valdes, D.; Goldberg, E. C.; Blanco, J. M.; Monreal, R. C. Linear Combination of Atomic Orbitals Calculation of the Auger Neutralization Rate of He+ On Al(111), (100), and (110) Surfaces. *Phys. Rev. B: Condens. Matter Mater. Phys.* **2005**, *71*, 245417.
(54) Monreal, R. C.; Guillemot, L.; Esaulov, V. A. On Auger Neutralization of He+ Ions on a Ag(111) Surface. *J. Phys.: Condens. Matter* **2003**, *15*, 1165−1171.
(55) Kane, M. D.; Roberts, F. S.; Anderson, S. L. Mass-Selected Supported Cluster Catalysts: Size Effects on CO Oxidation Activity, Electronic Structure, and Thermal Stability of Pd_n/Alumina ($N \leq 30$) Model Catalysts. *Int. J. Mass Spectrom.* **2014**, *370*, 1−15.
(56) Kimmel, G. A.; Stevenson, K. P.; Dohnálek, Z.; Smith, R. S.; Kay, B. D. Control of Amorphous Solid Water Morphology Using Molecular Beams. I. Experimental Results. *J. Chem. Phys.* **2001**, *114*, 5284−5294.
(57) Tripa, C. E.; Zubkov, T. S.; Yates, J. T. J. N_2 Chemisorption on Stepped Pt Surfaces. Control by 2-D and 1-D Precursor Behavior. *J. Phys. Chem. B* **2001**, *105*, 3724−3732.
(58) Vaarkamp, M.; Miller, J. T.; Modica, F. S.; Koningsberger, D. C. On the Relation Between Particle Morphology, Structure of the Metal-Support Interface, and Catalytic Properties of Pt/γ-Al2O3. *J. Catal.* **1996**, *163*, 294−305.
(59) Ramaker, D. E.; Mojet, B. L.; Garriga Oostenbrink, M. T.; Miller, J. T.; Koningsberger, D. C. Contribution of Shape Resonance and Pt-H EXAFS In The Pt L2,3 X-Ray Absorption Edges of Supported Pt Particles: Application and Consequences for Catalyst Characterization. *Phys. Chem. Chem. Phys.* **1999**, *1*, 2293−2302.
(60) Ankudinov, A. L.; Rehr, J. J.; Low, J.; Bare, S. R. Effect of Hydrogen Adsorption on the X-Ray Absorption Spectra of Small Pt Clusters. *Phys. Rev. Lett.* **2001**, *86*, 1642−1645.
(61) Wagner, C. D.; Naumkin, A. V.; Kraut-Vass, A.; Allison, J. W.; Powell, C. J.; Rumble, J. R., Jr., NIST X-ray Photoelectron Spectroscopy Database. *NIST Standard Reference Database 20, Version 3.2 (Web Version)*; 2000.
(62) Wertheim, G. K.; DiCenzo, S. B.; Youngquist, S. E. Unit Charge on Supported Gold Clusters in Photoemission Final State. *Phys. Rev. Lett.* **1983**, *51*, 2310−2313.
(63) Hohlneicher, G.; Pulm, H.; Freund, H.-J. On the Separation of Initial and Final State Effects in Photoelectron Spectroscopy Using an Extension of the Auger-Parameter Concept. *J. Electron Spectrosc. Relat. Phenom.* **1985**, *37*, 209−24.
(64) Wertheim, G. K.; DiCenzo, S. B.; Buchanan, D. N. E. Noble- and Transition-Metal Clusters: The d Bands of Silver and Palladium. *Phys. Rev. B: Condens. Matter Mater. Phys.* **1986**, *33*, 5384−5390.
(65) DiCenzo, S. B.; Berry, S. D.; Hartford, E. H. Photoelectron Spectroscopy of Single-Size Au Clusters Collected on a Substrate. *Phys. Rev. B: Condens. Matter Mater. Phys.* **1988**, *38*, 8465−8468.
(66) Legare, P.; Finck, F.; Roche, R.; Maire, G. Palladium Particles Growth on Various Aluminas. *Z. Phys. D: At., Mol. Clusters* **1989**, *12*, 19−22.
(67) Kuhrt, C.; Harsdorff, M. Photoemission and Electron Microscopy of Small Supported Palladium Clusters. *Surf. Sci.* **1991**, *245*, 173−179.
(68) Bellamy, B.; Mechken, S.; Masson, A. Metallic Clusters Surface Interaction: The Case of Palladium/Silicon Oxide (SiOx)/N-Silicon (100). *Z. Phys. D: At., Mol. Clusters* **1993**, *26*, 61−3.
(69) Bagus, P. S.; Illas, F.; Pacchioni, G.; Parmigiani, F. Mechanisms Responsible for Chemical Shifts of Core-Level Binding Energies and Their Relationship to Chemical Bonding. *J. Electron Spectrosc. Relat. Phenom.* **1999**, *100*, 215−36.
(70) Howard, A.; Clark, D. N. S.; Mitchell, C. E. J.; Egdell, R. G.; Dhanak, V. R. Initial and Final State Effects in Photoemission from Au Nanoclusters on TiO2(110). *Surf. Sci.* **2002**, *518*, 210−224.
(71) Tao, J. G.; Pan, J. S.; Huan, C. H. A.; Zhang, Z.; Chai, J. W.; Wang, S. J. Origin of XPS Binding Energy Shifts In Ni Clusters And Atoms on Rutile TiO2 Surfaces. *Surf. Sci.* **2008**, *602*, 2769−2773.
(72) Kitsudo, Y.; Iwamoto, A.; Matsumoto, H.; Mitsuhara, K.; Nishimura, T.; Takizawa, M.; Akita, T.; Maeda, Y.; Kido, Y. Final State Effect for Au 4f Line from Gold-Nano-Particles Grown on Oxides and HOPG Supports. *Surf. Sci.* **2009**, *603*, 2108−2114.
(73) Mao, B. H.; Chang, R.; Lee, S.; Axnanda, S.; Crumlin, E.; Grass, M. E.; Wang, S. D.; Vajda, S.; Liu, Z. Oxidation and Reduction of Size-Selected Subnanometer Pd Clusters on Al2O3 Surface. *J. Chem. Phys.* **2013**, *138*, 214304−214311.
(74) Peters, S.; Peredkov, S.; Neeb, M.; Eberhardt, W.; Al-Hada, M. Size-Dependent XPS Spectra of Small Supported Au-Clusters. *Surf. Sci.* **2013**, *608*, 129−134.
(75) Lee, S.; Fan, C.; Wu, T.; Anderson, S. L. Cluster Size Effects on CO Oxidation Activity, Adsorbate Affinity, and Temporal Behavior of Model Aun/TiO2 Catalysts. *J. Chem. Phys.* **2005**, *123*, 124710.
(76) Watanabe, Y.; Wu, X.; Hirata, H.; Isomura, N. Size-Dependent Catalytic Activity and Geometries of Size-Selected Pt Clusters on TiO2(110) Surfaces. *Catal. Sci. Technol.* **2011**, *1*, 1490−1495.
(77) Kane, M. D.; Roberts, F. S.; Anderson, S. L. Effects of Alumina Thickness on CO Oxidation Activity Over Pd_{20}/Alumina/Re(0001): Correlated Effects of Alumina Electronic Properties and Pd_{20} Geometry on Activity. *J. Phys. Chem. C* **2015**, *119*, 1359−1375.
(78) Derry, G. N.; Ji-Zhong, Z. Work Function of Pt(111). *Phys. Rev. B: Condens. Matter Mater. Phys.* **1989**, *39*, 1940−1941.
(79) Hu, C. H.; Chizallet, C.; Mager-Maury, C.; Corral-Valero, M.; Sautet, P.; Toulhoat, H.; Raybaud, P. Modulation of Catalyst Particle

DOI: 10.1021/acs.jpcc.6b10167
J. Phys. Chem. C 2017, 121, 361−374

Structure Upon Support Hydroxylation: Ab Initio Insights Into Pd13 And Pt13/γ-Al2O3. *J. Catal.* **2010**, *274*, 99−110.
(80) Gland, J. L.; Sexton, B. A.; Fisher, G. B. Oxygen Interactions with the Pt(111) Surface. *Surf. Sci.* **1980**, *95*, 587−602.
(81) Campbell, C. T.; Ertl, G.; Kuipers, H.; Segner, J. A Molecular Beam Study of the Adsorption and Desorption of Oxygen from A Pt(111) Surface. *Surf. Sci.* **1981**, *107*, 220−236.
(82) Steininger, H.; Lehwald, S.; Ibach, H. Adsorption of Oxygen on Pt(111). *Surf. Sci.* **1982**, *123*, 1−17.
(83) Puglia, C.; Nilsson, A.; Hernnäs, B.; Karis, O.; Bennich, P.; Mårtensson, N. Physisorbed, Chemisorbed and Dissociated O2 On Pt(111) Studied by Different Core Level Spectroscopy Methods. *Surf. Sci.* **1995**, *342*, 119−133.
(84) Deutsch, S. E.; Miller, J. T.; Tomishige, K.; Iwasawa, Y.; Weber, W. A.; Gates, B. C. Supported Ir and Pt Clusters: Reactivity with Oxygen Investigated by Extended X-ray Absorption Fine Structure Spectroscopy. *J. Phys. Chem.* **1996**, *100*, 13408−13415.
(85) Krupski, K.; Moors, M.; Jóźwik, P.; Kobiela, T.; Krupski, A. Structure Determination of Au on Pt(111) Surface: LEED, STM and DFT Study. *Materials* **2015**, *8*, 2935−2952.
(86) Cui, Y.; Harada, Y.; Ikenaga, E.; Li, R.; Nakamura, N.; Hatanaka, T.; Ando, M.; Yoshida, T.; Li, G.-L.; Oshima, M. In Situ Hard X-ray Photoelectron Study of O2 and H2O Adsorption on Pt Nanoparticles. *J. Phys. Chem. C* **2016**, *120*, 10936−10940.
(87) Yang, Y.; Sugino, O.; Ohno, T. Band Gap of β-PtO2 from First Principles. *AIP Adv.* **2012**, *2*, 022172.
(88) Eberhardt, W.; Fayet, P.; Cox, D.; Fu, Z.; Kaldor, A.; Sherwood, R.; Sondericker, D. Core Level Photoemission from Monosize Mass Selected Platinum Clusters Deposited on Silica and Amorphous Carbon. *Phys. Scr.* **1990**, *41*, 892−5.
(89) Lai, X.; St. Clair, T. P.; Valden, M.; Goodman, D. W. Scanning Tunneling Microscopy Studies of Metal Clusters Supported on Tio2 (110): Morphology and Electronic Structure. *Prog. Surf. Sci.* **1998**, *59*, 25−52.
(90) Ankudinov, A. L.; Rehr, J. J.; Low, J. J.; Bare, S. R. Sensitivity of Pt X-Ray Absorption Near Edge Structure to the Morphology of Small Pt Clusters. *J. Chem. Phys.* **2002**, *116*, 1911−1919.
(91) Isomura, N.; Wu, X.; Watanabe, Y. Atomic-Resolution Imaging of Size-Selected Platinum Clusters on TiO2(110) Surfaces. *J. Chem. Phys.* **2009**, *131*, 164707.
(92) Bayindir, Z.; Duchesne, P. N.; Cook, S. C.; MacDonald, M. A.; Zhang, P. X-ray Spectroscopy Studies on the Surface Structural Characteristics and Electronic Properties of Platinum Nanoparticles. *J. Chem. Phys.* **2009**, *131*, 244716.

DOI: 10.1021/acs.jpcc.6b10167
J. Phys. Chem. C 2017, 121, 361−374

CHAPTER 4

SELECTIVE GROWTH OF Al_2O_3 ON SIZE-SELECTED PLATINUM CLUSTERS VIA HIGH VACUUM ATOMIC LAYER DEPOSITION

4.1 Introduction

Catalytic activity, selectivity, and stability are the three main factors that dictate the performance of all catalysts. While controlling all of these aspects is difficult, recent development of atomic layer deposition (ALD) overcoating on nanoparticles has shown great promise to accomplish this goal.[1-4] ALD applies self-limiting reactions and provides precise control over the film growth on the atomic scale. There are two different methods of ALD overcoating, depending on whether the supported NPs are completely covered by an ALD film.[5] When the NPs are completely overcoated (typically over 20 cycles of ALD) initially, the thick film will eliminate the catalytic activities of the NPs and substrate due to the inaccessibility of the reactants to the surface active sites. However, through heat treatment, nano-pores are formed and reexpose the NPs' surface to the reactants.[1,6] The thick ALD layer acts as a physical barrier to prevent sintering or agglomeration, while the selectivity of the catalysts is improved. This is the result of selective blocking of low-coordinated sites by the overcoats, leaving mostly the terrace sites exposed. There is no better example of improved catalytic selectivity and stability than the ALD-overcoated Pd NPs for oxidative dehydrogenation of ethane.[1] With 45 cycles of Al_2O_3 ALD (~7.7 nm thick) on Pd NPs (~2.8 nm) surface, the catalysts give a 23% yield of desired ethylene product in contrast to 1.9% for the uncoated Pd NPs. Meanwhile, the overcoated Pd NPs demonstrate stable catalytic activity for ~1700 min and negligible change of particle size whereas the uncoated Pd NPs completely lose activity due to coke formation and particle sintering.

Another method of ALD overcoating is done by partially coating the supported NPs and the substrate with less than 10 cycles of ALD, leading to a discontinuous film on

the surface.[5] The overcoat preferentially nucleate at the low-coordinated sites (edges and corners) of the NPs.[2,7,8] These low-coordination surface sites are responsible for sintering,[9] and some unwanted side reaction. The advantage of this method is that higher exposure of the NP surface with fewer cycles of ALD, and will therefore have a high catalytic activity as compared to the first overcoating method. For example, Au clusters with 6 cycles of alumina ALD overcoat and Pd clusters with 6 cycles of titania ALD overcoat were both found to exhibit improved sintering resistance during catalytic reactions as compared to the bare clusters without ALD overcoat.[10,11] In addition, it was also found that substrate surface pretreated by ALD overcoating can also prevent sintering of the subnanometer particles under reaction conditions.[12]

Although ALD modification has shown significant improvement in catalytic performance, the mechanism of ALD layer growth on small sized metal clusters is unclear, as is the availability of sites on overcoated clusters under different conditions. The model that explains the preferential nucleation of ALD layer on particularly low-coordination sites on nanoparticles cannot be directly applied to subnanometer clusters, because nearly all the surface atoms are under coordinated. Here, we present a study of alumina ALD on size-selected Pt_{24} clusters using XPS, XANES, TPD, GISAXS, and ISS. In this study, it is demonstrated that the alumina grow effectively on Pt clusters that nearly all CO binding sites were blocked. Upon heating the overcoated Pt clusters, sites at the cluster periphery recovered and became accessible to CO binding.

4.2 Experimental Methodology

4.2.1 Preparation of Supported Size-Selected Pt Clusters

Size-selected Pt_n clusters were deposited on the substrates using a new cluster deposition instrument, which has been described in detail elsewhere.[13] Briefly, the instrument has a UHV section for sample cleaning/annealing, cluster deposition, X-ray and UV photoelectron spectroscopy (XPS, UPS), low-energy ion scattering spectroscopy (ISS), and temperature-programmed desorption (TPD). Clusters are generated and deposited by a beamline that extends into the UHV section. The UHV section has a separate "prep" chamber, equipped with a heatable sample stage that includes a residual gas analyzer, sputter gun, and directional gas inlets. This stage allows ALD to be performed at high vacuum, while avoiding contamination of the UHV section.

A Pt_n^+ beam was generated by laser vaporization of a Pt target in a pulsed helium flow, which then expanded into vacuum. Cationic clusters were collected and guided by a series of radio-frequency quadrupole ion guides through 6 stages of differential pumping, undergoing mass selection by a quadrupole mass filter mid-way along the beam line. The ion guide system extends into one of the UHV chambers, terminating at a 2 mm diameter defining aperture. For deposition, substrates were positioned ~1 mm behind the 2 mm aperture. During deposition, the pressure in the UHV chamber increased by $\sim 2 \times 10^{-10}$ Torr of helium from the source. The deposition energy of the Pt_n clusters was calibrated by retarding potential analysis of the beam on the sample, and most of the samples used in these experiments were prepared with deposition energy of 1 eV/atom, which we will refer to as "soft landing." A few samples were prepared by "hard landing" clusters at 3.75 eV/atom. Deposition of Pt_n clusters was monitored via the Pt_n^+ neutralization current on

the sample, and for all samples, deposition was stopped at a coverage corresponding to 1.50×10^{14} Pt atoms/cm^2, equivalent to 10% of a close-packed Pt monolayer. For X-ray scattering and spectroscopy experiments, samples were prepared by depositing four cluster spots in a row, to better overlap the footprint of the grazing incidence X-ray beam on the sample.

For many experiments, including all experiments where samples were prepared for ex situ studies at the Advanced Photon Source, disposable SiO_2 substrates were used. These were prepared by dicing an oxidized Si (100) wafer into 10 × 14 mm pieces, using n-doped Si to give sufficient conductivity to minimize charging during deposition or X-ray analysis. The SiO_2 substrates were clipped to a tantalum backing plate which was mounted to a copper sample holder by tantalum heating wires spot welded to the back of the plate. A C-type thermocouple was also spot welded to the backing plate for temperature measurement. The SiO_2 substrates were cleaned by heating to 800 K in UHV for 20 min prior to cluster deposition.

For comparison, a few experiments were done using a 7 × 7 mm NiAl(110) single crystal (Surface Preparation Laboratory) to grow a well ordered alumina substrate. A 0.5 nm thick Al_2O_3 film was grown on the NiAl(110) using a procedure[14] adapted from Kulawik et al.,[15] which is reported to give a well-ordered surface structure.[16-21] The NiAl(110) single crystal was initially cleaned by Ar^+ sputtering, followed by annealing at 1250 K for 20 min in UHV. To grow the Al_2O_3 thin film, the NiAl single crystal was exposed to 3000 L of O_2 while being heated to 550 K, followed by annealing at 1100 K for 5 min in UHV. Surface composition was verified by ISS and XPS shows a film thickness of 0.5 nm, in good agreement with previously reported thickness.

4.2.2 High Vacuum Al_2O_3 Atomic Layer Deposition (ALD)

Because we are working with a low coverage of small clusters, and are concerned about the effects of adventitious adsorbates on ALD and other experimental steps, ALD was carried out in the UHV "prep" chamber (base pressure ~8.0×10^{-10} Torr). Samples were transferred into the prep chamber, and then inserted into a heating stage (300k – 1200 K) equipped with gas inlets for ALD, a sputter gun, and a residual gas analyzer (RGA - SRS 200) to monitor gases in the sample region. A gate valve was used to isolate the prep chamber from the rest of the UHV system, except briefly to allow sample transfer. Trimethylaluminum (TMA, Sigma-Aldrich, 97%) and deionized water were used as ALD precursors, and directed at the sample surface through dosing tubes, to minimize exposure to the vacuum system. ALD involves repeated cycling of the two reactions:

$$\mathrm{Al-OH^{*} + Al(CH_3)_3 \rightarrow Al-O-Al(CH_3)_2^{*} + CH_4} \quad (1)$$

$$\mathrm{Al-CH_3^{*} + H_2O \rightarrow Al-OH^{*} + CH_4} \quad (2),$$

where the asterisks denote surface species. Because the gas flows are very small when doing ALD at high vacuum, it is essential to purify the TMA reactant to allow accurate measurement of the sample exposures. For this purpose, a short section of the ~1 mm ID gas line was cooled by mixture of dry ice and ethanol, and then filled with a small amount of gas from the TMA tank headspace, thus freezing the TMA and allowing volatile species like CH_4 to be pumped away. The frozen TMA was then warmed and leaked into the line leading to the sample position. With this procedure, the RGA showed essentially no species other than TMA entering the UHV system. To minimize the exposure of the vacuum system to TMA and water, they were introduced via separate

dosing tubes, pointing at the sample position from a distance of ~0.5 cm. Pressures given below are the background pressures measured with an ionization gauge, but we estimate that the local pressures at the sample surface were ~3 times higher.

We previously showed, using grazing-incidence small angle X-ray scattering (GISAXS) that Pt_n/SiO_2 began to sinter to form larger particle starting at some temperature between 373 and 423 K,[13] thus, we initially attempted ALD with the sample at room temperature, and additional experiments were done at a sample temperature of 423 K. For most experiments, the protocol for 1 cycle of ALD was as follows: water was dosed first with background pressure of 2×10^{-6} Torr for 150 s, followed by 90 s of evacuation. TMA was then dosed at 2×10^{-6} Torr for 150 s, followed by another 90 s of evacuation. One cycle of ALD was completed by a dosing of H_2O at 2×10^{-5} Torr in an attempt to fully react all the TMA adsorbed on the surface. To examine whether the reactant doses were high enough to saturate the surface, we also performed ALD at 423 K with gas doses that were 10 times higher. The dosing process was monitored by the RGA looking at both CH_4^+, from the ALD gaseous product, and mass 57, which is characteristic of unreacted TMA.

4.2.3 In Situ Sample Characterization

XPS, done in situ using Al Kα radiation, was used to verify the cluster coverage, probe the Al_2O_3 ALD growth rate on the SiO_2 substrate, and study the electronic properties of the Pt_{24} clusters with and without ALD overcoating. Pt 4f spectra were taken for as-prepared samples as well as samples with 1 cycle of ALD overcoating. Each of the experiments was done on a separately prepared sample in order to minimize effects

of X-ray damage or adventitious adsorbates.

ISS was done by scattering 1 keV He^+ from the sample, providing insight into the morphology of as-prepared $Pt_{24}/SiO_2/Si$ and how it changes after 1 cycle of ALD overcoating. The He^+ beam was incident at 45° with current of 3 μA (high flux) or 0.1 μA (low flux) on the sample, with a ~7 mm diameter beam spot that is substantially bigger than the 2 mm diameter cluster spot. He^+ scattered along the surface normal was analyzed with a hemispherical energy analyzer. Each sample was probed by a series of ISS measurements to observe how the morphology changes as material is slowly sputtered from the 1 keV He^+ beam. To minimize the effects of He implantation and sputter damage, ISS experiments were done on separately prepared samples.

One of the main questions was whether ALD can selectively poison/block the small Pt clusters. To probe the distribution of accessible Pt sites, CO temperature-programmed desorption (TPD) was used, comparing the absolute amount of CO desorbing from as-prepared $Pt_{24}/SiO_2/Si$ and $Pt_{24}/SiO_2/Si$ with ALD alumina overcoating. Samples were cooled to 180 K and exposed to 10 L of ^{13}CO, which, due to substrate-mediated adsorption,[22,23] is well in excess of the saturation dose. The 180 K dose temperature was chosen to minimize CO adsorption on the SiO_2 support. The sample was then positioned 0.5 mm away from the 3 mm diameter aperture in a skimmer cone, allowing gas desorbing from the sample to pass into a separately pumped chamber housing a quadrupole mass spectrometer. The sample temperature was ramped at 3 K/s, to 600 K. During heating, ^{13}CO, ^{12}CO, CO_2, water, and mass 16 (methane from decomposition of incompletely reacted TMA), were monitored. For each sample, the TPD experiment was carried out three times in succession, such that changes in the

number and energetics of CO binding sites induced by CO exposure and sample heating can be observed.

The $^{13}CO^{+}$ ion signals observed during the TPD experiments were converted to absolute numbers of CO molecules desorbing from the surface, allowing the results to be reported in the form of CO molecules desorbing *per* Pt_{24} cluster. To calibrate the absolute detection efficiency of the TPD system, 2×10^{-8} Torr of CO was leaked into the main chamber via a leak valve, thus producing a well-defined flux of molecules through the aperture in the TPD skimmer cone. The CO pressure was measured with a nude ion gauge, and corrected using the sensitivity factor reported by the manufacturer. The skimmer aperture diameter is 3 mm, whereas the cluster spot diameter is only 2 mm, and this factor was included in the calibration. The calibration was repeated daily, to correct for any day-to-day variations in sensitivity due to changes in electron multiplier gain. There are uncertainties in this calibration method due to the fact that the angular and velocity distributions of molecules entering the skimmer from TPD may be different than the effusive distributions used in calibration, with unknown consequences for detection efficiency. We, therefore, only claim absolute calibration to within ~50 %.

4.2.4 Ex Situ Characterization

Two sets of ALD-modified $Pt_{24}/SiO_2/Si$ samples were prepared for ex situ XANES and GISAXS experiments. For the first set, the samples were transferred out of the UHV system and placed in a custom-made sample container in air, then shipped to Argonne. For this set of samples, ALD was performed in high vacuum with the sample at room temperature, prior to transfer to Argonne. The other set of the samples was

transferred in N_2 to reduce oxygen exposure. A glove bag purged by N_2 was attached to the load lock chamber. The load lock was vented with N_2, the samples were transferred to the sample container under N_2, and then the sample container was put inside a UHV-compatible housing, also filled with N_2. When samples were received in Argonne, they were taken out of the housing and transferred to a sealed cell in an N_2 glove box, then moved to the beamline for X-ray studies. This N_2-transfer approach does not eliminate oxygen exposure, but should have reduced the exposure by a factor of ~10^5, compared to transfer in air. ALD for the N_2-transferred samples was done at a sample temperature of 423 K. All ALD was done using the TMA and water doses described above.

Grazing-Incidence Small-Angle X-ray Scattering (GISAXS) experiments were performed using a unique setup developed at the Sector 12-ID-C at the Advanced Photon Source of the Argonne National Laboratory.[24] The experiments were performed in a homebuilt reaction cell sealed with Kapton windows and mounted on a computer-controlled goniometer. The X-ray beam, tuned to the Pt L3 absorption edge, was scattered off the surface of the sample at grazing incidence, near the critical angle (α_c= 0.15°) of the substrate. A 1024 × 1024 pixel two-dimensional CCD detector designed and built at the APS was used for recording the GISAXS images from the sample. Initial measurements on as-deposited samples were made at incident energy of 18 keV with a scattering vector (q) range of 0.008 – 0.5 $Å^{-1}$ and annealing measurements were done at 11.75 keV with a q range of 0.008 – 0.33 $Å^{-1}$. The scattering vector was calibrated using a silver behenate sample. The size distributions of scatterers present on the sample surfaces were determined by fitting the GISAXS data using the Modeling II tool in the Irena package.[25]

Grazing incidence X-ray absorption spectra were collected at the Sector 12BM-B and 12-ID-C stations at the Advanced Photon Source of the Argonne National Laboratory using fluorescence detectors (13 element Ge detector and Vortex 4 element SDD) mounted perpendicular to the X-ray beam and parallel to the sample surface. The measurements focused on the X-ray absorption near edge spectral region (XANES), and were analyzed using the IFEFFIT interactive software package (with ATHENA and ARTEMIS graphical interfaces).[26]

4.3 Results

4.3.1 Characterization of Al_2O_3 Growth Rate by High Vacuum ALD

The growth rate of Al_2O_3 deposited on the clean planar SiO_2/Si substrate in the UHV prep chamber was characterized by XPS. Results for growth at a surface temperature of 423 K and for reactant doses as described above are shown in Figure 4.1. As shown in Figure 4.1(a), the Al 2p BE of the film was 75.3 eV, in the range of reported values for oxidized Al, and the peak intensity increased with number of ALD cycles. The ratio of the integrated intensities for the Al 2p and Si 2p peaks (shown in Figure A.1), was modeled to estimate the thickness of the Al_2O_3 film as a function of ALD cycle number. A layered model was constructed, using reported values of photoemission cross sections and asymmetry parameters from Yeh and Lindau,[27] and effective attenuation lengths (EAL) calculated from the NIST EAL Database version 1.3.[28] The average growth rate over 12 cycles was ~0.4 Å per cycle, however, the growth rate was observed to accelerate significantly, from ~0.2 Å/cycle averaged over the first three cycles, to ~0.67 Å/cycle for the last three cycles.

These growth rates are slow compared to what has been observed in alumina ALD at higher pressures. Ott et al.[29] used ellipsometry to characterize the ALD growth rate of alumina while also using oxidized Si(100) as the substrate. They examined substrate temperatures ranging from 350 to 650 K, with reactants dosed at ~20 mTorr in a vacuum system with ~10^{-5} Torr base pressure. For 250 ALD cycles, the fastest growth rate was observed at 450 K (~1.1 Å/cycle), with thickness found to be quite linear with the number of ALD cycles. The growth rate was only weakly dependent on temperature between 350 and 500 K. For example, at 400 K, the rate was ~1 Å/cycle. Analogous behavior was observed by Elam et al. in a viscous flow reactor.[30]

One obvious possibility is that our reactant doses were simply too small to saturate the available growth sites, and to test this hypothesis, we also measured the growth rate for reactant doses that were 25 times higher than in Figure 4.1. Both TMA and water were dosed at ~5×10^{-5} Torr background pressure for 150 s, but the difference in growth rate between the high dose (shown in Figure A.2) and low dose was found to be negligible, that is, the gas dose was not the limiting factor, even for the lower dose.

The alumina growth rate was measured for ALD performed at room temperature, using the lower of the two doses of TMA and water (2×10^{-6} Torr for 150 s). As shown in Figure A.3, the average growth rate was 0.92 Å/cycle, in other words, about twice as large as for the same reactant dose at 423 K. This result is somewhat surprising, however, as discussed below, there is evidence that it reflects incomplete reaction during growth, resulting in substantial incorporation of organic fragments into the surface layer. This conclusion is consistent with Ott et al. [29] who used IR spectroscopy to look at CH and OH

stretch vibrations associated with organics and hydroxyls incorporated in alumina films grown by ALD, and observed increasing intensity with decreasing growth temperature.

There are several differences between our experiment and that of Ott et al. which presumably explain our ~5 times lower initial growth rate. As noted, the gas dose used is not a limiting factor. Our growth temperature (423 K) is also slightly lower than the optimum temperature found by Ott et al. (450 K), but based on their measured temperature dependence, we would expect the small difference in temperature to result in only a few percent change in grown rate. Instead, the difference is attributed to the density of reactive sites present on the surface in the two experiments. In the Ott et al. work, the oxidized Si sample was pretreated with a H_2O plasma prior to ALD for sample cleaning, presumably leading to a high density of hydroxyls on the surface, serving as ALD growth sites. In our experiment, the oxidized Si substrate was heated to 800 K in UHV for 20 min for sample cleaning, which should desorb most hydroxyls present. The slow growth rate observed indicates that the H_2O dose that was the first step in our ALD protocol must have created only a small density of hydroxylated sites, presumably at defects in the silica surface. This conclusion is supported by consideration of the growth rates in terms of fraction of an alumina monolayer *per* ALD cycle. Ott et al. used the index of refraction of alumina films grown by ALD to estimate the thickness of one monolayer as 3.64 Å, that is, even their best growth rate at 450 K was less than one third of a complete alumina monolayer *per* cycle. Our initial growth rate of 0.2 Å/cycle corresponds to ~5 % of a monolayer, which is a plausible value for the density of defect sites capable of reacting with water to initiate ALD at 423 K. The rate increased during subsequent cycles, but remained below 1.1 ML/cycle for the relatively small number of

cycles studied. The increase in rate suggests that alumina islands initially nucleating on about ~5 % of the surface, spread laterally as they grow, allowing ALD to proceed on a larger fraction of the surface.

From the perspective of understanding the interaction of ALD reagents with the deposited Pt_n clusters, the low reactivity of the SiO_2 substrate is advantageous, allowing us to observe how the presence of clusters affects the area-averaged growth rate. In fact, the growth rate when 0.1 ML of Pt_n is present is substantially higher, as shown in Figure 4.2. This compares XPS signals in the region of the Al 2p and Pt 4f peaks for samples with and without Pt_{24} and alumina ALD. For Pt-free SiO_2, only a small Al 2p peak is observed even after 3 ALD cycles, as discussed previously. For as-deposited $Pt_{24}/SiO_2/Si$, signal is seen for the Pt $4f_{7/2}$ and $4f_{5/2}$ peaks at ~71 and ~74.4 eV, respectively. A single ALD cycle on this sample has little effect on the Pt $4f_{7/2}$ peak, but results in a large peak at ~75 eV due to overlapping contributions from Al 2p and Pt $4f_{5/2}$. Because the Pt $4f_{7/2}$ and $4f_{5/2}$ peaks are in a fixed, 4:3 intensity ratio, it is straightforward to separate the Al 2p and Pt $4f_{5/2}$ contributions, as shown by the fits. The extracted Al 2p intensity following a single ALD cycle on $Pt_{24}/SiO_2/Si$ is ~2.2 times greater than the Al 2p intensity following three cycles on SiO_2/Si, that is, the initial alumina growth rate is more than six times higher when Pt_{24} present, even though the Pt coverage is equivalent to only 0.1 Pt monolayers. Clearly, the Pt_{24} clusters act as efficient ALD initiation sites.

4.3.2 Particle Size Characterization by GISAXS

Because samples were characterized ex situ by GISAXS and XANES, it is necessary to examine whether the clusters remain intact after deposition and transfer to

the APS, and to also assess the degree of thermal sintering that might occur when the samples were heated to 423 K as part of the ALD protocol. We previously reported[13] a study in which $Pt_n/SiO_2/Si$ (n = 2, 13, 24), were both soft- and hard-landed on SiO_2/Si in UHV and then transferred to the APS for characterization by GISAXS and XANES at different temperatures. For soft-landed Pt_{24}, the scattered size distribution extracted from the GISAXS data was narrow and peaked at 0.96 nm – about what would be expected for flattened 24 atom Pt islands on a surface (spherical Pt_{24} would be ~0.9 nm). We were unable to observe scattering from Pt_{13} or Pt_2, which shows that if these do agglomerate, they at least do not produce large enough clusters to result in detectable scattering signal. When the Pt_{24} sample was annealed in 50 K steps, significant growth in the scatterer size distribution was first observed between 373 K and 423 K.

GISAXS was used to look at $Pt_{24}/SiO_2/Si$ samples after different ALD treatments. Figure 4.3a compares the raw room temperature GISAXS data for SiO_2/Si with no clusters deposited ("SiO_2 blank"), with those for soft-landed $Pt_{24}/SiO_2/Si$, and for soft-landed $Pt_{24}/SiO_2/Si$ with 1 cycle of room temperature alumina ALD carried out after cluster deposition, that is, "overcoating." Compared to the SiO_2/Si blank, Pt_{24} deposition results in additional scattering in the q range between 0.02 and 0.4 $Å^{-1}$, and ALD overcoating results in a large increase in scattering signal over the entire q range studied. The scatterer size distributions extracted by fitting the differences relative to SiO_2/Si are shown in Figure 4.3b. For $Pt_{24}/SiO_2/Si$ without ALD, the distribution is narrow and peaks at 0.96 nm, as noted above. For ALD-overcoated soft-landed $Pt_{24}/SiO_2/Si$, the scatterer size distribution is drastically broadened, spanning the range from 0.8 nm to 2.2 nm, and peaking at ~1.48 nm. Wang et al.[7] previously reported that applying 50 cycles of TiO_2

ALD overcoat on Au particles (2.9 ± 0.45 nm) did not lead to major changes in the size of the Au particle cores observed by HRTEM. As will be shown in the following paragraphs, our evidence suggests that ALD at such low temperatures leads to efficient TMA adsorption on the Pt clusters. During transfer to the APS in air, this TMA (or fragments thereof), would tend to react with air, apparently resulting in a substantial increase in the disorder associated with Pt.

The effects of ALD performed at 423 K, and of annealing the samples to different temperatures, were also monitored by GISAXS. Raw data for four different annealing temperatures are shown in Figure 4.4, and the corresponding scatterer diameter distributions for the two higher temperatures are shown in Figure 4.5.

The following samples are compared in Figure 4.4: $Pt_{24}/SiO_2/Si$ with no ALD treatment, $Pt_{24}/SiO_2/Si$ with 3 cycles of ALD *prior* to Pt_{24} deposition (denoted as $Pt_{24}/3ALD/SiO_2/Si$), $Pt_{24}/SiO_2/Si$ with 3 cycles of ALD *prior* to Pt_{24} deposition and 1 cycle of ALD *after* Pt_{24} deposition (denoted as $1ALD/Pt_{24}/3ALD/SiO_2/Si$), and $Pt_{24}/SiO_2/Si$ with 6 cycles of ALD *prior* to Pt_{24} deposition (denoted as $Pt_{24}/6ALD/SiO_2/Si$). The Pt_{24} clusters were soft-landed in all cases. To minimize air exposure during sample transfer to Argonne, these samples were transferred under N_2. Samples were annealed to different temperatures in a flow of 4% H_2 in helium at 800 Torr total pressure. For these experiments, GISAXS was measured for somewhat smaller q values ($q_{max} \leq 0.35$ Å^{-1}) than in the room temperature experiment (Figure 4.3),[31] roughly doubling the maximum detectable scatterer diameter.

As shown in Figure 4.4, there was little change in scattering for any sample at annealing temperatures up to 373 K. In particular, the signal at high q (> 0.1 Å^{-1}) for the

$Pt_{24}/SiO_2/Si$ sample is relatively flat, with little growth at temperatures up to 373 K. This observation indicates, as discussed above, that most of the Pt remained in subnano cluster form at 373 K and below. The growth in high q signal at higher temperatures indicates the onset of sintering to form small nanoparticles.

Samples where Pt_{24} deposition was done after the SiO_2/Si substrate was exposed to 3 or 6 ALD cycles (Figure 4.4(b), (d)) were not heated after cluster deposition prior to the annealing experiment shown in the figure. Recall that ALD initiation on the SiO_2/Si support is inefficient, with an initial growth rate equivalent to ~5% of a monolayer/cycle. Therefore, 3 and 6 cycles of ALD would deposit partial alumina layers. There is no reason to expect that the presence of a partial alumina layer should enhance Pt sintering, instead, we might expect sintering to be inhibited on the more corrugated, diffusion-limiting surface. Nonetheless, there is additional scattering in the high q range even at low annealing temperatures, which we therefore attribute to disorder associated with the roughness of this partial alumina layer itself.

For the $1ALD/Pt_{24}/3ALD/SiO_2/Si$, where one 423 K ALD cycle was carried out after Pt_{24} deposition, there is additional signal in the high q range, presumably reflecting that alumina deposition is more efficient on Pt_{24} clusters than on the SiO_2/Si support (Figure 4.4(c)). It is, therefore, interesting to compare the high q scattering for this sample, against that for the sample exposed to 1 cycle of room temperature ALD after Pt_{24} deposition. Clearly the high q scattering is weaker following 423 K ALD overcoating (Figure 4.4(c)) than after room temperature overcoating (Figure 4.3(a)).

Figure 4.5 compares the scatterer size distributions extracted from the data in Figure 4.4, for annealing temperatures of 423 K (i.e., the temperature at which ALD was

done) and 473 K. For the $Pt_{24}/Si/SiO_2/Si$ sample without ALD (or prior heating) the scatterer size distribution shifted to larger diameter and broadened, compared to the unheated distribution in Figure 4.3(b), peaking at ~1.1 nm at 423 K, and ~2.1 nm at 473 K. For reference, a 2.1 nm hemisphere would contain ~160 Pt atoms at the bulk density.

For the samples with ALD, interpretation of the scatterer size distributions and their temperature dependence is ambiguous, because annealing may cause changes both to the clusters and the partial alumina layer.[12,32] The scatterer size for the $Pt_{24}/6ALD/SiO_2/Si$ sample at 423 K is similar to that for the $Pt_{24}/SiO_2/Si$ sample at the same temperature, and the peak shifts to 2.6 nm at 473 K. The increase in scatterer size suggests that the partial alumina layer resulting from 6 cycles of ALD undercoating did not significantly increase resistance to Pt thermal sintering. For the $Pt_{24}/3ALD/SiO_2/Si$ sample, the fitted scatterer distribution shifted slightly to smaller diameter between 423 and 473 K. For the ALD overcoated sample, $1ALD/Pt_{24}/3ALD/SiO_2/Si$, the initial scatterer size was significantly larger than for any of the other samples, presumably reflecting efficient alumina grown on and around the Pt_{24} clusters. Note, however, that this sample was the only one where the size distribution did not change significantly after annealing to 473 K, which may indicate that the alumina overcoat provides some protection against Pt thermal sintering. It is also possible, however, that the lack of change simply reflects offsetting thermal changes to the Pt and alumina constituents, such that the net scatterer diameter is unaffected.

4.3.3 Temperature-Programmed Desorption (TPD)

TPD experiments were performed to probe several related issues: the density of accessible Pt binding sites on the samples, the presence of pyrolyzable organic material in the ALD alumina layer, and the sticking/desorption temperature dependence on both SiO_2 and Pt_{24}. CO was chosen as the probe molecule because it binds strongly to small Pt clusters, but not to oxide supports,[33] and thus provides insight into the effects of ALD overcoating on the number and energetics of Pt-associated binding sites. A series of sequential ^{13}CO TPD runs were made on samples in order to observe how the CO binding properties changed with heating. Before each TPD run, the samples were exposed to 10 L of ^{13}CO at 180 K, and then heated at 3 K/s while monitoring species desorbing from the surface. The 180 K exposure temperature was chosen to minimize CO binding on the SiO_2 support, while still saturating most sites associated with Pt_n.[33]

4.3.3.1 CO Desorption as a Probe of Pt Binding Sites

As shown in Figure 4.6a, for Pt_{24} on SiO_2/Si without ALD overcoating, there are two CO desorption features, peaking at ~190 K and ~510 K, These are similar to CO desorption observed from Pt_n ($1 \leq n \leq 18$) deposited on a ~3 nm thick alumina film grown by evaporation onto Re(0001).[33] In the second TPD run, the high-temperature feature decreased, and more desorption was observed at low temperatures. Essentially, no further change was observed in a third TPD run. For the Pt-free SiO_2/Si sample, no ^{13}CO desorption was observed in the temperature range probed, indicating that CO does not bind to SiO_2/Si at 180 K.

Figure 4.6b shows ^{13}CO TPD data taken under identical conditions, for a $Pt_{24}/SiO_2/Si$ sample that was exposed to 1 cycle of ALD alumina overcoating after Pt_{24} deposition, before TPD. The overcoating was done at a sample temperature of 423 K, and with reactant exposures of 2 x 10^{-6} Torr for 150 s. Note that in the first TPD run, both the low- and high-temperature CO desorption features were almost completely suppressed, indicating that CO found essentially no binding sites that were stable at the 180 K exposure temperature. In the second TPD run, a low-temperature CO desorption feature is observed, with somewhat sharper temperature dependence than the low-temperature feature observed for as-deposited $Pt_{24}/SiO_2/Si$, but the high-temperature feature remains suppressed in the second TPD. No further evolution was observed in the third TPD. For Pt-free SiO_2/Si with 1 cycle of alumina ALD, no significant ^{13}CO desorption was observed. Given that essentially no CO TPD was observed from SiO_2/Si without the ALD overcoat, we can conclude that ALD did not create any additional CO binding sites.

These results demonstrate that a single cycle of 423 K ALD alumina overcoating completely blocks all CO binding sites associated with Pt_{24}. After the first TPD run, low-temperature CO binding sites are again available, however, the higher temperature binding sites remain blocked even after several heating ramps. Recent works[7,34] show that CO binding sites associated with Au nanoparticles can be blocked by a TiO_2 ALD overcoat. DRIFTS CO chemisorption measurements showed that TiO_2 preferentially nucleates at low-coordination sites on the Au nanoparticles and after 50 cycles of TiO_2 ALD, the peak intensity for adsorbed CO dropped by ~3 orders of magnitude. In our case, even a single cycle of ALD is sufficient to block essentially all CO binding sites on our small Pt clusters, and after heating, only weak binding sites are exposed, with

desorption temperatures below 200K.

4.3.3.2 Desorption of Organics From the ALD Alumina Layer

Both the thermal changes to the GISAXS for ALD-coated samples, and the partial recovery of CO binding sites on Pt after 600 K heating, suggest that the alumina layer undergoes significant structural changes, and one obvious possibility is loss of organic species incorporated during low-temperature ALD. Figure 4.7 shows the mass 16 TPD signal recorded during the first CO TPD run on SiO_2/Si and Pt_{24}/SiO_2/Si samples overcoated with one alumina ALD cycle. Mass 16 is a major peak in the EI mass spectra for both TMA, and methane, that is, the organic product of the ALD chemistry. For Pt_{24}/SiO_2/Si, both 300 K and 423 K ALD overcoating was examined. After 300 K ALD on Pt_{24}/SiO_2/Si, there is substantial mass 16 signal starting at 300 K, and peaking ~380 K. For 423 K ALD on Pt_{24}/SiO_2/Si, there is considerably less signal, starting around 400 K, and peaking near 500 K. For the SiO_2/Si substrate, there is no significant mass 16 signal following a 423 K ALD cycle. As shown in Figure A.4 for the 423 K ALD-overcoated Pt_{24}/SiO_2/Si sample, no significant mass 16 desorption was observed in the second or third CO TPD. Clearly most of the pyrolyzable organic content in the alumina layer is lost during the first TPD run. Similar results were observed for mass 16 desorption from ALD-overcoated Pt_{24}/alumina/NiAl(110), as shown in Figure A.5.

Gow et al.[35] previously reported TPD of TMA desorbing from clean Si(100). They identified two contributions to the mass 16 signal, including mass spectrometer cracking of TMA, or fragments thereof, desorbing in the 300 K - 600 K range, and ionization of methane desorbing in the 400 K - 800 K range. Thus, Figure 4.7 indicates

that room-temperature ALD leaves a substantial amount of residual organic content in the alumina, which is reduced, but not eliminated, by raising the ALD temperature to 423 K. The choice of 423 K for ALD in the main set of experiments was driven by the conflicting desire to have as little organic contamination of the alumina as possible, while also minimizing thermal sintering of the Pt_{24}. As noted, 423 K is close to the 450 K optimum Al_2O_3 ALD growth temperature reported by Ott et al.[29]

4.3.3.3 Desorption of H_2O From the Alumina ALD Overcoated Samples

The first step in our ALD process was dosing H_2O, therefore, an interesting question is whether alumina growth initiates so efficiently on the Pt_{24} cluster because water binds efficiently to the clusters at the 423 K ALD dose temperature. Figure 4.8 shows the mass 18 (H_2O) TPD signal recorded during the first CO TPD run on three samples. For as-deposited $Pt_{24}/SiO_2/Si$ exposed only to water at 423 K, only a small amount of water desorption was observed, mostly well below the 423 K ALD dose temperature. This small signal presumably reflects residual water from the 423 K water dose adsorbing as the sample was cooled to the 180 K CO dose temperature. For a $Pt_{24}/SiO_2/Si$ sample exposed to one 423 K ALD cycle (i.e., water, then TMA, then water again), a large amount of water desorbed at high temperatures. Finally, for SiO_2/Si without Pt_{24}, exposed to one 423 K ALD cycle, only a small amount of water desorbed around 200 K, again, attributed to adsorption of residual water from the final water dose as the sample was cooled.

The three results, together with results presented above showing that ALD initiates efficiently on $Pt_{24}/SiO_2/Si$, but not on SiO_2/Si, leads to the conclusion that water

does not adsorb stably on Pt_{24} clusters at 423 K. Therefore, we conclude that the efficient initiation of alumina growth on Pt_{24} is due to efficient binding of TMA on the clusters. The large amount of high-temperature water desorption on the ALD-overcoated $Pt_{24}/SiO_2/Si$ sample is, thus, due to water (or OH) adsorbed on the alumina layer deposited on Pt_{24}.

4.3.4 Electronic Structure of Overcoated Pt_{24} Clusters

Both the ALD growth rate (Figure 4.2) and TPD results clearly show that alumina ALD preferentially nucleates on Pt cluster sites, thus preventing CO adsorption. One question is whether the latter effect is simply due to physical site blocking, or if binding of the ALD layer on Pt_{24} changes the electronic structure of Pt, and ultimately, the CO affinity for Pt.

4.3.4.1 XPS

The XPS measurements made during the course of the ALD experiments provide insight into this question. Figure 4.2 compares the Pt 4f XP spectra measured for $Pt_{24}/SiO_2/Si$, as-deposited in UHV, and after 1 cycle of 423 K ALD overcoating. For the as-deposited sample, the Pt $4f_{7/2}$ binding energy (BE) is 71.0 eV, which is in the range reported for the Pt $4f_{7/2}$ BE for bulk Pt (70.9 eV to 71.3 eV, mean 71.2 eV[36]). As discussed elsewhere,[37-39] core level binding energies for small supported clusters tend to be higher than those for bulk metals, because there is less screening and charge delocalization in the photoemission final state in small clusters. In this case, the bulk-like BE for Pt_{24} leads to the conclusion that there is partial electron transfer from SiO_2/Si to

Pt_{24}, offsetting the expected shift to higher BE from final state screening.[13]

In the XP spectrum taken after 1 cycle of Al_2O_3 ALD overcoating, the Pt $4f_{7/2}$ peak is fit with a BE of 71.1 eV, while the higher energy feature has contributions from both the Pt $4f_{5/2}$ component at 74.4 eV (same 7/2 – 5/2 splitting as in the bottom spectrum), and an Al 2p feature which is fit to obtain a BE of 75.0 eV. The 0.1 eV BE shift seen for Pt $4f_{7/2}$ suggests that the electronic environment of the Pt cluster is not significantly changed by ALD overcoating, and therefore the suppression of CO binding by ALD overcoating is due to physical blocking of the Pt surface. The change in Pt $4f_{7/2}$ XPS intensity after ALD overcoating is small (~2%), consistent with the amount of material deposited on top of the Pt being small. For the kinetic energy of the Pt 4f photoelectrons (96.5 eV), we can estimate the electron effective attenuation length (EAL) using the NIST Effective Attenuation Database.[28] For a complete alumina monolayer, we would expect attenuation of ~7.0%, suggesting that the actual coverage on Pt_{24} is only equivalent to ~1/3 ML.

The fitted binding energy for Al 2p in the overcoated sample is ~75 eV, which is at the high end of the range of BEs reported for bulk Al_2O_3 or aluminum hydroxides, and at the low end of BEs reported for alumina films on aluminum.[36] Furthermore, there is also a report that the Al 2p BE for TMA on silver is 75.0 eV, thus, we really are only able to say that the aluminum is in some oxidized state, possibly including partially decomposed/oxidized TMA.

4.3.4.2 Grazing-Incidence X-ray Absorption Near Edge Spectra

Normalized Pt L_3-edge XANES spectra are shown in Figure A.6 for all the samples. As with the GISAXS experiments (Figure 4.4), samples were studied as-received at the APS, and during annealing to different temperatures in a H_2/He flow. The results at room temperature and 473 K are collected together in Figure 4.9, and the edge energies, taken as the inflection point, for the all the samples shown in the figure have been summarized in Table 4.1. At 298 K, the edge for all samples is shifted 5 eV to higher energy with respect to the Pt foil reference, regardless of whether the sample had ALD treatment or not. The $Pt_{24}/SiO_2/Si$ sample without ALD has higher white line intensity compared to both the Pt foil reference sample and the ALD-treated samples. High edge energy and white line intensity are often taken as evidence of oxidation, however, in a previous study of XANES for Pt_2, Pt_{13}, and Pt_{24} on SiO_2/Si, we used XPS to show that deposited Pt_n remain in the zero-oxidation state, both as-deposited, and after large O_2 or air exposures.[13] As discussed above, and shown in Figure 4.2, ALD causes a negligible change in the Pt 4f BE, that is, the Pt in the ALD-treated samples is also in the zero-oxidation state. Instead, the edge shifts are attributed to size-dependent changes in both core and valence level binding energies, which destabilize the XANES final state. The origin of the high white line intensity is less obvious, but it is not unexpected that there might be rehybridization that changes the empty state density,[40,41] as well as better overlap between the core orbital and localized empty orbitals in small clusters, compared to the delocalized conduction band states available in bulk metal.[13]

At room temperature, the ALD-treated samples have substantially lower white line intensity. The white line intensity decreases in the order of $Pt_{24}/SiO_2 \gg$

Pt_{24}/6ALD/SiO_2/Si > Pt_{24}/3ALD/SiO_2/Si > 1ALD/Pt_{24}/3ALD/SiO_2/Si. Since XPS shows that the Pt oxidation state does not change significant for the ALD-treated samples, we propose that the changes in white line and edge energies reflect more subtle interactions of the Pt_{24} orbitals with those of the Al_2O_3 ALD layer(s). For example, if the empty state wave functions of the Pt_{24} clusters delocalize in response to interaction with the defected alumina layer(s), or if there is alumina-to-cluster electron transfer, this would tend to reduce the white line signal.

After annealing in H_2 at 473 K, the white line intensity dropped significantly for all the samples. Such changes are often attributed to reduction of initially oxidized metal centers, however, the Pt in these samples was not oxidized. Furthermore, if reduction were responsible for the white line decrease, a significant reduction in the edge energy should also occur, which is not observed. For the Pt_{24}/SiO_2/Si sample, GISAXS shows that substantial cluster sintering occurs in the temperature range, thus, the annealing effect on the XANES was attributed to size-dependent electronic structure effects. At 473 K, the ALD-overcoated 1ALD/Pt_{24}/3ALD/SiO_2/Si sample, which had the lowest intensity at room temperature, has the highest intensity and edge energy of any of the ALD-treated samples, that is, was least affected by annealing in H_2. This could reflect less cluster sintering in the overcoated sample (as suggested by GISAXS) or simply the effects of stronger Pt-alumina interactions on the Pt electronic structure.

4.3.5 Morphology Characterization by ISS

The surface of the samples was probed by He^+ ion scattering in order to obtain information regarding the morphology of the ALD overcoat. Figure 4.10a shows a series

of ISS spectra showing just the region of the Pt peak, for soft-landed $Pt_{24}/SiO_2/Si$ with one 423 K ALD alumina overcoat. The Pt ISS peak results primarily from events where He^+ scatters from a single Pt atom in the top-most layer of the sample.[42] Adsorbates or overlayers tend to attenuate ISS signals from underlying atoms, due to a combination of shadowing, blocking, and reduced ion survival probability,[23,42] but the signals tend to recover as the He^+ beam slowly sputters the adsorbates away. Here, the Pt ISS intensity is initially small, but increases by an order of magnitude during the first three ISS scans, indicating that ALD left a nearly complete adsorbate layer on the Pt_{24}, which quickly sputtered away, exposing underlying Pt. The final scan in the set was taken after the sample was exposed for 2 min to 1 keV Ar^+, which sputters material much more rapidly than 1 keV He^+. The Pt ISS intensity substantially reduced, because much of the Pt has been sputtered away.

To show the changes in sample surface composition more clearly, Figure 4.10b plots the intensity of the Pt ISS peak for four different samples, as the surfaces were slowly sputtered by a low flux He^+ beam. The samples, all soft-landed with identical Pt_{24} coverages, include $Pt_{24}/SiO_2/Si$, $Pt_{24}SiO_2/Si$ with one 423 K ALD alumina overcoat, a $Pt_{24}/SiO_2/Si$ sample that was overcoated and then flashed to 600 K prior to analysis, and finally, a $Pt_{24}/SiO_2/Si$ that was heated in UHV to 423 K without ALD overcoating. The Pt signal was normalized to the sum of the Si and O signals to correct for any day-to-day variations in the He^+ intensity.

For the as-deposited sample, the Pt signal is at maximum at zero He^+ exposure, and simply decays due to the loss of surface Pt by He^+ sputtering. The monotonic decay is indicative of no significant initial adsorbate coverage that would attenuate signal from

underlying Pt. For the sample that was simply annealed to 423 K, the initial signal is a factor of ~two smaller than for the as-deposited sample, indicating that only about half as many Pt atoms were in the top-most sample layer. Note that the decay rate for the annealed sample is slower than for as-deposited Pt_{24}, which is also consistent with a more multilayered morphology, where sputtering of top-layer Pt exposes underlying Pt. Such changes could result from Pt_{24} sintering into larger, more multilayer clusters, or simply restructuring of initially flattened clusters into more three-dimensional structures. As noted, however, the GISAXS results in Figure 4.5 indicate that sintering does occur at this temperature, at least in an H_2 atmosphere.

When $Pt_{24}/SiO_2/Si$ was overcoated with 1 cycle of ALD, the initial Pt ISS signal is attenuated by ~93%, and slowly *increases* during the initial ~200 μA·sec of He^+ exposure. This behavior shows that the Pt was covered by a layer of adsorbed material that almost completely attenuated Pt ISS signal, with Pt signal recovering as the overlayer sputtered away. If the overcoated sample was flashed to 600 K prior to ISS experiment, the initial Pt ISS signal was attenuated by only ~80% when compared to as-prepared $Pt_{24}/SiO_2/Si$. When compared to the overcoated sample that was not flashed, the initial signal was roughly three times higher. From the TPD experiment in Figure 4.7, we know that considerable loss of organic species from the alumina overlayer would have occurred during the flash, thus, it is not surprising that the ISS attenuation is also lower (albeit still 80%). The dependence of Pt signal on He^+ exposure is also somewhat different for the two samples, with the sample that was not flashed showing more Pt signal recovery from sputtering. For the flashed sample, the Pt signal was nearly constant for the initial ~200 μA·sec of He^+ exposure, then declined slowly. 600 K flashing should remove a

substantial fraction of the organic contaminant in the alumina layer, but also is likely to have driven sintering of the Pt.

4.4 Discussion

XPS shows that alumina deposition occurs ~6 times more rapidly for $Pt_{24}/SiO_2/Si$, compared to SiO_2/Si, even though the Pt_{24} coverage is only equivalent to 0.1 of a close-packed Pt monolayer. This result indicates that Pt sites are ~60 times more efficient at initiating ALD, than SiO_2, that is, that ALD does provide an approach for strongly preferential deposition at cluster sites. CO TPD shows that ALD overcoating blocks all Pt-associated binding sites, and that during the first TPD run to 600 K, there is substantial desorption of both organics and water, indicating that the mild ALD conditions used did not drive the TMA-water reaction to completion. Even after the excess water and organics desorb, a second CO TPD shows that only the low-temperature CO binding sites recover, and the strong binding sites responsible for high-temperature CO desorption remain blocked. Previous temperature-dependent ISS experiments on Pt_n/alumina[43] indicated that CO desorbing at low temperatures is primarily in sites at the cluster periphery ("peripheral" sites), whereas the high-temperature sites are on top of the Pt clusters ("on-top" sites). Similar behavior was observed for small Pd clusters on TiO_2[44] and alumina,[45] and if we assume that this is true for $Pt_n/SiO_2/Si$, then these results suggest that even after heating, the strong binding sites on top of the Pt_{24} remain blocked. The conclusion that ALD blocks sites on top of the clusters is also consistent with the ISS results, showing that one ALD cycle almost completely attenuates scattering from Pt, and that there is only modest recovering of Pt signal after flashing the sample to 600 K.

In considering the ALD mechanism, it is useful to review literature for water and TMA interactions with Pt surfaces. A previous H_2O TPD study on Pt(553) has shown that H_2O does not adsorb on Pt(553) surface at 423 K and can only dissociate into OH when the surface is preadsorbed with atomic oxygen.[46] A recent XPS and theoretical study of H_2O adsorption on Pt nanoparticles has also shown that H_2O hardly chemisorbs on Pt nanoparticles at room temperature due to the lack of bonding and antibonding states for H_2O chemisorption.[47] Our observation that water does not desorb significantly from $Pt_{24}/SiO_2/Si$ (Fig. 4.9) suggests that water also does not adsorb significantly on smaller supported Pt clusters.

Detwiler et al.[48] reported a study of TMA adsorption on Pt(111) and Pd(111). They found that TMA adsorbs on Pt(111) at 373 K, as evidenced by XPS showing C 1s at 283.8 eV and Al 2p at 73.0 eV, which is in the range expected for Al^0. Density functional theory (DFT) showed that TMA dissociation to adsorbed monomethylaluminum and methyl is exothermic on Pt(111), and dissociation to $Al_{ads} + CH_{3ads}$ is only slightly endothermic from monomethylaluminum. Similar behavior was found by Detwiler et al.[48] and Lu et al.[8,49] for TMA on Pd(111). Lu et al. also reported that $AlCH_3$* can further dissociate into Al* and CH_3* on Pt(211) surface, and both $AlCH_3$ * and Al* transform into $Al(OH)_3$* species in the following H_2O exposure.[49] These results suggest that TMA probably dissociates when chemisorbed on Pt clusters as well, forming adsorbed $Al(CH_3)_x$* and CH_3*. After the subsequent H_2O exposure, we observe by XPS that Al is oxidized, suggesting reaction to form adsorbed $Al(OH)_x$.

When samples are heated after ALD, both H_2O^+ and CH_4^+ signals are observed, indicating that in addition to $Al(OH)_x$, the samples contain some organics, such as

adsorbed methyl, such that both water and methane (and perhaps other organic species) can form by recombination reactions. This desorption is presumably responsible for partial recovery of Pt ISS signal and CO adsorption sites. The resulting partial alumina layer does, however, continue to block the stronger CO binding sites.

For heterogeneous catalysis, different sites (terraces, edges) of nanoparticles are responsible for formation of different products during a catalytic reaction. Zhang et al.[4] previously reported that the selectivity of Pd nanoparticles (~1.3 nm) to furan, the product of furfural hydrogenation, increases after the Pd catalysts are overcoated with 10 cycles of alumina ALD. They concluded that the terrace sites of Pd nanoparticles favoring the formation of furan remain available after ALD, whereas step sites responsible for side reactions are passivated by alumina via ALD. Feng et al.[2] also found that the low-coordinated sites of Pd nanoparticles (~1.4 nm) can be fully covered by 8 cycles of alumina ALD, by using DRIFTS CO chemisorption. In our case, as shown in Figure 4.11, the Pt clusters are in an even smaller size range with nearly all surface Pt atoms having low-coordination numbers, and alumina ALD initiates with high efficiency, initially completely blocking all CO binding sites, and leaving the stronger binding sites passivated even after heating, with only weakly binding peripheral sites available.

The remaining issue is what ALD and subsequent heating does to the Pt clusters themselves. For $Pt_{24}/SIO_2/Si$ without any ALD, GISAXS shows a sharp initial size distribution, in the range expected for Pt_{24}, which broadens and shifts to larger size when the sample is heated above 373 K. Since ALD was performed at 423 K, it is not unreasonable to expect that there should have been some ripening of the clusters. Unfortunately, alumina ALD, itself, introduces considerable nanoscale disorder into the

samples, even for the samples in which Pt_{24} was deposited after ALD. In those samples, the room temperature GISAXS scatterer diameter distribution is already broad, peaking above the size range expected for Pt_{24}, even though the samples were never heated after Pt_{24} deposition. Furthermore, because the alumina layer loses water and organics when heated, it is impossible to separate the effects of Pt ripening versus alumina layer consolidation/restructuring on the scatterer size distributions when the samples are heated.

4.5 Conclusion

We have shown that alumina growth via ALD in the first few cycles strongly depends on the active sites present on the substrates. For SiO_2/Si, ALD initiates only at a small fraction of sites on the surface, presumably corresponding to defects in the silica layer. When Pt clusters are present, alumina growth initiates efficiently on them, via dissociative chemisorption of TMA, followed by reaction with water. Although we chose alumina ALD as a well characterized system for this initial study, the fact that ALD initiates preferentially on small clusters suggests that this may be an efficient approach to generated size-selected bimetallic clusters, by selectively doping size-selected seed clusters of one metal by ALD of the second metal. Experiments with boron and tin deposition using this approach are under way.

4.6 References

(1) Lu, J. L.; Fu, B. S.; Kung, M. C.; Xiao, G. M.; Elam, J. W.; Kung, H. H.; Stair, P. C. *Science* **2012**, *335*, 1205.

(2) Feng, H.; Lu, J.; Stair, P. C.; Elam, J. W. *Catal. Lett.* **2011**, *141*, 512.

(3) O'Neill, B. J.; Jackson, D. H. K.; Crisci, A. J.; Farberow, C. A.; Shi, F.; Alba-Rubio, A. C.; Lu, J.; Dietrich, P. J.; Gu, X.; Marshall, C. L.; Stair, P. C.; Elam, J. W.; Miller, J. T.; Ribeiro, F. H.; Voyles, P. M.; Greeley, J.; Mavrikakis, M.; Scott, S. L.; Kuech, T. F.; Dumesic, J. A. *Angew. Chem., Int. Ed.* **2013**, *52*, 13808.

(4) Zhang, H. B.; Gu, X. K.; Canlas, C.; Kropf, A. J.; Aich, P.; Greeley, J. P.; Elam, J. W.; Meyers, R. J.; Dumesic, J. A.; Stair, P. C.; Marshall, C. L. *Angew. Chem., Int. Ed.* **2014**, *53*, 12132.

(5) O'Neill, B. J.; Jackson, D. H. K.; Lee, J.; Canlas, C.; Stair, P. C.; Marshall, C. L.; Elam, J. W.; Kuech, T. F.; Dumesic, J. A.; Huber, G. W. *ACS Catal.* **2015**, *5*, 1804.

(6) Ma, Z.; Brown, S.; Howe, J. Y.; Overbury, S. H.; Dai, S. *J. Phys. Chem. C* **2008**, *112*, 9448.

(7) Wang, C.; Wang, H.; Yao, Q.; Yan, H.; Li, J.; Lu, J. *J. Phys. Chem. C* **2016**, *120*, 478.

(8) Lu, J.; Liu, B.; Greeley, J. P.; Feng, Z.; Libera, J. A.; Lei, Y.; Bedzyk, M. J.; Stair, P. C.; Elam, J. W. *Chem. Mater.* **2012**, *24*, 2047.

(9) Greeley, J. *Electrochimica Acta* **2010**, *55*, 5545.

(10) Lee, S.; Molina Luis, M.; Lopez Maria, J.; Alonso Julio, A.; Hammer, B.; Lee, B.; Seifert, S.; Winans Randall, E.; Elam Jeffrey, W.; Pellin Michael, J.; Vajda, S. *Angewandte Chemie (International ed. in English)* **2009**, *48*, 1467.

(11) Lee, S.; Lee, B.; Mehmood, F.; Seifert, S.; Libera, J. A.; Elam, J. W.; Greeley, J.; Zapol, P.; Curtiss, L. A.; Pellin, M. J.; Stair, P. C.; Winans, R. E.; Vajda, S. *J. Phys. Chem. C* **2010**, *114*, 10342.

(12) Winans, R. E.; Vajda, S.; Ballentine, G. E.; Elam, J. W.; Lee, B.; Pellin, M. J.; Seifert, S.; Tikhonov, G. Y.; Tomczyk, N. A. *Top. Catal.* **2006**, *39*, 145.

(13) Dai, Y.; Gorey, T. J.; Anderson, S. L.; Lee, S.; Lee, S.; Seifert, S.; Winans, R. E. *J. Phys. Chem. C* **2017**, *121*, 361.

(14) Lee, S.; Fan, C.; Wu, T.; Anderson, S. L. *Surface Science* **2005**, *578*, 5.

(15) Kulawik, M.; Nilius, N.; Rust, H.-P.; Freund, H.-J. *Phys. Rev. Lett.* **2003**, *91*, 256101.

(16) Jaeger, R. M.; Kuhlenbeck, H.; Freund, H.-J.; Wuttig, M.; Hoffmann, W.; Franchy, R.; Ibach, H. *Surf. Sci.* **1991**, *259*, 235.

(17) Libuda, J.; Winkelmann, F.; Bäumer, M.; Freund, H.-J.; Bertrams, T.; Neddermeyer, H.; Müller, K. *Surf. Sci.* **1994**, *318*, 61.

(18) Ceballos, G.; Song, Z.; Pascual, J. I.; Rust, H.-P.; Conrad, H.; Bäumer, M.; Freund, H.-J. *Chem. Phys. Lett.* **2002**, *359*, 41.

(19) Lay, T. T.; Yoshitake, M.; Mebarki, B. *J. Vac. Sci. Technol. A* **2002**, *20*, 2027.

(20) Stierle, A.; Renner, F.; Streitel, R.; Dosch, H.; Drube, W.; Cowie, B. C. *Science* **2004**, *303*, 1652.

(21) Schmid, M.; Shishkin, M.; Kresse, G.; Napetschnig, E.; Varga, P.; Kulawik, M.; Nilius, N.; Rust, H. P.; Freund, H. J. *Phys. Rev. Lett.* **2006**, *97*, 046101/1.

(22) Kaden, W. E.; Kunkel, W. A.; Anderson, S. L. *J. Chem. Phys.* **2009**, *131*, 114701.

(23) Aizawa, M.; Lee, S.; Anderson, S. L. *Surf. Sci.* **2003**, *542*, 253.

(24) Lee, S.; Lee, B.; Seifert, S.; Vajda, S.; Winans, R. E. *Nucl. Instrum. Methods Phys. Res., Sect. A* **2011**, *649*, 200.

(25) Ilavsky, J.; Jemian, P. R. *J. Appl. Crystallogr.* **2009**, *42*, 347.

(26) Ravel, B.; Newville, M. *J. Synchrotron Radiat.* **2005**, *12*, 537.

(27) Yeh, J. J.; Lindau, I. *At. Data Nucl. Data Tables* **1985**, *32*, 1.

(28) Powell, C. J.; Jablonski, A. *Electron Effective-Attenuation-Length Database version 1.3 ed.*; NIST: Gaithersburg, MD, 2011.

(29) Ott, A. W.; Klaus, J. W.; Johnson, J. M.; George, S. M. *Thin Solid Films* **1997**, *292*, 135.

(30) Elam, J. W.; Groner, M. D.; George, S. M. *Rev. Sci. Instrum.* **2002**, *73*, 2981.

(31) Lei, Y.; Zhao, H.; Rivas, R. D.; Lee, S.; Liu, B.; Lu, J.; Stach, E.; Winans, R. E.; Chapman, K. W.; Greeley, J. P.; Miller, J. T.; Chupas, P. J.; Elam, J. W. *J. Am. Chem. Soc.* **2014**, *136*, 9320.

(32) Molina, L. M.; Lee, S.; Sell, K.; Barcaro, G.; Fortunelli, A.; Lee, B.; Seifert, S.; Winans, R. E.; Elam, J. W.; Pellin, M. J.; Barke, I.; von Oeynhausen, V.; Lei, Y.; Meyer, R. J.; Alonso, J. A.; Fraile Rodriguez, A.; Kleibert, A.; Giorgio, S.; Henry, C. R.; Meiwes-Broer, K.-H.; Vajda, S. *Catal. Today* **2011**, *160*, 116.

(33) Roberts, F. S.; Kane, M. D.; Baxter, E. T.; Anderson, S. L. *Phys. Chem. Chem. Phys.* **2014**, *16*, 26443

(34) Yao, Q.; Wang, C.; Wang, H.; Yan, H.; Lu, J. *J. Phys. Chem. C* **2016**, *120*, 9174.

(35) Gow, T. R.; Lin, R.; Cadwell, L. A.; Lee, F.; Backman, A. L.; Masel, R. I. *Chem. Mater.* **1989**, *1*, 406.

(36) Naumkin, A. V.; Kraut-Vass, A.; Gaarenstroom, S. W.; Powell, C. J. NIST X-ray photoelectron spectroscopy database, 2012. NIST Standard Reference Database 20, Version 4.1. https://srdata.nist.gov/xps/Default.aspx (accessed March 28, 2017).

(37) Chusuei, C. C.; Lai, X.; Luo, K.; Goodman, D. W. *Top. Catal.* **2001**, *14*, 71.

(38) Bagus, P. S. Presented at the 225th ACS National Meeting, New Orleans, LA, United States, March 23-27, 2003.

(39) Kaden, W. E.; Wu, T.; Kunkel, W. A.; Anderson, S. L. *Science* **2009**, *326*, 826.

(40) Kaden, W. E.; Büchner, C.; Lichtenstein, L.; Stuckenholz, S.; Ringleb, F.; Heyde, M.; Sterrer, M.; Freund, H.-J.; Giordano, L.; Pacchioni, G.; Nelin, C. J.; Bagus, P. S. *Phys. Rev. B* **2014**, *89* 115436 1.

(41) Roberts, F. S.; Anderson, S. L.; Reber, A. C.; Khanna, S. N. *J. Phys. Chem. C* **2015**, *119*, 6033.

(42) Rabalais, J. W. *Principles and Applications of Ion Scattering Spectrometry: Surface Chemical and Structural Analysis*; Wiley: New York, 2003.

(43) Baxter, E. T.; Ha, M.-A.; Alexandrova, A.; Anderson, S. L. *ACS Catal,* submitted for publication.

(44) Kaden, W. E.; Kunkel, W. A.; Roberts, F. S.; Kane, M.; Anderson, S. L. *J. Chem. Phys.* **2012**, *136*, 204705/1.

(45) Kane, M. D.; Roberts, F. S.; Anderson, S. L. *Int. J. Mass Spectrom.* **2014**, *370*, 1.

(46) Van der Niet, M. J. T. C.; den Dunnen, A.; Juurlink, L. B. F.; Koper, M. T. M. *Phys. Chem. Chem. Phys.* **2011**, *13*, 1629.

(47) Cui, Y.; Harada, Y.; Ikenaga, E.; Li, R.; Nakamura, N.; Hatanaka, T.; Ando, M.; Yoshida, T.; Li, G.-L.; Oshima, M. *J. Phys. Chem. C* **2016**, *120*, 10936.

(48) Detwiler, M. D.; Gharachorlou, A.; Mayr, L.; Gu, X. K.; Liu, B.; Greeley, J.; Delgass, W. N.; Ribeiro, F. H.; Zemlyanov, D. Y. *J. Phys. Chem. C* **2015**, *119*, 2399.

(49) Lu, J. L.; Liu, B.; Guisinger, N. P.; Stair, P. C.; Greeley, J. P.; Elam, J. W. *Chem. Mater.* **2014**, *26*, 6752.

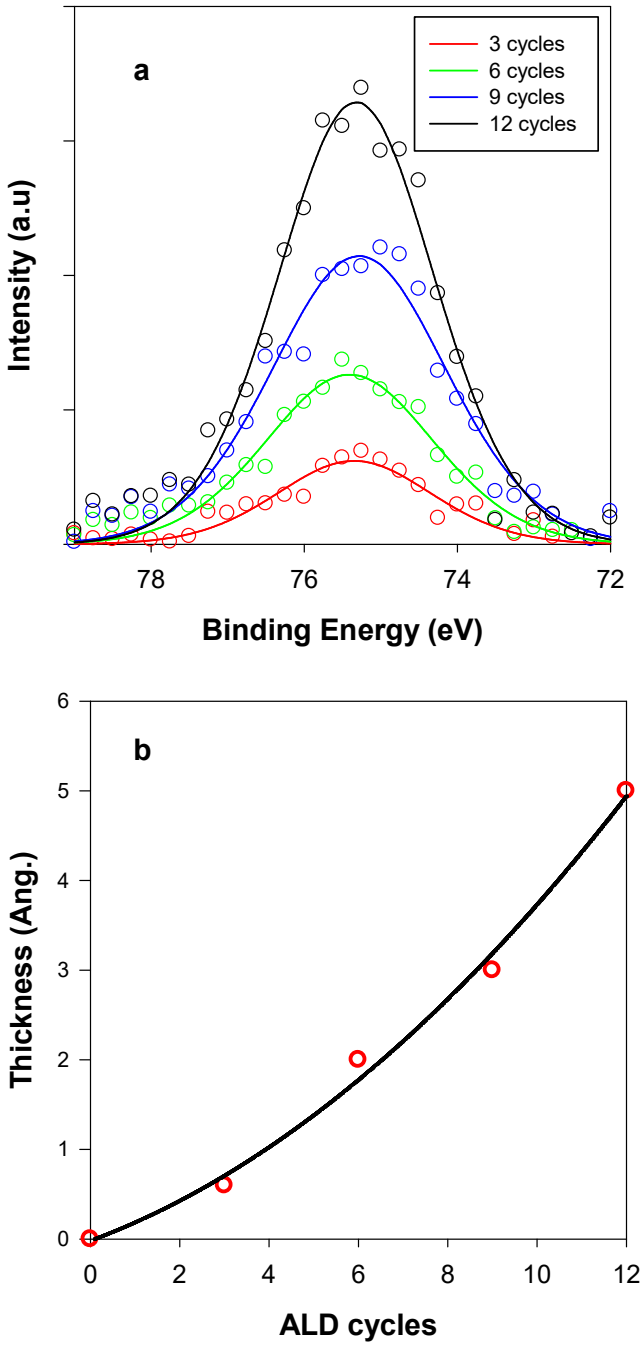

Figure 4.1 The growth rate calibration of alumina ALD on a clean silica substrate at the surface temperature of 423 K. (a) XP spectra of Al 2p (b) Calculated thickness of Al_2O_3 as a function of ALD cycles.

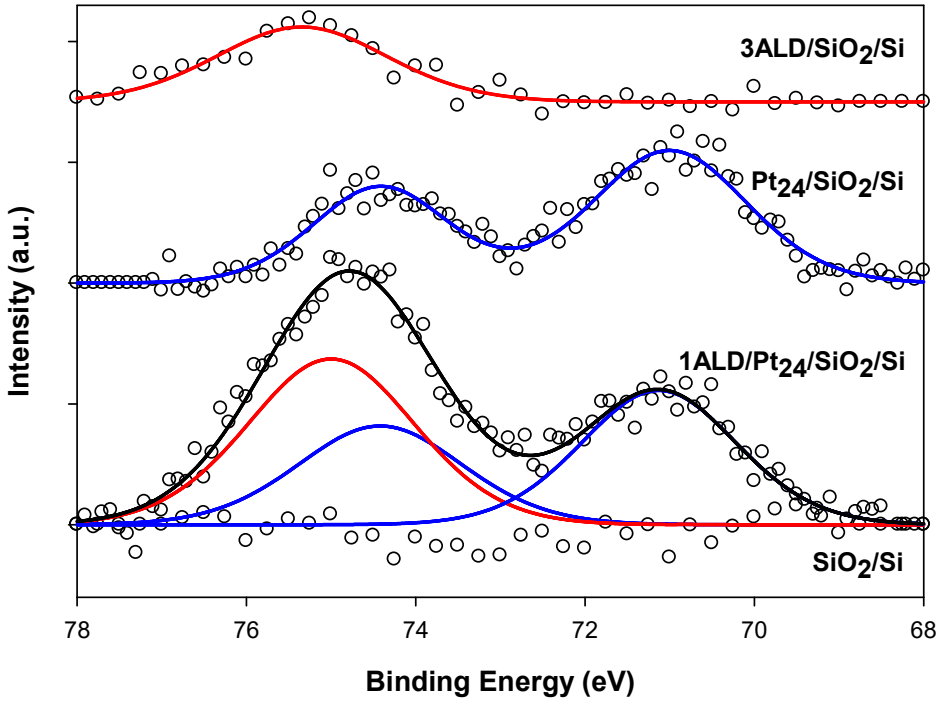

Figure 4.2 XPS of the Pt 4f and Al 2p region. Top: Spectrum for a SiO_2/Si substrate after three 3 ALD cycles. Middle: Spectrum of as-deposited Pt_{24}/SiO_2/Si. Bottom: Spectrum for Pt_{24}/SiO_2/Si after one ALD cycle, with fits showing Al 2p and Pt 4f contributions.

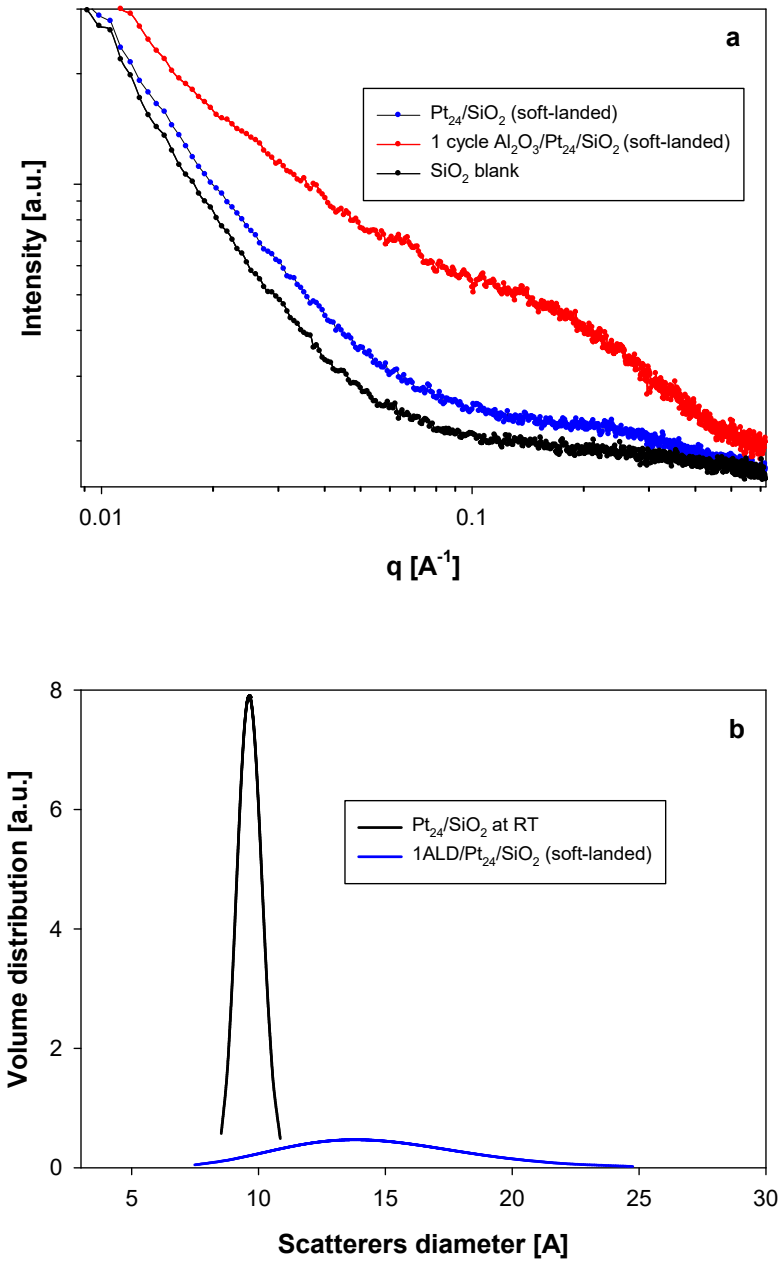

Figure 4.3 GISAXS for soft-landed $Pt_{24}/SiO_2/Si$ transferred in air, an ALD overcoated sample, and a clean blank SiO_2/Si sample. (a) Raw GISAXS scattering data (b) Fitted size distributions extracted by fitting the scattering data as in (a) for soft-landed $Pt_{24}/SiO_2/Si$, as well as soft-landed $Pt_{24}/SiO_2/Si$ with 1 cycle of Al_2O_3 ALD overcoat.

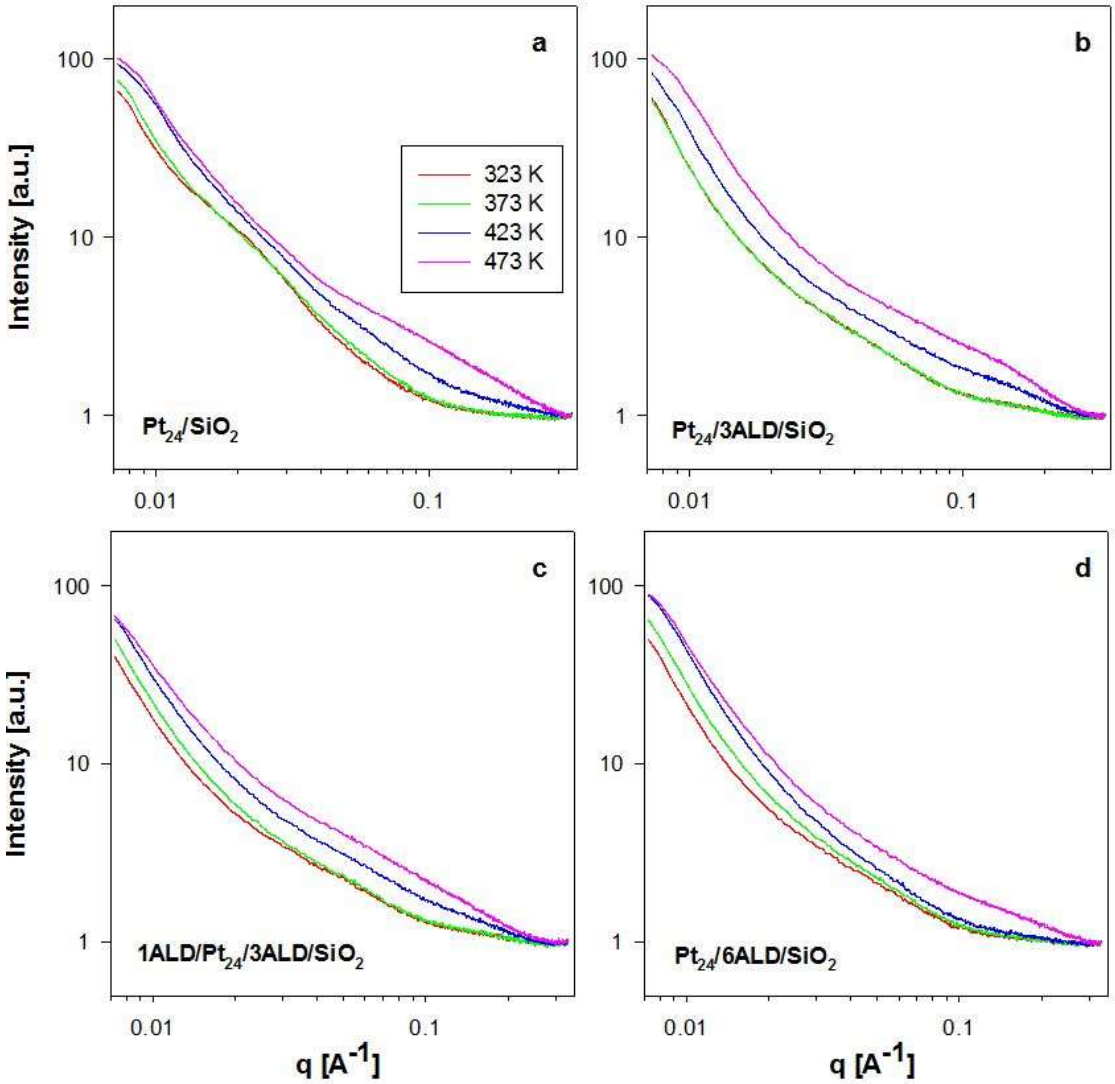

Figure 4.4 GISAXS scattering data for the sample (a) soft-landed $Pt_{24}/SiO_2/Si$, (b) soft-landed $Pt_{24}/SiO_2/Si$ with 3 cycles of ALD undercoat, (c) soft-landed $Pt_{24}/SiO_2/Si$ with 1 cycle of ALD overcoat and 3 cycles of ALD undercoat, and (d) soft-landed $Pt_{24}/SiO_2/Si$ with 6 cycles of ALD undercoat.

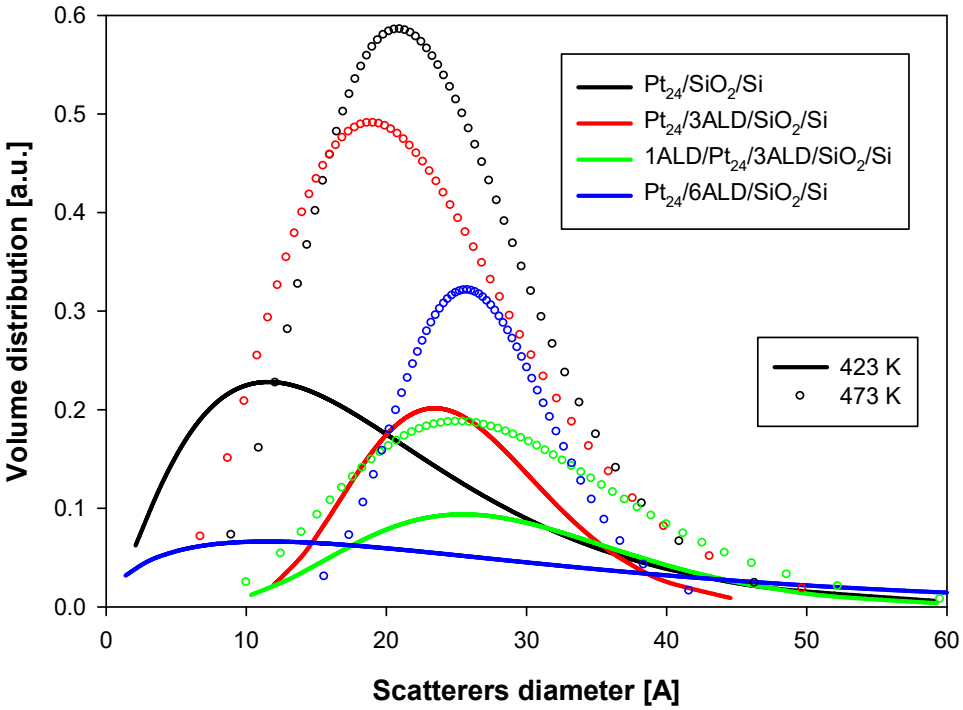

Figure 4.5 GISAXS scattering data for the sample (a) soft-landed $Pt_{24}/SiO_2/Si$, (b) soft-landed $Pt_{24}/SiO_2/Si$ with 3 cycles of ALD undercoat, (c) soft-landed $Pt_{24}/SiO_2/Si$ with 1 cycle of ALD overcoat and 3 cycles of ALD undercoat, and (d) soft-landed $Pt_{24}/SiO_2/Si$ with 6 cycles of ALD undercoat.

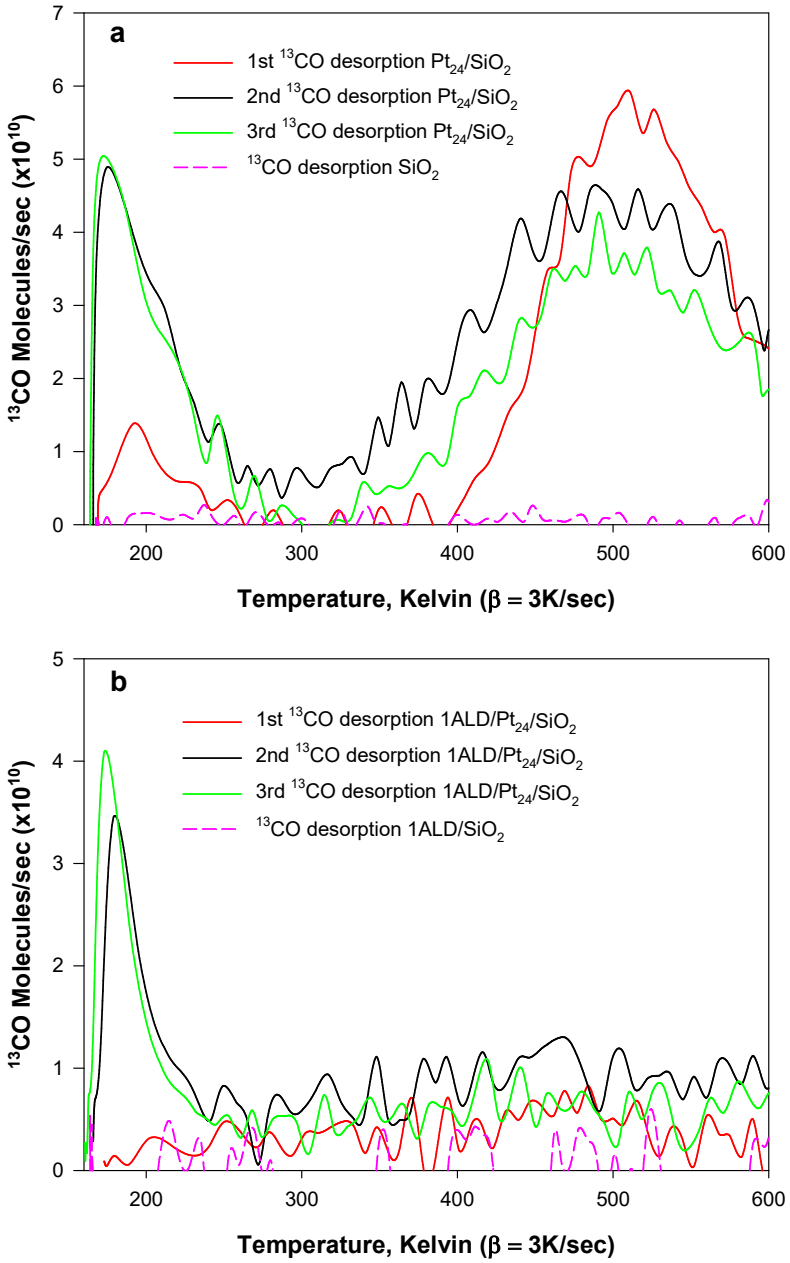

Figure 4.6 ^{13}CO desorption. (a) ^{13}CO desorption from $Pt_{24}/SiO_2/Si$ for three consecutive CO TPDs (solid), and a blank SiO_2/Si sample (dashed), after 10 L ^{13}CO exposure at 180 K. There are two distinct CO desorption peaks at ~190 K (low temperature) and 510 K (high temperature). (b) ^{13}CO desorbing from $Pt_{24}/SiO_2/Si$ with 1 cycle of ALD overcoat for three consecutive CO TPDs (solid) and a blank SiO_2/Si sample with 1 cycle of ALD overcoat. The main difference between the cluster samples with and without ALD overcoat is the disappearance of high-temperature feature for ALD overcoated sample.

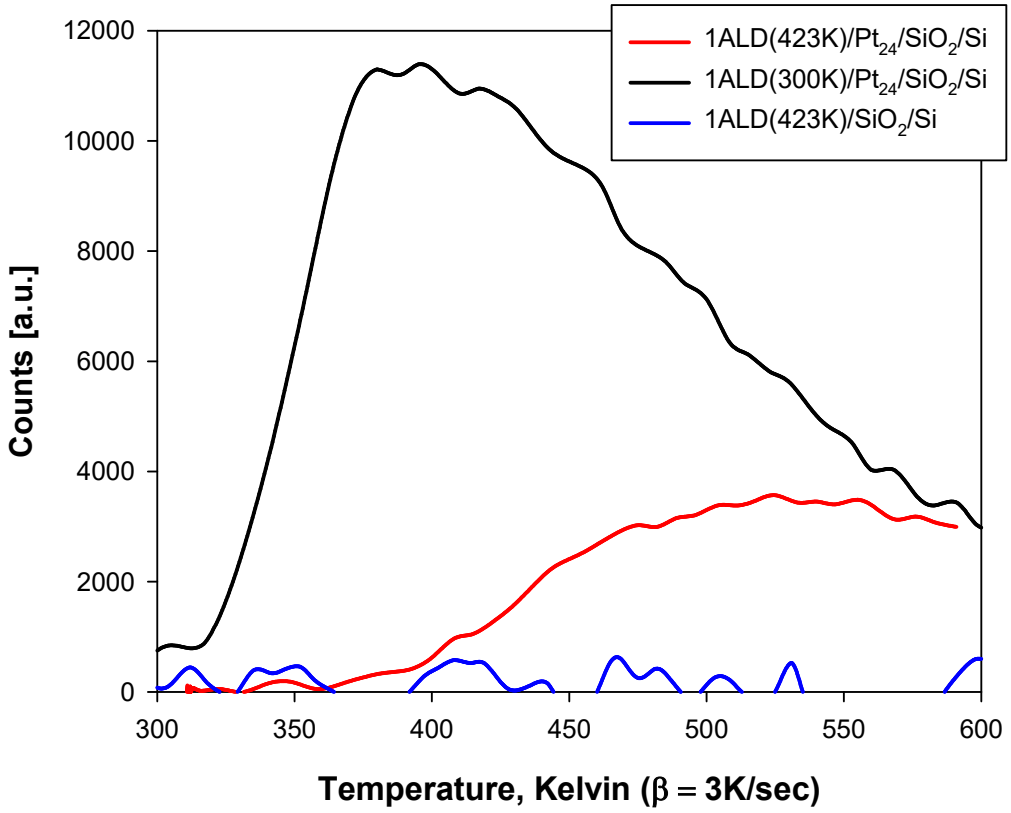

Figure 4.7 Mass 16 TPD following a single alumina ALD cycle on $Pt_{24}/SiO_2/Si$ at either 300 (black) or 423 K (red), and on SiO_2/Si at 423 K (blue).

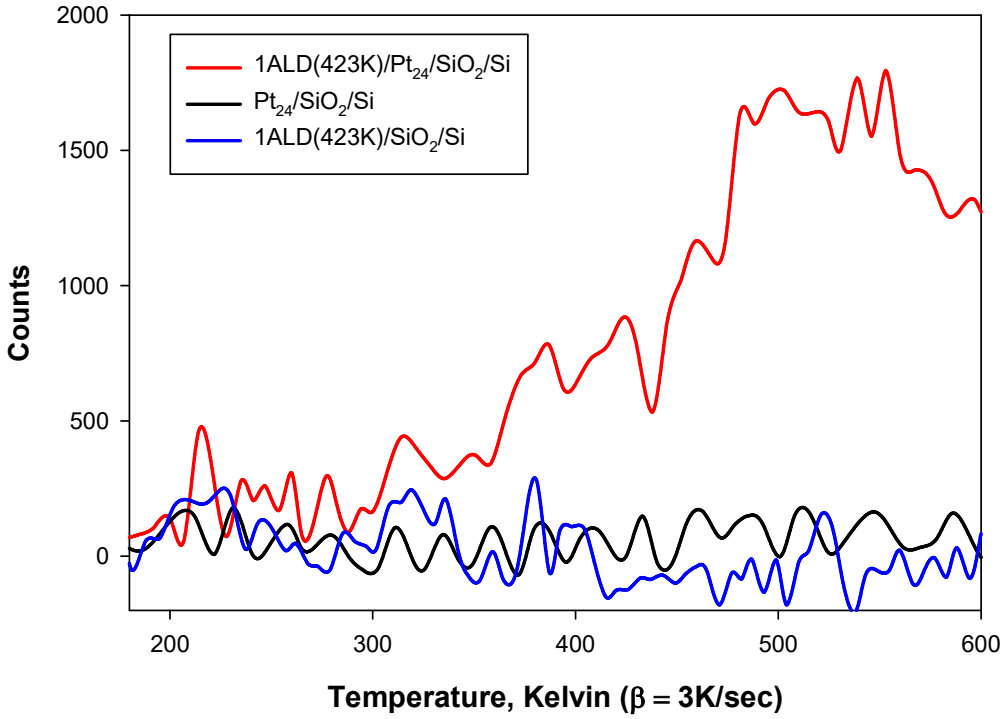

Figure 4.8 Mass 18 TPD following a single alumina ALD cycle on $Pt_{24}/SiO_2/Si$ at 423 K (red), and SiO_2/Si blank (blue), and for the sample $Pt_{24}/SiO_2/Si$ without ALD overcoat with H_2O being dosed at 423 K (black).

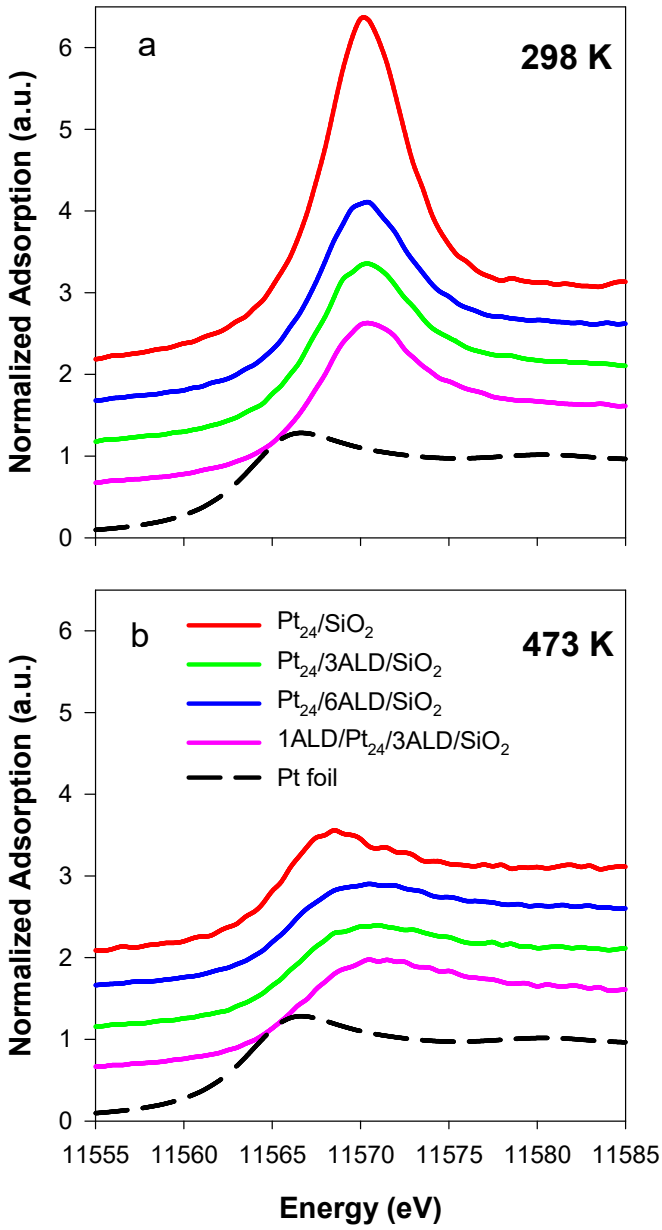

Figure 4.9 Normalized XANES spectra at Pt L_3-edge for the sample soft-landed $Pt_{24}/SiO_2/Si$ (red solid line), soft-landed $Pt_{24}/SiO_2/Si$ with 3 cycles of ALD undercoat (green solid line), soft-landed $Pt_{24}/SiO_2/Si$ with 1 cycle of ALD overcoat and 3 cycles of ALD undercoat (pink solid line), soft-landed $Pt_{24}/SiO_2/Si$ with 6 cycles of ALD undercoat (blue solid line), and Pt foil (black dashed line) at the temperature of 298 K (a) and 473 K (b).

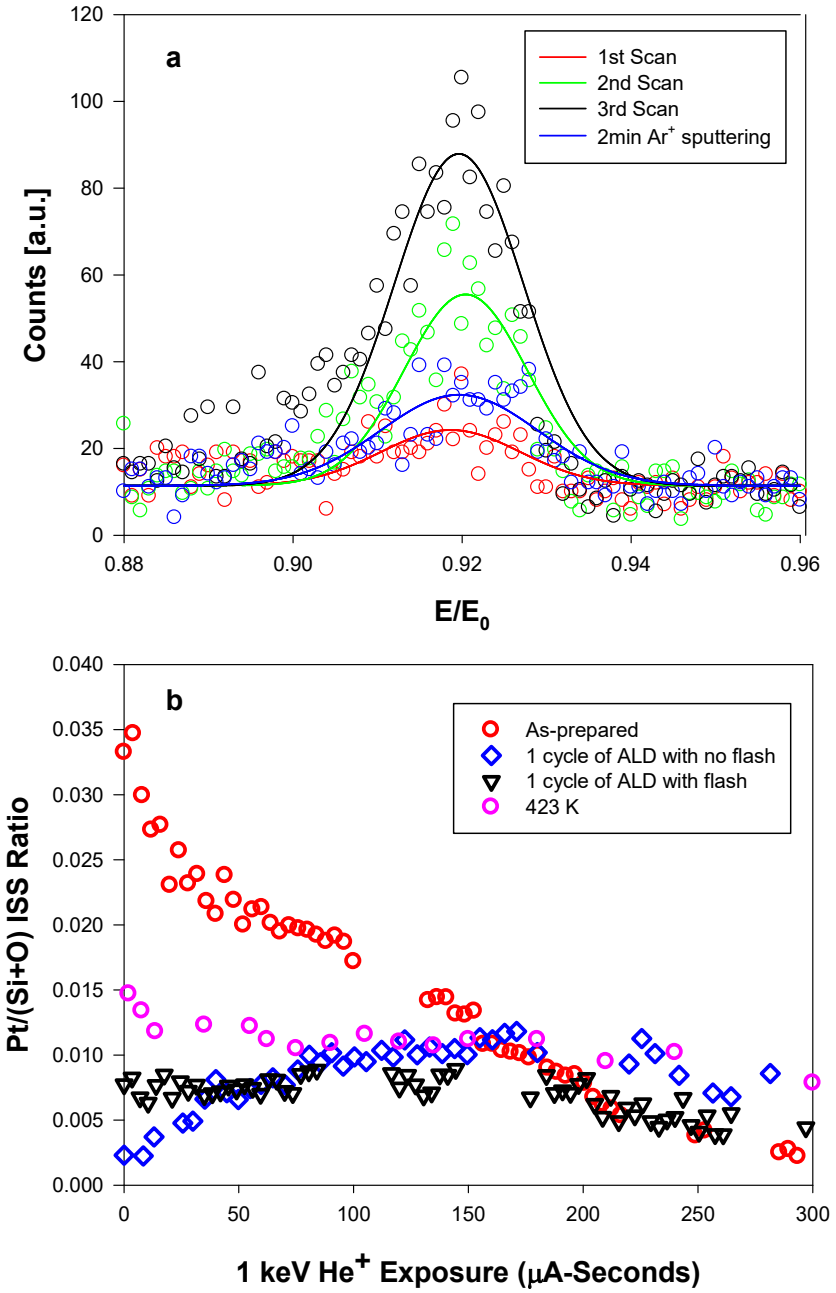

Figure 4.10: Pt ISS results for the probe of sample surface morphology. (a) Three consecutive high flux ISS scans and an additional scan after 2 min of 1 keV Ar+ sputtering on the sample 1ALD/Pt24/SiO2/Si, where ALD was performed at the substrate temperature of 423 K. (b) Normalized Pt ISS intensity for Pt24/SiO2/Si (red), samples with 1 cycle of ALD overcoat with (black) or without (blue) flash post-treatment, and a sample annealed at 423 K in vacuum (pink).

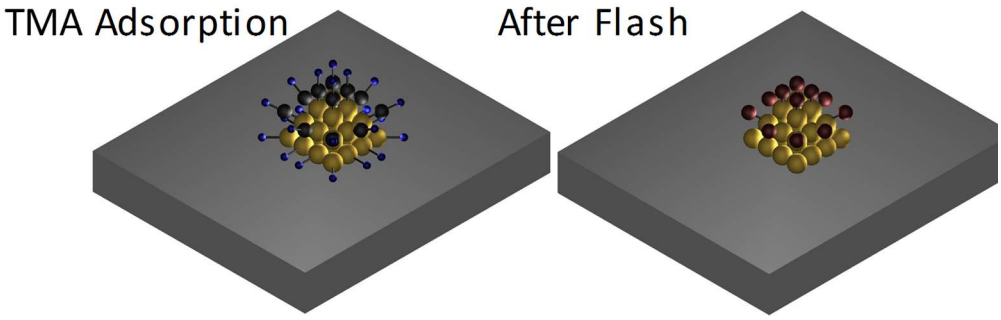

Figure 4.11 Schematic illustrations of alumina ALD mechanism on Pt clusters.

Table 4.1 Edge energies for all the samples described in Figure 4.9 at 298 K and 473 K.

Samples	Edge Energy (eV)	
	At 298 K	At 473 K
Pt foil	11564	11564
$Pt_{24}/SiO_2/Si$	11569	11566
Pt_{24}/3ALD/SiO_2/Si	11569	11566
Pt_{24}/6ALD/SiO_2/Si	11569	11566.5
1ALD/Pt_{24}/3ALD/SiO_2/Si	11569	11567.5

CHAPTER 5

CONCLUSION

5.1 Conclusions

Three topics were presented in this dissertation, including a detailed description of a new cluster deposition instrument, size effects on XANES of nanometer Pt clusters, and Al_2O_3 ALD effects on size-selected Pt clusters. In order to investigate the effects of ALD and particle size on the metal clusters, a clusters deposition instrument was built with the capability of depositing size-selected metal clusters, performing atomic layer deposition in high vacuum, and characterizing samples with in situ XPS, UPS, ISS, and TPD, as discussed in Chapter 2. Meanwhile, the fast sample transferring system made it possible to prepare multiple samples in a short time frame and analyze them ex situ using characterization techniques, such as XANES, GISAXS, and so forth.

A combination of surface analysis techniques was used to determine the inherent size effects on XANES of size-selected Pt clusters on silica, and revealed that the effects of particle size on the electronic structure can mislead the interpretation of XANES spectra. For $Pt_n/SiO_2/Si$ samples, detailed in Chapter 3, a high white line intensity and absorption edge energy were observed in the Pt L_3 edge, relative to bulk Pt, which would suggest that the Pt clusters were oxidized. However, the XPS has confirmed that all Pt clusters were in the zero oxidation state. It was suggested that the higher white line intensity was attributable to the localization of empty state wavefunctions, whereas the enhanced white line intensity was the result of the development of a band gap in small clusters.

The work presented in Chapter 4 focuses on the detailed investigation of Al_2O_3 ALD on Pt_{24} clusters supported on SiO_2/Si. It was found that the growth rate of Al_2O_3 ALD was much smaller than other reported values, mainly due to the loss of hydroxyl

group on the surface during sample cleaning process. However, with this low growth rate, it is surprising that all Pt_{24} active sites are completely blocked by just 1 cycle of Al_2O_3 ALD overcoat. This provides a potential method to modify size-selected clusters with other small metal promoters.

APPENDIX

SUPPORTING INFORMATION INCLUDED FOR

CHAPTER 4

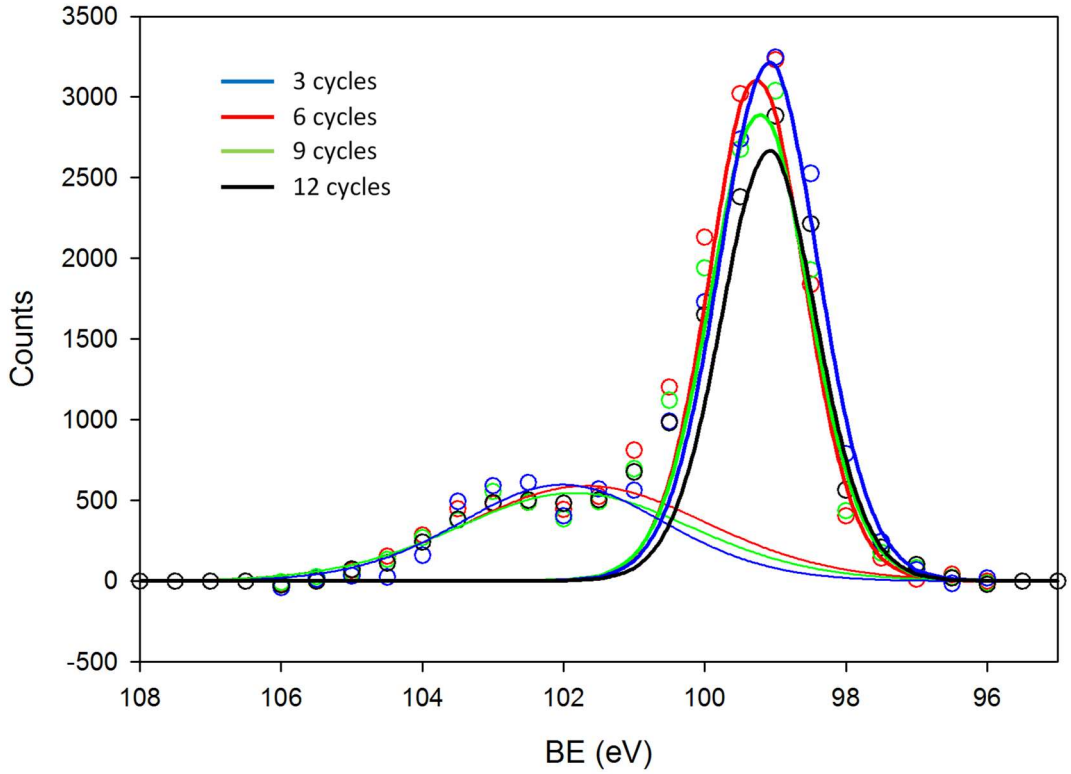

Figure A.1 Si 2p XP spectra with 3 – 12 cycles of Al_2O_3 ALD grown on SiO_2/Si substrate at a surface temperature of 423 K.

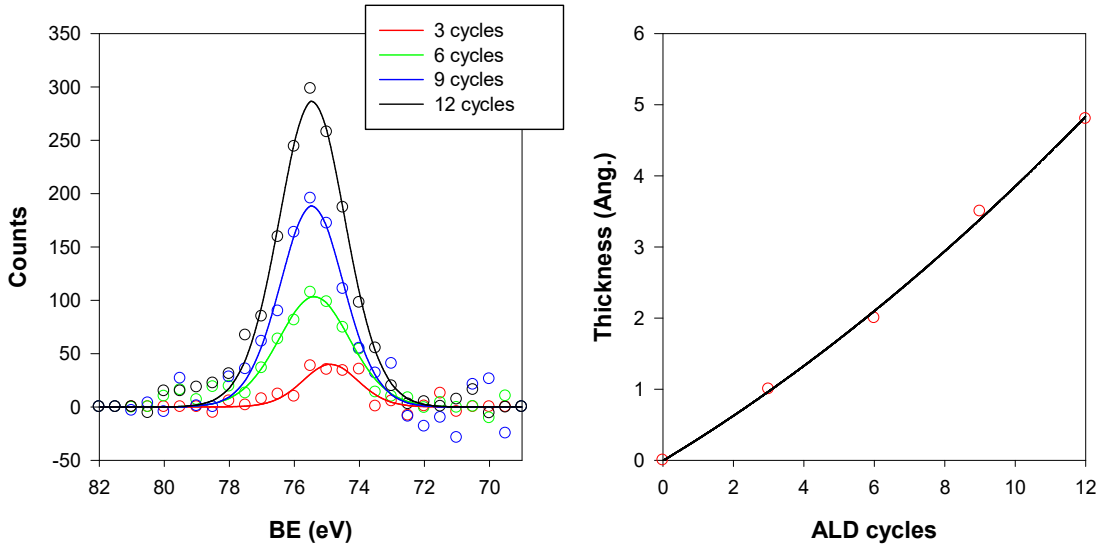

Figure A.2 XP Spectra of Al 2p and thickness of Al_2O_3 ALD grown on SiO_2 substrate at a surface temperature of 423 K. Left: XP spectra of Al 2p with 3 – 12 cycles of Al_2O_3 ALD grown on SiO_2 substrate at a surface temperature of 423 K. TMA and H_2O were dosed at ~5 × 10^{-5} Torr for 150 s. Right: Calculated thickness of Al_2O_3 as a function of ALD cycles.

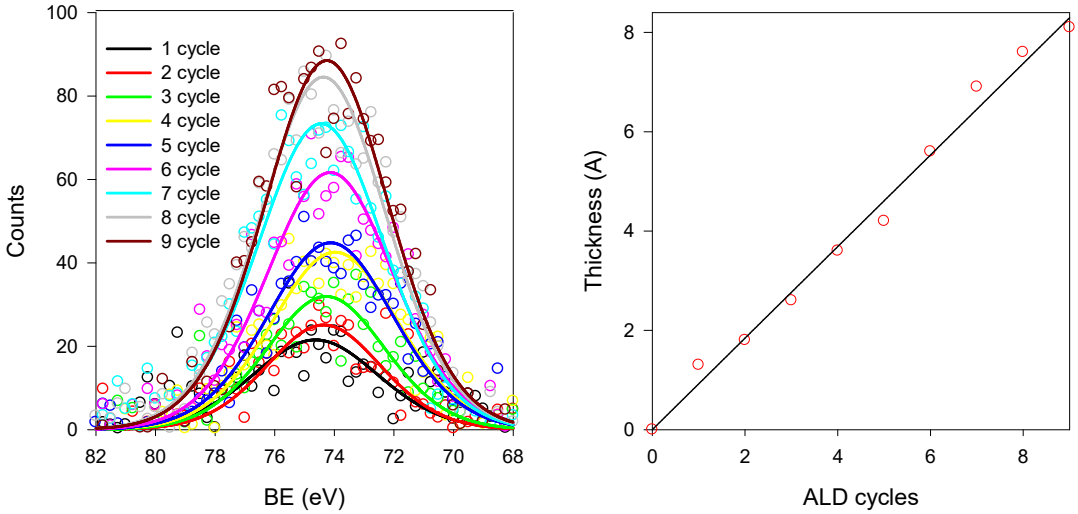

Figure A.3 XP spectra of Al 2p and thickness of Al_2O_3 ALD grown on SiO_2 substrate at room temperature. Left: XP spectra of Al 2p with 0 – 9 cycles of Al_2O_3 ALD grown on SiO_2 substrate at room temperature. TMA and H_2O were dosed at ~2×10^{-6} Torr for 150 s. Right: Calculated thickness of Al_2O_3 as a function of ALD cycles.

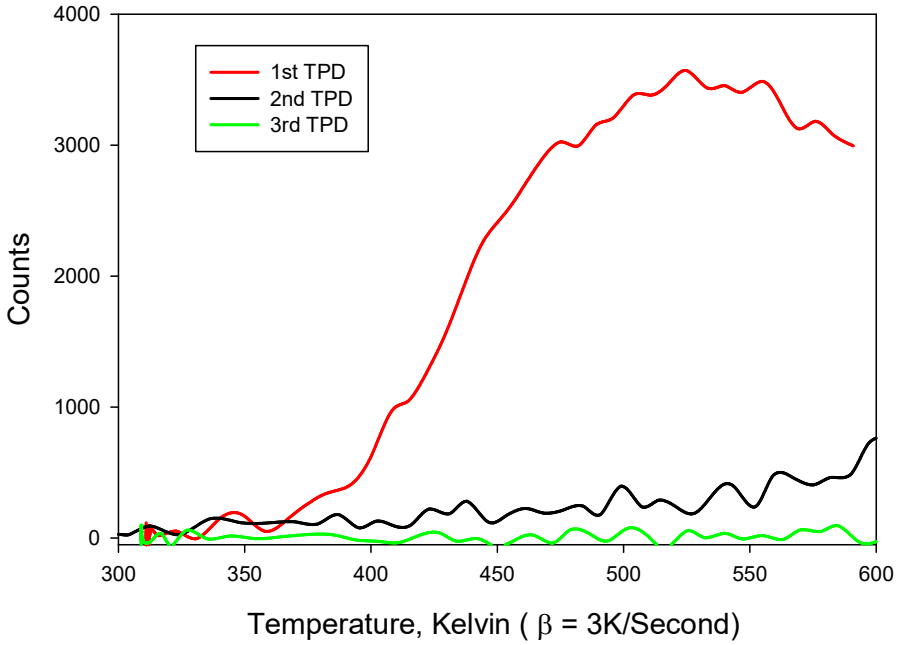

Figure A.4 Three consecutive runs of mass 16 TPD, taken during the CO TPD for the 1cycle of ALD overcoated $Pt_{24}/SiO_2/Si$ sample, where the ALD was performed at the surface temperature of 423 K.

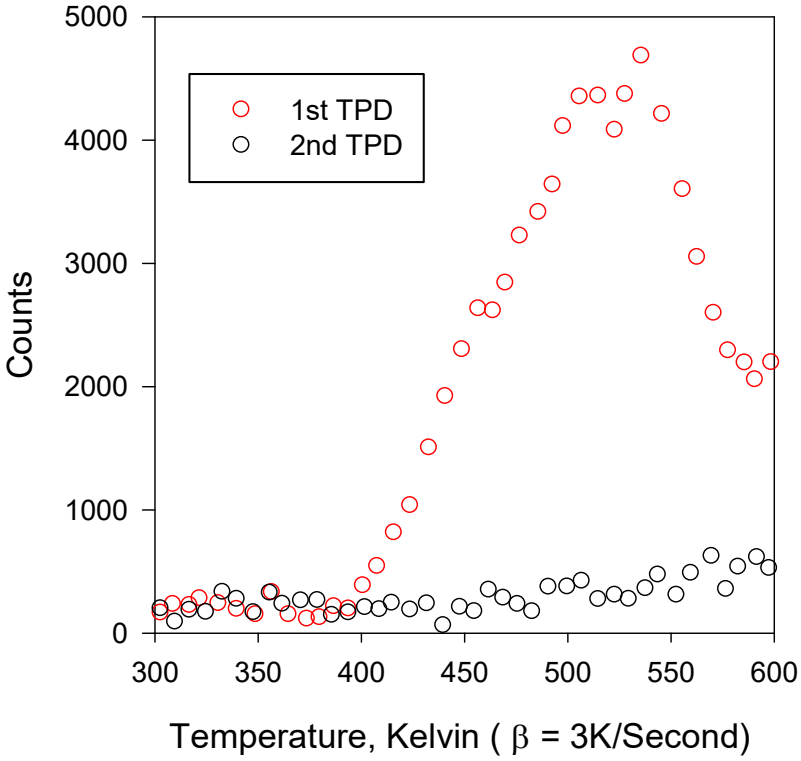

Figure A.5 Two consecutive runs of mass 16 TPD, taken during the CO TPD for the 1 cycle of ALD overcoated $Pt_{24}/Al_2O_3/NiAl$ sample, where the ALD was performed at the surface temperature of 423 K.

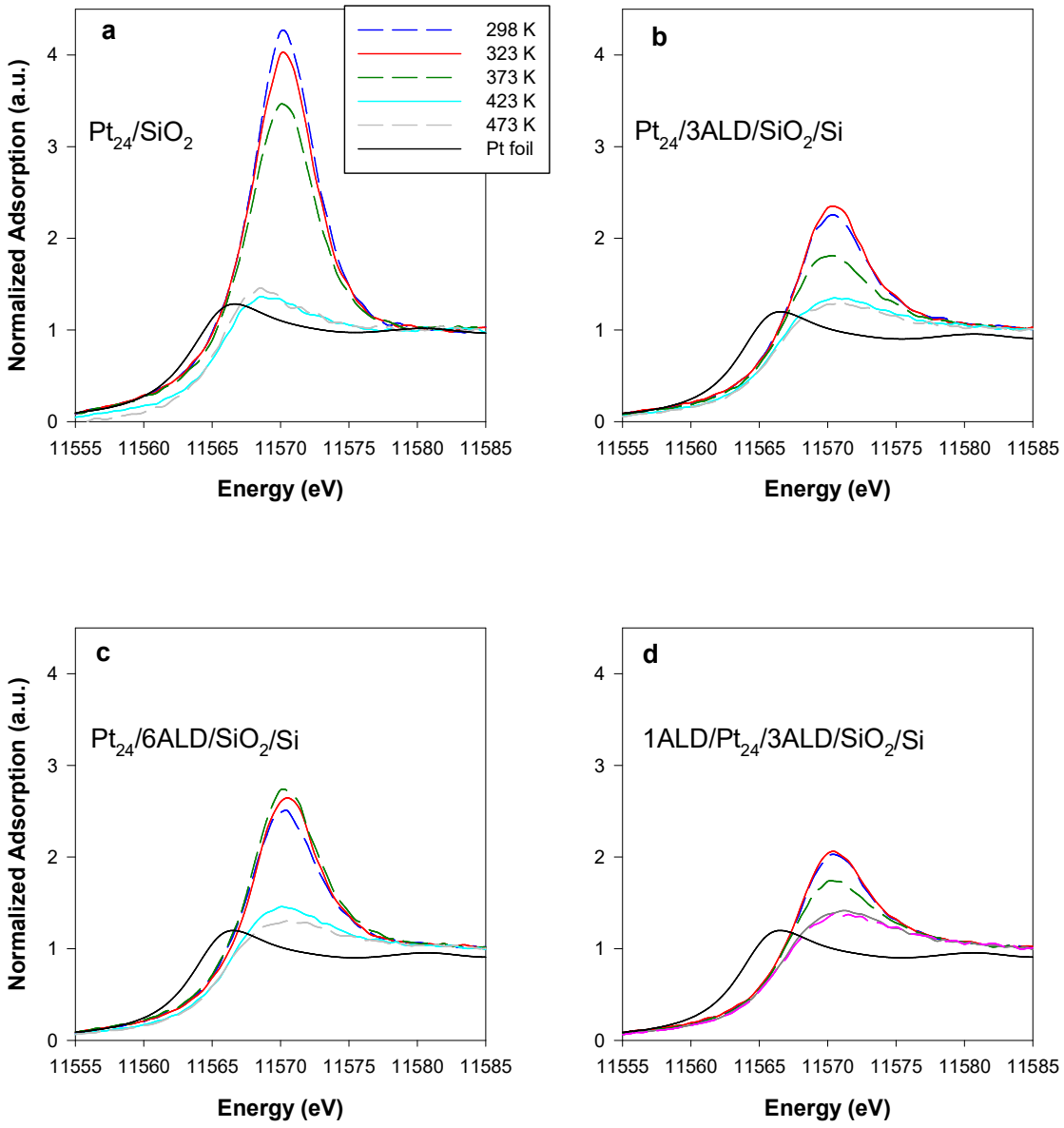

Figure A.6 Normalized XANES spectra at Pt L_3-edge for the sample (a) soft-landed $Pt_{24}/SiO_2/Si$, (b) soft-landed $Pt_{24}/SiO_2/Si$ with 3 cycles of ALD undercoat, (c) soft-landed $Pt_{24}/SiO_2/Si$ with 6 cycles of ALD undercoat (d) soft-landed $Pt_{24}/SiO_2/Si$ with 1 cycle of ALD overcoat, and 3 cycles of ALD undercoat at room temperature and different annealing temperatures.